Alma Mater Studiorum · Università di Bologna

PHYSICS AND ASTRONOMY DEPARTMENT 'AUGUSTO RIGHI'
Master Degree Programme in Astrophysics and Cosmology

Assessing the origin of the extragalactic neutrino background with new cosmological simulations

Graduation Thesis

Supervisor: Prof. Franco Vazza
Co-supervisor: Prof. Sara Buson

Presented by:
Francesca Zanetti

Academic Year 2023-2024

Abstract

The extragalactic neutrino background is a diffuse emission with unknown origin. It was first detected in 2013 by the IceCube Observatory in the energy ranges between 10 TeV and 2 PeV. Its spectrum has been found to correspond to a power-law spectrum with index of -2.5 (Aartsen and et al, 2013). The study of such high energy particles is of paramount importance in finding the strongest acceleration sources in the Universe and understanding their underlying mechanisms. It is suggested that sources capable of producing such high energy neutrinos should also be responsible for the acceleration of Ultra High Energy Cosmic Rays (whose origin is unknown too) (Spurio, 2018). Different classes of sources have been suggested as potential contributors to the background, among these: Active Galactic Nuclei, Star Forming Galaxies, Tidal Disruption Events and Gamma Ray Bursts. Recent studies suggest that AGNs should be the main contributors to the extragalactic neutrino diffuse flux,in particular, it seems that non-jetted AGNs such as Seyfert galaxies might be responsible for the background at energies below 1 PeV while jetted AGNs such as blazars should dominate the high energy part (Padovani et al., 2024).

Star Forming Galaxies, on the other hand, should account for less than 3% of it (Ajello et al., 2020), while a possible contribution from either TDEs or GRBs is still debated (Winter, 2024).

The formation and growth of cosmic structures cause the formation of accretion shocks. Such shocks convert part of their kinetic energy into thermal energy, amplification of magnetic fields and particle acceleration. These shocks might therefore accelerate cosmic rays and the interactions between cosmic rays and the thermal gas might produce neutrinos and gamma rays (Bykov et al., 2019).

My Thesis work has the goal of understanding the contributions of cosmic populations to the extragalactic neutrino background through the employment of cosmological magneto-hydrodynamical simulations using ENZO. Such simulations are designed to investigate the injection and evolution of cosmic rays by different mechanisms operating in the cosmic web. They cover a comoving volume of $(42.5Mpc)^3$ with a static grid of cells with a constant spatial resolution of 41.5 kpc/cell and a constant mass resolution of $1.01 \times 10^7 M_\odot$ per dark matter particle. Cosmic rays are injected at runtime by simulated jetted AGN, star formation and cosmic shocks and are assumed to generate neutrinos and gamma-rays through proton-proton interactions. These simulations allow me to compute the neutrino and gamma-ray fluxes, based on the formalism developed by Pfrommer and Ensslin (2004) which was applied to all cells at several snapshots. The simulation's snapshots lie in the redshift range between 0.01 and 3 with a redshift spacing of about $\Delta z = 0.2$. I computed the cumulative neutrino and gamma ray fluxes taking into account redshift dependent corrections such as bandwidth compression (Condon and Matthews, 2018) in order to generate a realistic model for the full sky background of neutrinos and gamma-rays, in the energy bands $0.5 - 200$ GeV for the gamma-rays and $10^5 - 10^6$ GeV for the neutrinos. I compared the simulated cumulative neutrino and gamma ray fluxes with the *Fermi*-Large Area Telescope (LAT) limit for the gamma-ray and with the IceCube obseravtory limit for neutrinos. The analysis helped constraining the injection efficiency of cosmic rays in the simulation. I found that, in order for the gamma-ray emission to be consistent with the *Fermi*-LAT limit, the cosmic ray injection efficiency of AGN and cosmic shocks in the simulation should be decreased by at least a factor 6. Once this effect is taken into account, the main contributors to the neutrino background are found to be AGN, while the contributions from star-formation and cosmic shocks are estimated to be about one order of magnitude lower. The results show that AGN, star-formation and cosmic shocks are responsible for the entirety of the gamma-ray emission, but only for a fraction of the neutrino emission. These prompt to extend the study to investigate additional mechanisms such as photo-pion production and attenuation occurring in AGN or the contribution from non-jetted AGN.

Contents

1 Introduction

The main goal of this Thesis is understanding the contributions of AGN, cosmic shocks and star-formation to the extragalactic neutrino diffuse flux and to the γ-ray background. The presence of many interconnected topics calls for a broad introduction, capable of giving at least an overview of their characteristics and their importance for the current work. A small explanation for the specific structure I have chosen for my Introduction is in order.

Since neutrinos are the main focus of this work, they are the first topic presented (Section 1.1). Next, since this work deals with extragalactic neutrinos ($E_\nu \sim$ TeV-PeV) which are believed to originate from high cosmic ray processes, a whole Section is dedicated to the description of cosmic rays (Section 1.2). The neutrino emission in astrophysical environments is believed to be often accompanied by γ-ray emission, hence Section 1.3 is completely dedicated to them.

Finally, the last two sections of the Introduction are dedicated to the description of the possible sources of neutrino and γ-ray emission addressed in this work: Active Galactic Nuclei (Sect 1.5) and cosmic shocks (Sect. 1.4).

1.1 Neutrinos: generalities

Neutrinos are regarded as fundamental particles by the Standard Model of Particle Physics. As can be seen from Figure 1, they are divided into three generations: electronic, muonic or tauonic. These generations or flavours are attributed dynamically for example, an electronic neutrino ν_e is either produced together with a positron e^+ or produces an electron e^-. Traditionally these particle have been regarded as massless however, recent experiments with solar, atmospheric and reactor neutrinos proved the existence of transitions between different flavours caused by mixing. These transitions are often referred to as oscillations and can be explained as transitions occurring when the mass and flavour of neutrinos do not coincide (Volpe, 2015). The current data suggest that neutrinos' masses are extremely small, below 1 eV, and that the three generations of neutrino have different masses.

The mass of neutrinos brings with it the additional problem of whether neutrinos are Dirac or Majorana particles. In the first case neutrinos would carry a lepton charge (such as the total lepton charge) that should be conserved by particle interactions. In this scenario neutrinos and antineutrinos would be two distinct particles carrying a different value for the lepton charge and they would be massless. If neutrinos were Majorana particles, instead, no lepton charge wold be conserved, neutrinos would be identical to antineutrinos and they would carry a mass (Group, 2012).

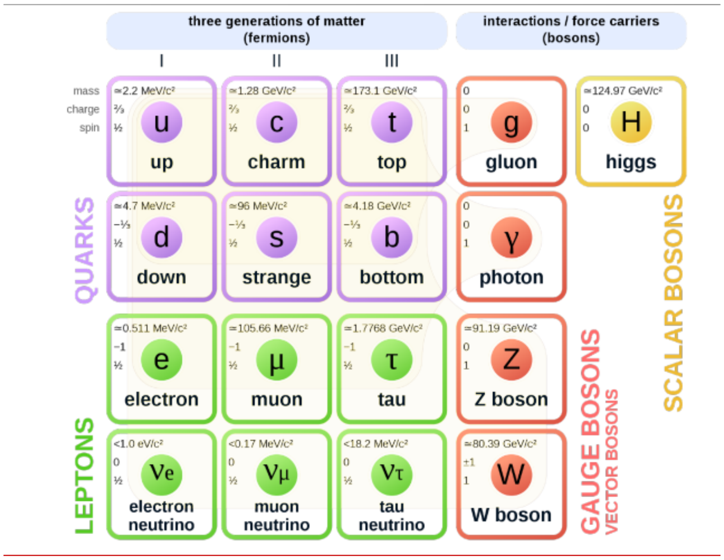

Figure 1: A schematic representation of the fundamental particles as defined from the Standard Model of Particle Physics. From Wikipedia

Neutrinos are classified as neutral leptons which means that the only forces they are subjected to are the weak interaction and the gravitational force. This results in the fact that they are not deflected by electromagnetic fields, that their half-life times are relatively long ($\sim 10^{-10}$ s) and that their cross sections for interactions are extremely small ($\sim 10^{-43}$ cm^2 at 1 MeV). These characteristics point towards the fact that, on one hand, neutrinos can probe phenomena happening deep inside the core of astrophysical objects since they are not easily deflected or absorbed, while their detection is difficult because of the extremely small cross section.

High energy neutrinos interact with matter mainly through charged current weak interaction (CC) or neutral current interaction (NC). The charged current weak interaction can be visualised as: $\nu_l + N \rightarrow l + X$, where ν_l represents a generic neutrino whose generation is l, N represents a generic nucleon, l is a charged lepton (electron, muon or tau) and X represents the hadronic system formed by the interaction carrying part of the incoming neutrino energy. Neutral current neutrino interactions, instead, can be outlined using the same formalism as above as: $\nu_l + N \rightarrow \nu_l + X$. The two processes have different cross sections as a function of energy, as can be observed from Figure 2 which refers to muonic neutrinos and anti neutrinos. However, for both processes it is possible to notice a linear rise for the cross section with energy until 10^4 GeV and a subsequent flattening.

Figure 2 furthermore shows why neutrino detectors have to occupy large volumes: even at high energy the probability of neutrinos interacting with a medium is extremely low, so the wider the volume surveyed by the detector, the higher the number of target nucleons the neutrino might interact with and the higher the probability of an interaction (Spurio, 2018).

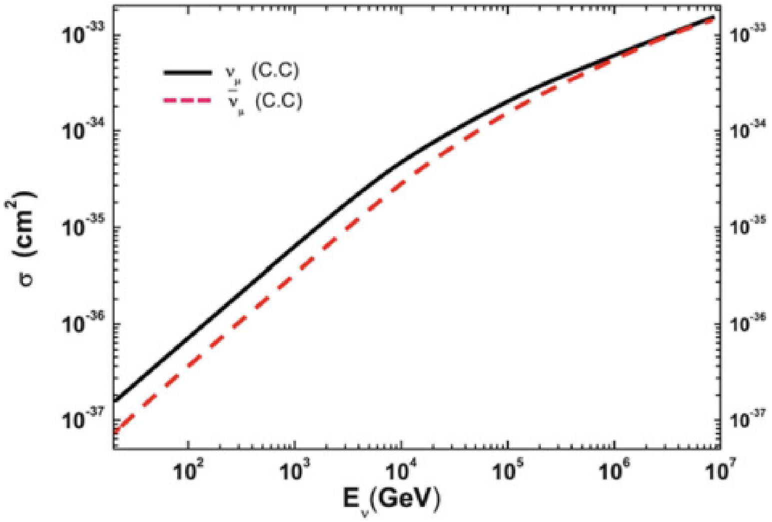

Figure 2: Cross-section for ν_μ and $\bar{\nu_\mu}$ as a function of their energy according to one particular distribution function of quarks in nuclei (CTEQ6-DIS). From Spurio (2018)

Neutrinos are produced by many different sources, either natural or artificial, some of whose are still unknown. A number of these are listed in Figure 3 together with the typical energies and cross sections for the neutrinos. It is possible to see how neutrinos cover a wide range of energies from 10^{-2} eV to 10^{18} eV. Figure 3 also shows that artificial sources of neutrinos such as nuclear reactor and particle accelerators, despite being able to reach considerable energies, cannot accelerate particles to the extreme energies reached by galactic and extragalactic neutrinos.
The different kinds of neutrinos mentioned in Figure 3 are:

- Cosmological neutrinos: produced during the Big Bang, they are essentially undetectable due to their low energy and cross section;
- Terrestrial neutrinos: they arise as a result of radioactive decays naturally occurring in the Earth such as the ones involving uranium, potassium and thorium;
- Solar neutrinos: they are a byproduct of the nuclear reactions powering the Sun such as the pp chain. Their flux was first measured by R. Davies in the 60s, in recent years their study allowed to discover neutrino oscillations (Volpe, 2015);
- Neutrinos from Supernova explosions: these energetic events release energies of the order of 10^{53} erg and 99% of this energy is expected to be converted in neutrinos. This paradigm was confirmed in 1987 thanks to the detection of some neutrinos in connection with the supernova 1987A in the Large Magellanic Cloud. Supernova neutrinos are connected to the study of the mechanisms causing the explosion of stars and the sites where heavy elements are formed (Volpe, 2015);
- Atmospheric neutrinos: arise from the interaction of high energy cosmic rays with atoms and molecules present in the Earth's atmosphere.

- Galactic and extragalactic neutrinos: they are able to reach extreme energies but their sources are yet to be conclusively identified. **The class of extragalactic neutrinos, in particular, is the one at the centre of this Thesis.**

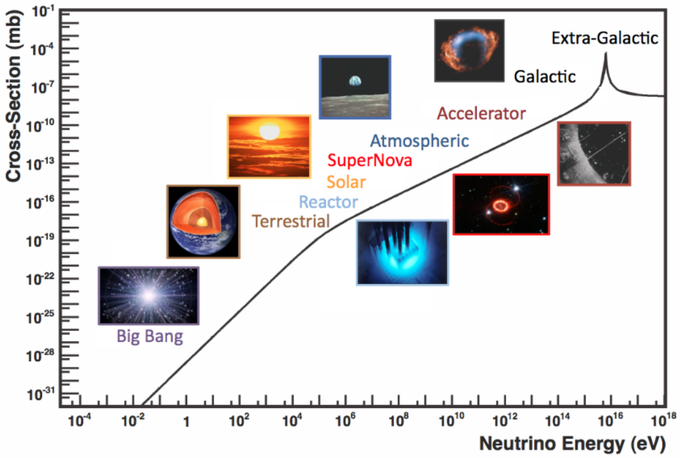

Figure 3: The neutrino cross-section (arising from the combination of different processes) as a function of energy, and related to various possible neutrino sources. From Formaggio and Zeller (2013)

1.1.1 Extragalactic Neutrinos

The IceCube observatory has detected a diffuse astrophysical neutrino flux at energies between TeV and PeV. The majority of this is thought to have an extragalactic origin. Neutrinos at such energies originate from the interactions of high energy cosmic ray protons with either photons or low energy thermal protons. Both processes produce neutral and charged pions. Neutrinos arise from the decay of the charged pions as shown in Equation 1, while the decay of neutral pions results in a gamma ray emission that can be revealed with telescopes.

$$\begin{cases} \pi^{\pm} \rightarrow \mu^{\pm} + \nu_{\mu} \rightarrow e^{\pm} + \nu_{e} + \nu_{\mu} \\ \pi^{0} \rightarrow \gamma + \gamma \end{cases} \tag{1}$$

The high-energy energy cosmic rays believed to be responsible for the high energy neutrinos production have an unknown origin. Their sources must be powerful accelerators of particles such as Active Galactic Nuclei, Gamma Ray Bursts and Tidal Disruption Events, among others. Both AGNs and GRBs are γ-ray emitters but the detection of such radiation is not sufficient to imply the acceleration of protons. Gamma rays in fact can arise by interaction between low energy photons and high energy electrons such as Inverse Compton effect and synchrotron self Compton. Only the detection of neutrinos represents a smoking gun for the acceleration of protons. In the following I provide an overview of the candidate sources of high-energy cosmic rays and high-energy neutrinos.

Tidal Disruption Events occur when a celestial body is pulled apart by tidal forces of a supermassive black hole. Some of the material is then captured by the supermassive black hole resulting in the formation of an accretion disk and a temporary electromagnetic flaring activity. TDEs have been added to the potential astrophysical accelerators only very recently when a high energy neutrino was associated with a tidal disruption event (Stein et al., 2021). The electromagnetic emission arising from this event showed a thermal spectrum in the X-ray and UV-optical band while radio observations show the presence of synchrotron emission from non thermal electrons hinting at particle acceleration (Stein et al., 2021). At present however, the connection between Tidal Disruption Events and neutrinos is still speculative (Winter, 2024).

Gamma ray bursts are short bursts of intense gamma-ray radiation lasting a few seconds and releasing energy between 0.1 and 1 MeV. They seem to originate either from hypernovae (catastrophic energy releases marking the endpoint in the evolution of massive stars) or from merging events between neutron stars. The simplest description for these phenomena is the one proposed by the relativistic fireball model: a highly relativistic expanding gas sphere able to heat the gas and drive a relativistic shock wave into it. If the sphere is optically thin, electrons can be accelerated via diffusive shock acceleration and give rise to the observed non thermal spectrum. As the expanding sphere decelerates a reverse shock is produced which reheats the gas. It is believed that cosmic rays too might be accelerated in the process (Longair, 2011). The maximum proton energies achievable in gamma ray bursts' shocks should be comparable to the ones of the highest energy cosmic rays. These accelerated protons can interact with the high-energy photons produced in the fireball generating neutrinos through photo-pion mechanisms (Gehrels et al., 2009). So far though no neutrino emission has been observed in coincidence with gamma ray bursts meaning that either the proton density in the bursts is too low with respect to the one required for the highest energy cosmic rays or the gamma ray bursts models employed so far have to be revisited (IceCube-Collaboration, 2013).

Other promising sources of extragalactic neutrinos are Active Galactic Nuclei. Around 10% of galaxies can be classified as active, their main peculiarity is that the supermassive black hole at their centre is accreting mass. This means that they are capable of releasing huge amounts of energy. The basic structure for an AGN is: a central black hole surrounded by a gaseous accretion disk, a X-ray emitting corona, a dusty obscuring torus and in some cases relativistc jets. The orientation of the galaxy with respect to the observer's line of sight results in the detection of different AGN components and therefore of different spectral characteristics. These spectral characteristics have been used to classify them. In particular about 10% of AGNs are classified as radio loud meaning that they have an excess of non thermal radiation in the radio band due to the presence of jets. The presence of shocks and magnetic fields in jets allows the acceleration of cosmic rays through diffusive shock acceleration or magnetic reconnection (Matthews et al., 2020). The most peculiar among radio galaxies are blazars. These are sources whose jet is oriented along the observer's line of sight so thee observed emission is completely dominated by the non-thermal jet emission. Their spectrum is shown in Figure 4, its main feature is the double hump. The first peak is due to sychrothron emission while the origin of the second peak is generally attributed to inverse Compton.

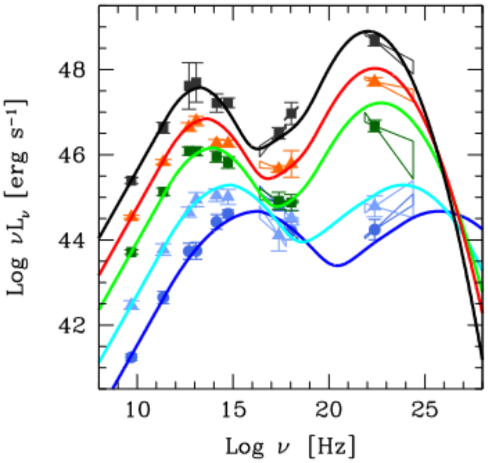

Figure 4: The SED of different blazars forming the blazar sequence. From Ghisellini (2016)

Non jetted AGNs are broadly referred to as radio quiet. Seyfert galaxies are a subclass of radio quiet AGNs characterised by a prominent UV-optical spectrum originating from the accretion disk. It is possible to distinguish two families of Seyfert galaxies on the basis of their optical spectrum: in Seyfert I galaxies the permitted emission lines are broader ($v \sim 10^4$ km s^{-1}) than the forbidden ones ($v \sim 10^3$ km s^{-1}), while in Seyfert II galaxies both permitted and forbidden emission lines show similar broadness ($v \sim 10^3$ km s^{-1}). The difference in their spectra seems to be related to the different optical depths along the line of sight. Seyfert I galaxies have a lower optical depth so radiation travels almost unabsorbed to the observer, while in Seyfert II galaxies the absorption results in thinner emission lines (Longair, 2011).
The IceCube observatory has provided evidence for AGNs to be extragalactic neutrino sources: for example, in 2017 it detected a neutrino event in spatial and temporal coincidence with the flaring activity of the blazar TXS 0506+056 (IceCube et al., 2018), while analysis of the integrated neutrinos events between 2018 and 2020 detected a signal in the direction of the Seyfert galaxy NGC1068 (IceCube-Collaboration, 2024). These are considered the first identifications of high-energy neutrino sources. While for blazars it was long known that they are able to accelerate particles to extreme energies, the identification of a Seyfert galaxy as a potential neutrino source came as a surprise (Neronov et al., 2023). It is still unclear whether all Seyfert galaxies produce neutrinos or NGC1068 is a special case. Particle acceleration in such sources should happen close to central black hole and might be related to accretion flows or weak jets. If Seyfert galaxies are neutrino sources, their intrinsic X-ray flux should scale with the neutrino luminosity (Neronov et al., 2023; IceCube Collaboration, 2024).

In summary, even though many different kind of sources have been proposed, at the time of the writing, the most promising candidate sources of high-energy neutrinos are AGNs, and the sources responsible for the bulk of the measured neutrino diffuse flux remain mysterious.

1.1.2 Detectors: IceCube

After having introduced the topic of extragalactic neutrinos, a brief overview on how they can be detected is required. The basic structure of a neutrino detector comprises of a set of detectors in a transparent medium such as ice or water. The detection happens via the collection of Cherenkov light in the detectors. Cherenkov light is emitted when charged particles travel through a medium faster than the speed of light in that medium. The passage of such a particle induces short lived electric dipoles concentrating along a narrow cone, when these dipoles relax they emit electromagnetic radiation. The emission angle of Cherenkov light with respect to the particle direction is:

$$\Theta_C = \cos^{-1}\left(\frac{1}{\beta n}\right) \tag{2}$$

where n is the refractive index of the medium, while $\beta = \frac{v}{c}$ and v is the velocity of the particle. In the air $\Theta_C \sim 1.4°$ while in water the angle is wider, $\Theta_C \sim 43°$ explaining why water tanks are usually employed to detect this effect. Since the emission of Cherenkov light in water peaks at wavelengths between 300 and 600 nm, detectors are composed of many photomultipliers tubes (PMT) sensitive to this band. PMTs can measure the number of photons and their arrival time and derive the neutrino flavour, direction and energy.
Two different kind of events are most commonly distinguished: tracks and showers. Their appearance on a detector is shown in 5: each dot is a module hit by a photon, each colour represents a different arrival time and each size how much light was detected.

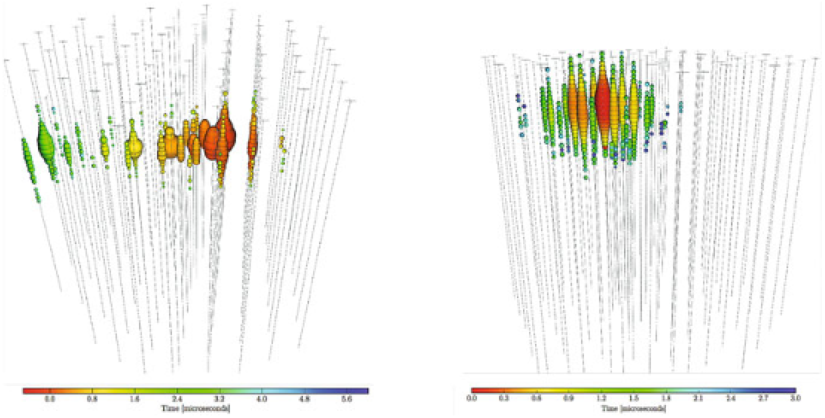

Figure 5: Left: an upward muon track. Right: the highest energy cascade event detected with IceCube as of 2018 with $\sim$ 2 PeV of energy released in the detector. From Spiering (2020)

Charged current weak ν_μ interactions usually leave tracks, while neutral current and charged current ν_e and ν_τ interactions generate showers.
As any other detector, neutrino telescopes are affected by the presence of a background. The definition of what constitutes a background strictly depends on the scientific goal. Since this work is focused on the study of extragalactic neutrinos (namely neutrinos with energies between 10^{14} and 10^{21} eV), the main background sources are the atmospheric neutrino flux, atmospheric muons. The atmospheric neutrino flux is an irreducible background component having two main contributions:

- the conventional flux (dominates below 100 TeV): it originates from the decay of kaons ($K \rightarrow \mu + \nu_\mu$) and pions ($\pi^\pm \rightarrow \mu + \nu_\mu$)
- the prompt emission (dominates above 100 TeV): it arises form the decay of charmed mesons resulting from cosmic ray interactions with atmospheric nuclei.

Atmospheric muons are produced together with the atmospheric neutrino conventional emission. As they can travel through several kilometers of water and ice, neutrino detectors have to be located under large amounts of shielding material in order to reduce the background.
Solar neutrinos are another source of background. They are produced by nuclear reactions happening inside the Sun's core. Given their energies, in the range between 400 keV and 15 MeV, they are not relevant for this Thesis's work.

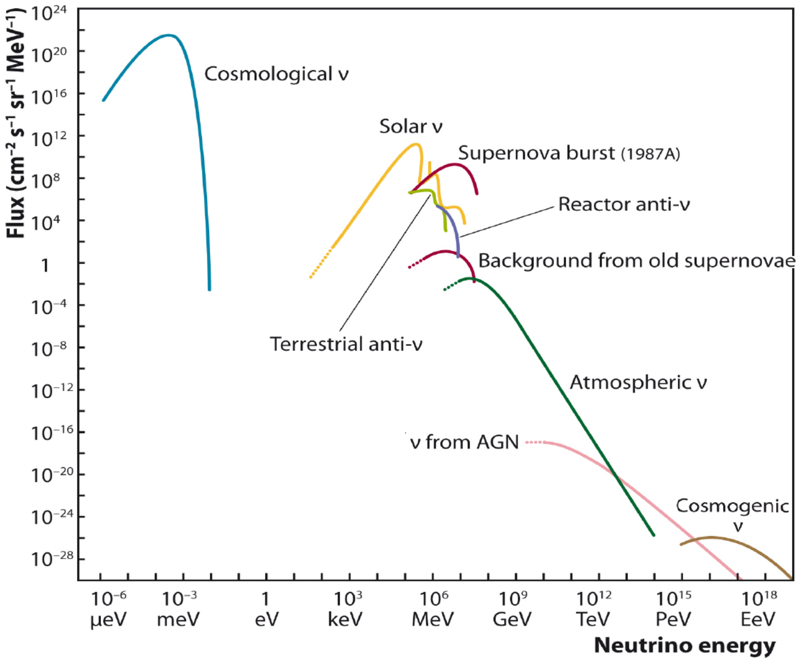

Figure 6: Expected neutrino fluxes and energies for different classes of sources. From IceCube Masterclass

IceCube is a neutrino observatory located at the geographic South Pole. It is sensitive to the passage of neutrinos having energy between 10^{11} and 10^{21} eV which, as show in Figure 6, means that the observatory is ideal to study extraglactic neutrino coming from AGNs. As shown in Figure 7, IceCube consists of an array of 5160 Deep Optical Modules located between 1.5 and 2.5 km deep and displaced over a 1 km^3 volume of transparent ice. Each Deep Optical module contains a photo-multiplier meant to detect Cherenkov radiation. The modules are arranged in 86 strings 8 of which constitute the Deep Core, namely a set of finer spaced detectors extending the observatory's sensitivity to lower energies. The observatory is completed by a surface cosmic ray detector. IceCube began operating in 2011 and until now it has been at the forefront of research on extragalactic neutrinos by discovering the neutrino diffuse flux between 2011 and 2013 and by localising the first possible extragalactic source of neutrinos in 2018 (IceCube et al., 2018).

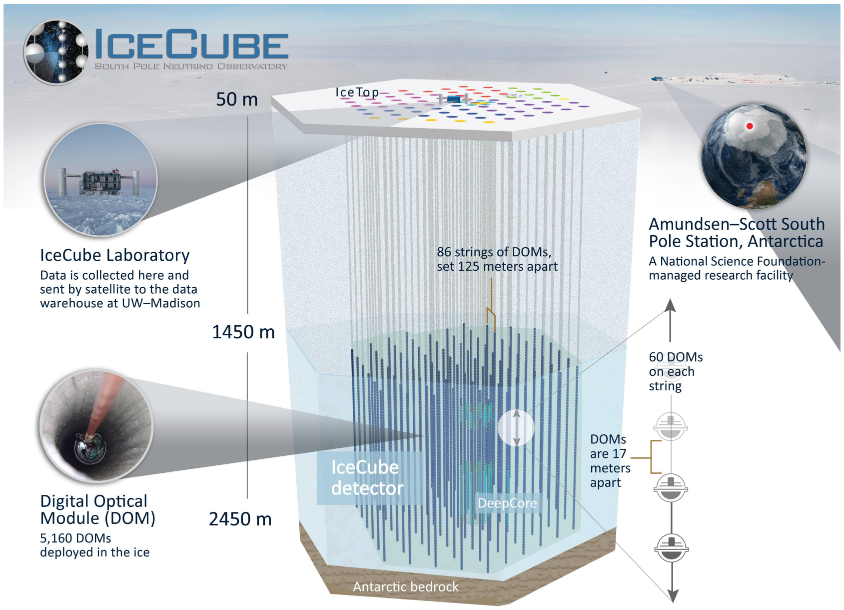

Figure 7: Schematic representation of IceCube observatory. From IceCube neutrino observatory page

1.1.3 IceCube neutrino diffuse flux

The data collected by IceCube between 2010 and 2013 show the presence of an excess of high energy neutrinos over the expected background (Aartsen and et al, 2013). Subsequent studies performed on the data acquired between 2010 (Aartsen and et al, 2015) and 2017 (Aartsen and et al, 2017) confirm the presence of a neutrino diffuse flux extending between 10 TeV and 2 PeV. Its spectrum as shown in Figure 8, is a power-law spectrum with a spectral index of -2.5 ± 0.1 (Aartsen and et al, 2017) and it is compatible with an equal flavour composition.

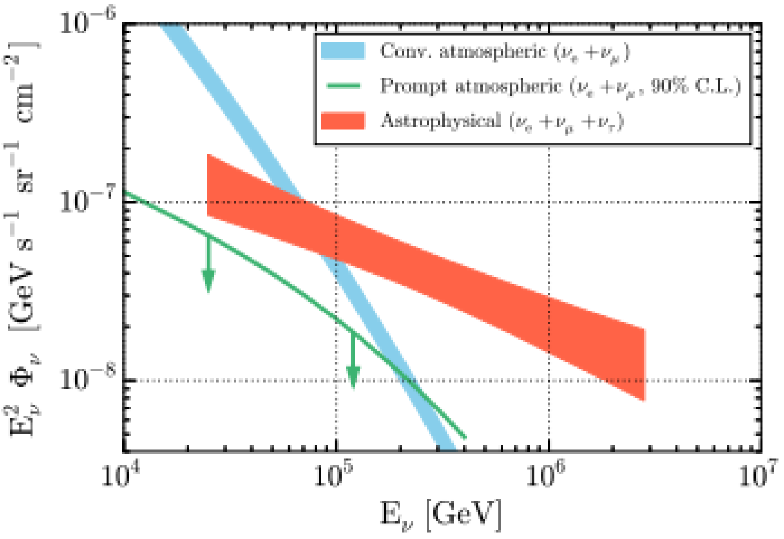

Figure 8: Spectrum of the extragalactic neutrino diffuse flux. From Aartsen and et al (2013)

This flux is found to be compatible with an isotropic distribution of sources suggesting that its origin might be extragalactic. Recent estimates find that only about 10 % of the diffuse flux can be ascribed to galactic emission (Collaboration, 2024). Among the sources listed in Section 1.1.1 AGNs seem to be the most plausible sources of the neutrino diffuse flux since the non detection of neutrinos associated with GRBs limits their contribution and the neutrino-TDE connection is not confirmed yet.
A first tentative study performed by Aartsen and et al (2017) tried to relate the observed neutrino diffuse flux with the position of 862 GeV emitting blazars selected form the *Fermi*-LAT 2LAC catalog. It was found that, assuming a proportionality between the γ-ray flux and the neutrino luminosities of the sources, the maximal flux contribution by all of the *Fermi*-LAT 2LAC blazars to the neutrino diffuse flux is less than 27%. More recent studies such as Buson et al. (2022) and Buson et al. (2023) suggest the presence of a spatial correlation between a subset of blazars and the neutrino diffuse flux. The two studies analyse possible correlations between the positions of neutrinos detected between 2008 and 2015 and the positions of blazars listed in the 5th release of Roma-BZCat catalog. One of the main differences with Aartsen and et al (2017) lies in the choice for the blazars' sample. The Roma-BZCat catalog has no preferred selection based on the wavelength or survey strategy. The analysis calculates a post trial p-value of 2.59×10^{-7} for the cross-correlation analysis thus pointing at blazars as the first population of high energy neutrino sources discovered. Among these, 52 sources flagged as candidate PeVatron blazars are highlighted as possible counterparts for the neutrino emission. Such sources seem to be only weak γ-ray emitters since only 22 of them are listed in the Fermi catalog. This feature might be related to the interaction between gamma rays and lower energy photons producing electron-positron pairs. On the other hand, PeVatron blazars seem to show a strong radio power $P_{1.4GHz} \geq 10^{26}$ W Hz^{-1} typical of high-excitation radio galaxies (HERG).
Other studies, instead, focus instead on the contribution from non-jetted AGNs, such as Seyfert galaxies, to the neutrino diffuse background. In (Padovani et al., 2024) the X-ray flux of AGNs is related to their neutrino emission, as suggested by previous works such as Neronov et al. (2023). In particular, the

approach in Padovani et al. (2024) employs the X-ray Luminosity Function as a measure of the total X-ray flux from AGNs, which is then converted into an estimate for the total contribution to the extragalactic neutrino flux. Their results, shown in 9 seem to suggest the possibility that non-jetted AGNs contribute to the diffuse background at energies below 1 PeV while blazars might dominate the higher-energy part.

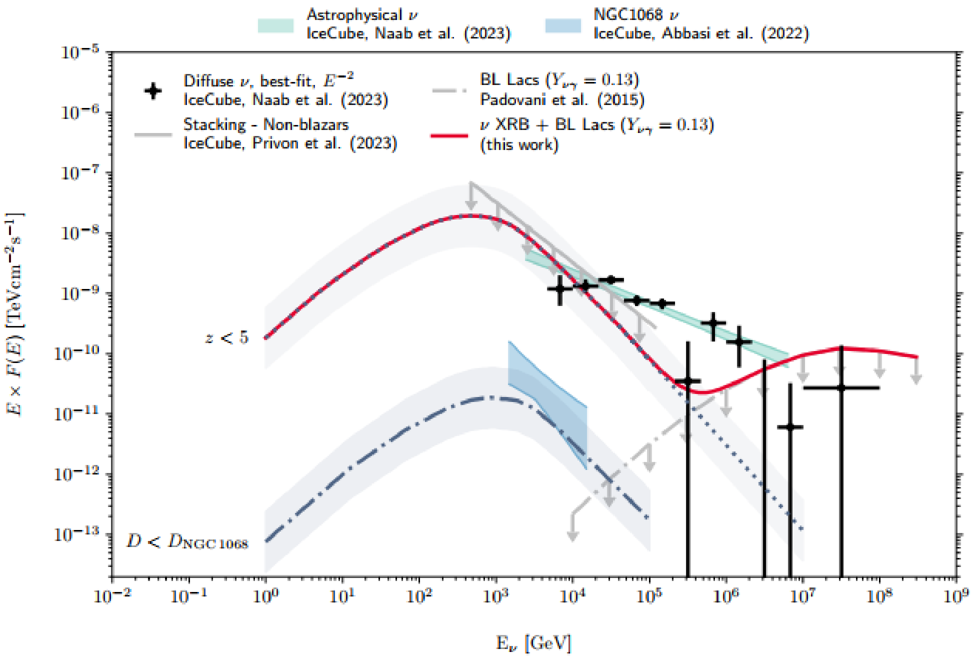

Figure 9: Computed all-flavour neutrino background derived from an X-ray AGN population synthesis. Dark blue curves show the computed neutrino backgrounds for source populations integrated up to the distance of NGC1068 and redshift $z = 5$ (dash-dotted and dotted, respectively). A high energy extrapolation up to 107 GeV is added to the integrated spectrum for $z = 5$ and combined with the blazar neutrino background model (dash-dotted grey curve) to highlight the structure of the combined AGN neutrino background flux ("double-humped" red solid curve). The estimated uncertainty on the integrated neutrino component from X-ray AGN is assumed to be 0.5 dex (dark blue band). Also shown are the current best-fit astrophysical diffuse neutrino flux and the segmented neutrino flux fit assuming an E^{-2} energy spectrum in each bin (green area and black points), IceCube upper limits from stacking analyses for non blazar AGN. From Padovani et al. (2024)

My Thesis uses as starting point the findings of Buson et al. (2022, 2023) and investigates the contribution of active galactic nuclei, star formation and cosmic shocks to the diffuse neutrino background using ENZO cosmological simulation.

1.2 Cosmic Rays

As seen in the previous Section, most known astrophysical mechanisms for the acceleration of neutrinos are tightly associated with the acceleration of cosmic rays, and therefore a minimal introduction to their properties is in order.

Cosmic Rays are high energy particles accelerated by astrophysical sources reaching the Earth form outside the Solar System. They are composed by 87% protons, 12% helium nuclei, 2% electrons and 1% heavy nuclei such as carbon, oxygen, and iron (Longair, 2011). Since the vast majority of cosmic rays are charged particles, they are significantly deflected by magnetic fields. A measure of this deflection is given by the gyroradius: $r_g = \frac{mv_\perp}{|q|B}$ for a non relativistic particle.
When cosmic rays interact with the atoms and molecules present the Earth's atmosphere they produce a cascade of secondary particles such as pions, muons, electrons positrons, neutrinos and electromagnetic radiation. All of these byproducts constitute an extensive shower and their detection provides insights on the energy of the particles initiating the shower (Longair, 2011).

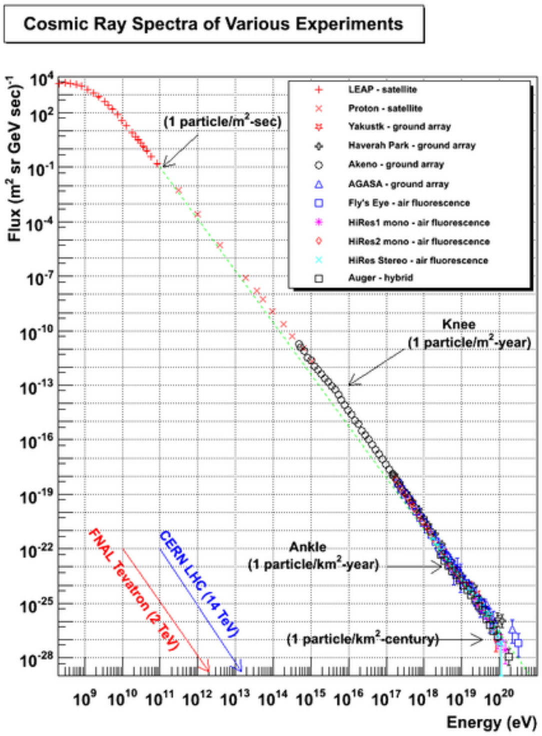

Figure 10: Spectrum of cosmic rays from different experiments. From Updated Cosmic Ray Spectrum

Figure 10 shows the complete cosmic ray spectrum as obtained from different experiments. As shown these particles have a wide energy range extending for more than 10 orders of magnitude from 10^9 to 10^{21} eV. The spectrum can be well represented by a power-law distribution of the form $N(E)dE = KE^{-\alpha}dE$. Figure 10 highlights the presence of two main features: the knee at about 10^{15} eV and the ankle at about 10^{19} eV. Such features mark a change in the spectrum's slope: for energies below the knee $\alpha \sim 2.6$, for energies below the ankle the spectrum is steeper with $\alpha \sim 3.1$ while for energies above the ankle $\alpha \sim 2.7$ (Spurio, 2018). As outlined in Figure 10, cosmic rays with different energies have different integral fluxes: particles with lower energies have higher fluxes ($\sim$ 1000 particles/s/m^2) with respect to higher energy ones ($\sim$ 1 particle /year/km^2).

1.2.1 Galactic Cosmic Rays

Cosmic rays with energies below the ankle are thought to be of galactic origin since their gyroradius is of the same order of magnitude or smaller than the scale height of the Milky Way's disk ($\sim$ 200 pc). Those particles are likely to be accelerated via Diffusive Shock Acceleration in supernova remnants.
The chemical abundances of cosmic rays provide useful insights on the origin and propagation towards the Earth. Figure 11 shows a comparison between the abundance of elements in the cosmic rays and in the Solar neighbourhood. It is possible to notice that the two distributions are not so different from each other: in particular the peaks at carbon, nitrogen, oxygen and iron group are present in both. The main differences in the cosmic rays instead are: an overabundance of light elements (lithium, beryllium and boron), a higher fraction of elements with atomic and mass numbers below those of iron (such as calcium, titanium and chromium) and an underabundance of hydrogen and helium with respect to heavier elements. These differences can be explained by considering the processes cosmic rays undergo during their propagation from the source to the Earth. In particular, collisions with the interstellar medium can fragment cosmic ray nuclei resulting in the production of species with lower atomic and mass numbers (Longair, 2011). Such particles are known as secondary cosmic rays and the process generating them is known as spallation. The production of secondary cosmic rays depends on the average density of the interstellar medium (ρ_{ISM}) and on the characteristic residence time (τ) inside the galaxy therefore it is possible to define a quantity $\xi = c \cdot \rho_{ISM} \cdot \tau$ known as path length or grammage (Spurio, 2018). The ratios between the abundances of primary and secondary cosmic rays allow to infer the grammage which is a proxy for the average amount of interstellar matter traversed by cosmic rays before leaving the confinement volume. For example the boron to carbon ratio has a value of $R_{B/C} = 0.25$ which corresponds to a path length of $\xi = 5$ g cm^{-2}. Since the path length is also equivalent to $\xi = x \cdot \rho_{ISM}$ where x is the distance travelled by particles since their production until the exit from the Galaxy. The value of x obtained from $R_{B/C}$ is of the order of 1 Mpc which is much higher than the estimated radius of the Milky Way ($\sim$ 15 kpc). This result hints towards a propagation model for cosmic rays resembling a random walk. The average confinement time is estimated to be of the order of 1 Myr (Spurio, 2018), however this value depends on the energy and lowers for higher energy particles. Another way of determining the confinement time is by measuring the abundance of certain radioactive isotopes with known decay times such as ^{10}Be, ^{26}Al, ^{36}Cl, ^{54}Mn . In this case the estimate is independent of the assumed average density for the ISM.

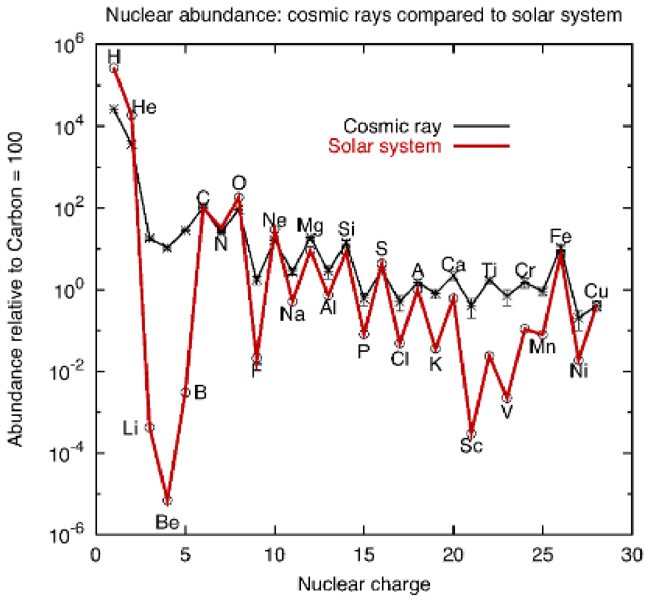

Figure 11: The chemical composition of cosmic rays. From Particle Astrophysics Lecture 3

The model used to describe the propagation of cosmic rays inside the Milky Way is known as the leaky box model: high energy particles diffuse freely in a cylindrical volume of radius ~ 15 kpc and height ~ 200 pc and are reflected at the boundaries. At each encounter with the boundary there is a non zero escape probability and their escape time depends on the particle's energy (Longair, 2011).
A crucial role in the confinement and diffusion of cosmic rays is played by the galactic magnetic field. Information of the Milky Way's magnetic field are provided by measurements of Faraday rotation, by the synchrotron radio emission and by the polarised dust emission. Its average intensity is of the order of a few μG but it has strong fluctuations and shows a decline from the central regions to the outskirts of the galaxy. Two main components can be distinguished: a disk like structure and a halo.
The magnetic field in the disk is mainly oriented parallel with respect to the galactic plane and its lines follow the spiral arms (Spurio, 2018).
The halo component of the magnetic field extends above and below the galactic plane and it seems to have a toroidal shape. The region above the galactic plane and the one below seem to have opposite orientation (Shaw et al., 2023).

1.2.2 Ultra High Energy Cosmic Rays

Ultra High Energy Cosmic Rays are particle with energies above 10^{18} eV, they have a power-law spectrum but its slope is poorly constrained due to the rarity of the detection. In fact, the arrival rate for such particle is of only 1 particle/km^2/century. Therefore the determination of the UHECRs' composition is challenging due the presence of fluctuations between the showers (Spurio, 2018).
Since a cosmic ray with energy of 10^{18} eV has a gyroradius of the order of 300 pc which is of the same order of magnitude as the galactic height and no galactic source is known to accelerate particles to such extreme energies, UHECRs are thought to be of extragalactic origin. Another proof of their

extragalactic origin lies in their isotropy in the direction of the galactic centre (Spurio, 2018). Their sources have not been identified yet, among the ones proposed there are Gamma Ray Bursts, Active Galactic nuclei, magnetars (Spurio, 2018) and Tidal Disruption Events (Winter, 2024). The nature of UHECRs is fundamental for the determination of their sources. If the primary particles are mainly protons their acceleration sources seem likely to be GRBs or AGNs, while if they are mainly heavier nuclei their sources might be magnetars (Spurio, 2018). This happens because since magnetars are highly magnetized neutron stars, they possess an iron rich surface that might inject large quantities of heavy nuclei in an acceleration region.

An argument proposed by Greisen, Kuzmin and Zatsepin predicts that the highest energy cosmic rays must have originated within a few tens of Megaparsecs from our galaxy. In particular, if they are composed mainly by protons, their sources should lie within 30 Mpc from the Milky Way, while if they are mainly composed by heavier nuclei they should have originated within 80 Mpc. This is due to the fact that the photons of the Cosmic Microwave Background permeating the Universe possess high energies in the cosmic rays' reference frame hence they are available partners for photo-pion and pair production. This means that a cut off in the cosmic ray spectrum should exist at energies of about 5×10^{19} eV (Longair, 2011). If instead Ultra High Energy Cosmic Rays are composed mostly by heavier nuclei, the cut off should be detected at energies $E \sim 10^{20}$ eV (Spurio, 2018).

The study of anisotropies in the arrival direction of UHECRs located excesses in the position of the radiogalaxy Centaurus A (Collaboration, 2015). Studies such as Collaboration (2018) instead, found a possible correlation between the arrival directions of UHECRS and the positions of both AGNs and star-forming galaxies. The explanation suggested by Bell and Matthews (2022) is that the particles are accelerated in radio-galaxies and later scattered by the magnetic field of starburst galaxies. In this framework starburst galaxies reflect the echoes of the past activity of radio-galaxies.

Since interactions between cosmic rays and nucleons produce neutrinos, high energy neutrinos and UHECRs are believed to originate form the same sources. Furthermore, neutrino astronomy is believed to be of paramount importance in order to determine the sources of UHECRs since they travel almost undeflected from their production sites to the Earth.

1.2.3 Diffusive Shock Acceleration

The Diffusive Shock Acceleration is believed to be the most ubiquitous acceleration mechanism for cosmic rays in the Universe. It describes the production of a non thermal tail of particles injected from the high energy end of a thermal distribution. Its main strength relies on the fact that the energy distribution of the accelerated particles results in a power-law distribution, without requiring any fine tuning. The basic mechanism involves collisions between charged particles and magnetised clouds in the presence of shocks or of a turbulent medium. The nature of the collisions is usually thought to be electromagnetic scatter. The following treatment is mostly presented in Matthews et al. (2020) and it contains the basic ideas developed by Enrico Fermi in 1949. Let us consider N_0 particles with initial energy E_0 undergoing scattering processes in which they gain energy. For each collision the fractional gain in energy is β_i so that after k collisions the particles have an energy $E = E_0 \Pi_{i=1}^{k} \beta_i$. Let us denote with P the probability that a particle is still present in the acceleration region after one collision undergoing other collisions. After k collisions the number of particles in the acceleration region is $N = N_0 \Pi_{i=1}^{k} P_i$. It follows:

$$\frac{\ln{(N/N_0)}}{\ln(E/E_0)} = \frac{\Sigma_{i=0}^{k} \ln(P_i)}{\Sigma_{i=0}^{k} \ln(\beta_i)} \tag{3}$$

The observed cosmic ray spectrum is consistent with a power-law distribution for the differential number of particles $n(E) = dN/dE$ and this is possible only if $\frac{\Sigma_{i=0}^{k}\ln(P_i)}{\Sigma_{i=0}^{k}\ln(\beta_i)}$ is constant. One way to achieve this is when P_i and β_i are constant with increasing particle energy, in this case it is possible to label them as P and β. The differential number of particles then becomes

$$n(E)dE \propto E^{(\ln(P)/\ln(\beta))-1}dE \tag{4}$$

This proves that if P_i and β_i remain constant with increasing energy, particles undergoing stochastic collisions can produce a power-law distribution of particle energies. Furthermore, DSA theory allows to compute the value for the exponent $\ln(P)/\ln(\beta) - 1$ by relating it to the strength of the shock. Since shocks are collisionless, the impacts do not happen as particle-particle encounters but they are collective plasma processes, in particular they are deflections in a turbulent magnetic field. However, the process can be thought as interactions between magnetised clouds and particles. Every time a particle crosses the shock front (in either directions) it receives a small increase in energy. Scattering ensures that the particle distribution in front of and behind the shock is isotropic. In more detail, let us consider a relativistic test particle with velocity $v_p = c$ and energy $E = pc$ and a non-relativistic shock having velocities u_1 and u_2 upstream and downstream respectively as represented in Figure 12.

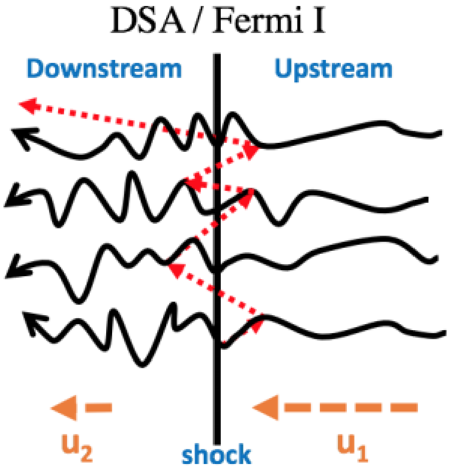

Figure 12: The Figure shows how particles are accelerated according to DSA mechanism. From: Matthews et al. (2020)

Let us consider a steady state solution in which the number of particles being injected in the shock is equal to the number of particles being carried away downstream. The energy of the particle travelling from the upstream to the downstream region is given by a Lorentz transformation:

$$E' = \gamma_s(E + 3pu_2\cos\theta) \tag{5}$$

where γ_s is the Lorentz factor, θ is the angle with respect to the shock's normal and $3u_2$ is the downstream velocity of a strong shock with respect to the upstream plasma. By integrating over the pitch angles, we obtain that the fractional increase in energy is $4u_2/c$ per full cycle hence

$$\ln(\beta) = \ln\left(1 + \frac{4u_2}{c}\right) \sim \frac{u_1}{c} \tag{6}$$

From Equation 6 it is possible to notice that the energy gain per collision is first order in the shock velocity, making DSA an attractive acceleration mechanism. The probability P of a particle remaining in the acceleration region after being scattered is determined by considering that the particles being swept up by the shock is Nu_2 while the number of particles crossing the shock is $Nc/4$. Which means that the fraction of particle lost from the acceleration site is $(1 - P) = 4Nu_2/Nc$. Thus we obtain:

$$\ln(P) = \ln\left(1 - \frac{4u_2}{c}\right) \sim -\frac{u_1}{c} \tag{7}$$

It is possible to notice that neither the rate at which particles leave the acceleration site nor the fractional energy gain depend on the energy but only on the velocity of the shock. By substituting Equations 6 and 7 in Equation 3 we obtain

$$n(E)dE \propto E^{-2}dE \tag{8}$$

Which represents a great success for the theory since it is very similar to the observed spectrum of cosmic rays as seen from the Earth.
One of the main drawbacks of the theory is the so called ”injection problem”. The particle undergoing DSA acceleration are injected from a Maxwellian distribution, however the minimum energy or momentum required for a particle to enter the acceleration cycle are unknown. The most common assumption is that the injection momentum p_{min} is a multiple of the post shock thermal momentum $p_{th} = \sqrt{2m_pk_bT_d}$:

$$p_{min} = q_{inj}p_{th} \tag{9}$$

where q_{inj} represents the injection threshold ranging between 3 and 4. The actual value of q_{inj} is difficult to constrain because there is only a smooth range of values for the momentum each having a different probability of starting the acceleration. At the same time, since the slope of the Maxwellian distribution at high energies is steep, even a small difference in the determination of p_{min} can result in large differences in the energy and number of cosmic rays entering the acceleration cycle (Longair, 2011).

1.3 Gamma-rays

Similarly to cosmic rays, γ-rays are an unavoidable by product of the most plausible mechanisms for the acceleration of high energy neutrinos. This section provides a short introduction to their astrophysical relevance in the context of this Thesis. Gamma-rays is a term broadly referring to the electromagnetic radiation with energies above the MeVs. The photon flux at the highest energies presents a non-thermal spectrum. Two different mechanisms are thought to be responsible for the production of γ-rays in most astrophysical sources: the leptonic model and the hadronic model (Spurio, 2018).

In a leptonic model the high-energy emission is believed to originate from the interaction of low energy photons and high-energy electrons travelling through a magnetized medium via synchrotron Self-Compton mechanism. This means that electrons moving in a magnetic field generate electromagnetic emission with a broad spectrum extending form the infrared to the X-rays (synchthron emission). The same population of photons is then further accelerated by inelastic collisions with their own parent electron population via Inverse Compton Scattering. The resulting SED is shown in Figure 13, its main feature is presence of two peaks, the one at lower energies is produced by the synchtothron emission, while the one at high energies is produced by the Inverse Compton scattering (Spurio, 2018).

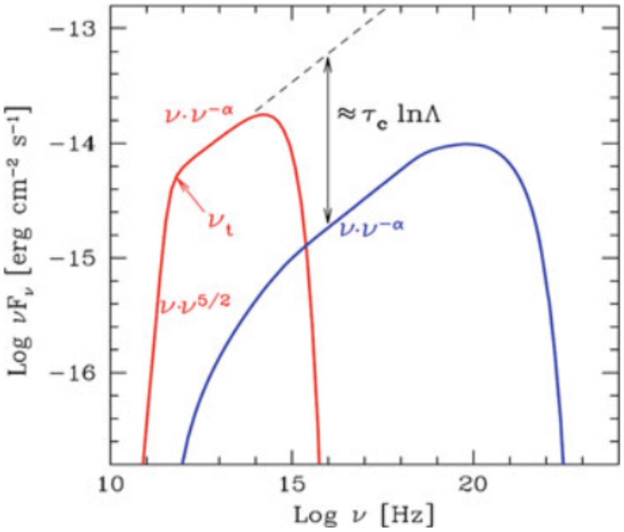

Figure 13: The figure shows an example of the SED for photons produced in the leptonic model. From Spurio (2018)

The hadronic mechanism involves the production of high energy photons by accelerated protons. The main interactions involved are either between high energy protons and low energy thermal protons (proton proton collisions) or between high energy protons and photons (photoproduction) (Spurio, 2018). In both cases the main byproduct of the interactions are charged and neutral pions. Gamma-rays arise from the decay of neutral pions while charged pions decay into neutrinos as described in Equation 1. The detection of neutrinos is therefore a clear evidence of the hadronic mechanism being in place (Spurio, 2018). If a power-law spectrum of the form E^{-2} is assumed for the parent proton population, the γ-ray spectrum due to hadronic mechanisms is characterised by a steep rise up to 200 MeV and approximately follows the energy distribution of the parent population at energies above a few GeV (Spurio, 2018).

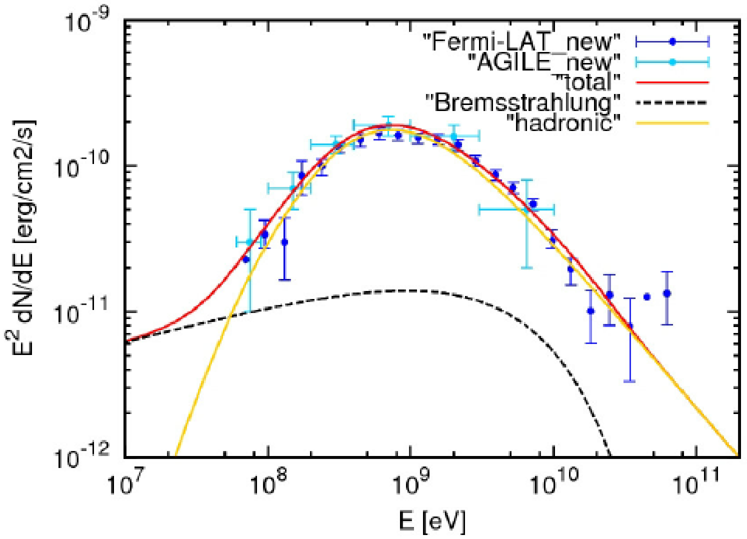

Figure 14: The figure shows a model for the gamma ray spectrum of the supernova remnant W44. In yellow it is possible to appreciate the γ-ray emission from hadronic mechanism. From Cardillo et al. (2014)

1.3.1 Fermi-LAT telescope

The Earth's atmosphere is opaque to the high-energy electromagnetic radiation. Therefore, in order to study γ rays, space-based instruments are needed. The *Fermi*-LAT is the most sensitive γ-ray telescope, it was launched in 2008 and dramatically improved our knowledge of γ-ray emission in the range between 20 MeV to 300 GeV. It is a pair conversion telescope, where γ-ray photons are converted into an electron-positron pair by interacting with the instrument. In more detail, the telescope's tracking section is made of 36 layers of silicon strips meant to record the tracks of charged particle (electrons and positrons) interspersed with 16 layers of tungsten foil meant to interact with the high energy photons and promote their conversion. The tracking section is coupled with a calorimeter able to estimate the energies of the charged particles and an anti-coincidence detector which identifies and rejects background cosmic ray events (Spurio, 2018). Thanks to this complex apparatus, *Fermi*-LAT is able to estimate the arrival time, energy and direction of the incoming γ-rays.

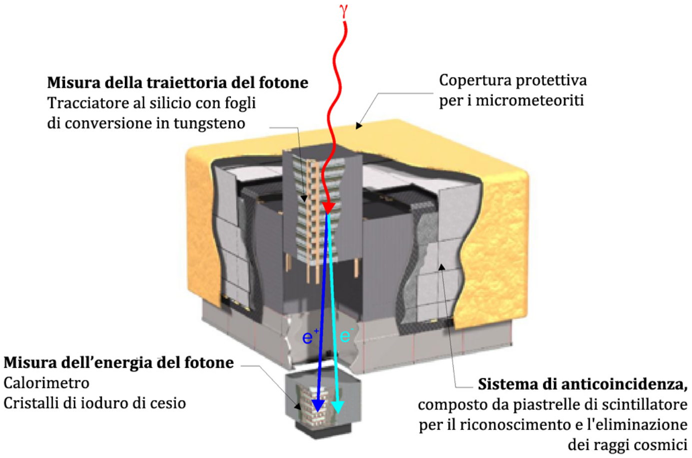

Figure 15: The figure shows the tracker, the anti-coincidence detector and the calorimeter onboard *Fermi*-LAT. From MediaINAF

1.3.2 Extragalactic Gamma-Ray Background

This study will exploit the simulated γ-ray background as a first calibration for our neutrino models hence an overview about this topic seemed to be required. The Extragalactic Gamma-Ray Background (EGB) was first detected in the 70s by the OSO-3 satellite but *Fermi*-LAT provided useful insights about its origin and characteristics. It comprises of both an individual and a diffuse γ-ray emission extending from the edge of the Milky Way to the edge of the Universe (FermiLAT-Collaboration, 2014). Diverse phenomena are expected to contribute to its emission among them: AGNs, Gamma-Ray Bursts, star-forming galaxies, galaxy clusters and shocks. While blazars' emission is sufficiently bright that many sources have been detected even at high redshift, for other populations such as star-forming galaxies and AGNs with misaligned jets, the cumulative emission is mostly unresolved. Therefore, scaling relations and theoretical models are needed to predict their contribution to the EGB (FermiLAT-Collaboration, 2014).

At energies above 100 GeV, interactions of high energy cosmic rays or γ-ray photons and the Electromagnetic Background Light can contribute to the Extragalactic Gamma-Ray Background. Furthermore some studies suggest that even more exotic processes could be at work such as Dark Matter annihilation or Dark Matter decay (FermiLAT-Collaboration, 2014).

As more sensitive instruments have been built, their ability to resolve individual sources of the EGB has increased. Recent studies estimated that 86% of the EGB at energies above 50 GeV is resolved by point sources, mostly blazars (di Mauro, 2016). However, even subtracting the emission due to individual sources from the EGB, still there is a residual component left. Such component is known as the Isotropic diffuse Gamma-Ray Background, since it is found to be isotropic on large angular scales. Its intensity is observation dependent, since deeper exposures can detect fainter sources (FermiLAT-Collaboration, 2014). The IGRB spectrum is a power-law spectrum of the form

$$\frac{dN}{dE} = I_{100}\left(\frac{E}{100MeV}\right)^{-\gamma}\exp\left(\frac{-E}{E_{cut}}\right) \tag{10}$$

The exact origin of the IGRB is still a mystery. Part of it is believed to be a superposition of multiple unresolved point sources (di Mauro, 2016). Since blazars are the most common sources found in the *Fermi*-LAT catalogs, they are thought of being responsible for most of the IGRB emission. In particular, they seem to be responsible for about 10% of the low energy portion (E≤ 50 GeV) and almost entirely for the high energy portion (di Mauro, 2016). AGN with misaligned jets should be responsible for a large part of the background at any energy, on average between 30% and 40%. However since their detection in the γ-ray band is difficult due to their faintness, the predictions upon their contribution suffer from large uncertainties (di Mauro, 2016).
The lack of detections of star-forming galaxies in the γ-ray band with respect to infrared and radio wavelengths suggest the existence of a population of unresolved star-forming galaxies. They should emit gamma rays because of interactions between cosmic rays and the Inter-Galactic Medium. The contribution of star-forming galaxies is estimated to range between 4% and 23%. Their contribution peaks between 0.1-1 GeV as visible form Figure 16.

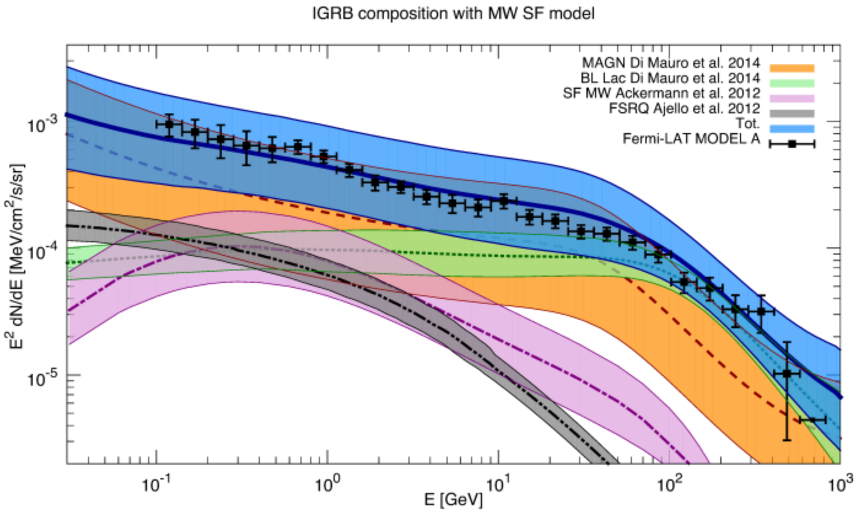

Figure 16: The figure shows the spectrum of IGRB (black dots) and contributions from different sources to it. From di Mauro (2016)

1.4 Cosmic Shocks

As discussed in Section 1.2.3, among the most important mechanisms to inject high-energy cosmic rays is the acceleration by shock waves in a plasma. Shocks also represent one of the most important injection mechanisms included in the cosmological simulations used in my Thesis, hence a short overview is useful here. Shocks are irreversible discontinuities of a medium's thermodynamic state propagating through the medium itself. Figure 17 describes the possible formation of a shock: if we assume a density perturbation having the profile of a sinusoidal wave propagating adiabatically through the medium, the sound speed will depend on the fluid's density as $c_s^2 \sim \rho^{\frac{2}{3}}$. On the perturbation's crest will propagate faster with respect to the valley causing the profile's distortion.

Figure 17: The figure shows the formation of a shock from an initial sinusoidal wave. Adapted from Pozzi (2014)

Across the shock, thermodynamic variables such as the gas temperature, density, and velocity are discontinuous, however conservation laws still apply and this allows us to derive relations between the flow of variables through the shock wave. The conservation of mass, momentum and energy yield the following system of equations where the subscript 1 indicates the gas before being shocked while the subscript 2 indicates the gas after being shocked:

$$\begin{cases} \rho_1 v_1 = \rho_2 v_2 \\ \rho_1 v_1^2 + p_1 = \rho_2 v_2^2 + p_2 \\ \epsilon_1 + \frac{p_1}{\rho_1} + \frac{v_1^2}{2} = \epsilon_2 + \frac{p_2}{\rho_2} + \frac{v_2^2}{2} \end{cases} \tag{11}$$

Here ρ symbolises the density, p the pressure, v the velocity and ϵ the energy.
The strength of a shock wave is usually quantified through the Mach number, namely the ratio between the speed of the pre-shock gas in the shock's rest frame and the speed of sound in the fluid: $M = \frac{v_1}{c_s}$. On the basis of the Mach number shocks can be classified in weak ($M \sim 1$) and strong shocks ($M \gg 1$). Weak shocks are characterised by small discontinuities of the thermodynamic quantities, a small compression rate of the gas and moderate gas heating. Strong shocks, instead, have higher gas compression rates, make the supersonic gas subsonic and convert bulk energy into internal energy.
The formation and growth of cosmic structures implies the formation of shock waves (Bykov et al., 2019). Structure formation theory predicts that galaxies and galaxy clusters form through the infall of matter onto Dark Matter halos. Figure 18 shows the evolution of the gas density in the simulated volume considered in this Thesis highlighting the collapse of gas into bound structures. The transition between a smooth accretion of matter and the virialisation of the halo is marked by the development of strong accretion shocks ($M \geq 10 - 10^2$). Such accretion shocks are predicted to dominate the statistics of shocks in the Universe (Bykov et al., 2019).

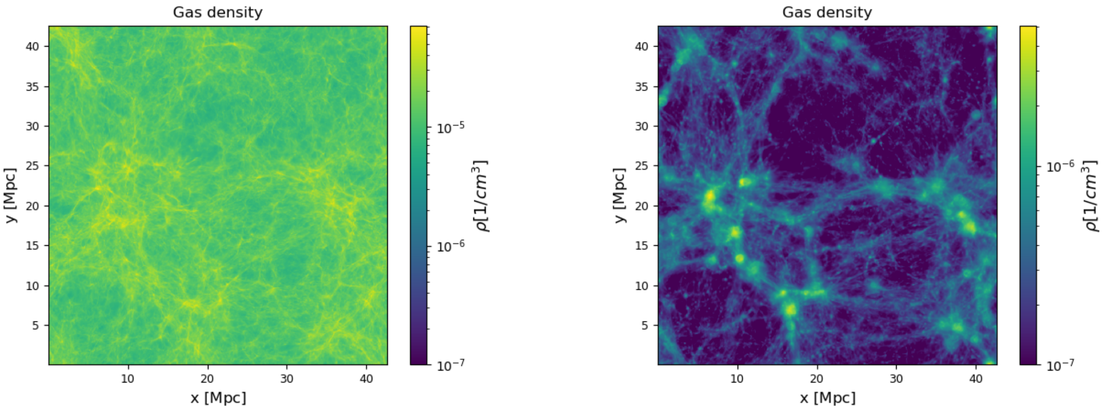

(a) (b)

Figure 18: The two figures show the gas density morphology from a quasi-uniform distribution at redshift 2.8 (*on the left*) to a clustered one at redshift 0.01 (*on the right*) as predicted by theories of structure formation. The figures are taken from the simulation described in 3.2 as Model B.

According to cosmological simulations, the bulk of the gas kinetic energy in a cosmic volume is dissipated within the large scale structure by shocks having $2 < M < 4$. These shocks are often associated with major mergers and are expected to accelerate cosmic rays. Cosmological simulations predict that cosmic rays accelerated by structure formation shocks should be volume filling, affect the dynamics of gas inside clusters and they might also be responsible for the emission of radio relics (Bykov et al., 2019). The main problems of simulating cosmic rays accelerated by shocks are their transport and their acceleration efficiency. Cosmic ray transport is driven by magnetic fluctuations of different scales which may arise from the conversion of the shock energy into the amplification of magnetic fields. The main difficulty here is represented by the broad range of dynamical fluctuations that should be modelled which falls well below the resolution of even modern simulations (Bykov et al., 2019).
The acceleration efficiency for cosmic rays is defined as the fraction of cosmic rays' energy flux and the kinetic energy dissipated by the shock: $\eta(M) = \frac{f_{CR}}{f_{diss}}$. The value for the acceleration efficiency is not known and needs to be set on the basis of other works (Bykov et al., 2019). Figure 19 displays some the acceleration efficiency functions employed in the literature.

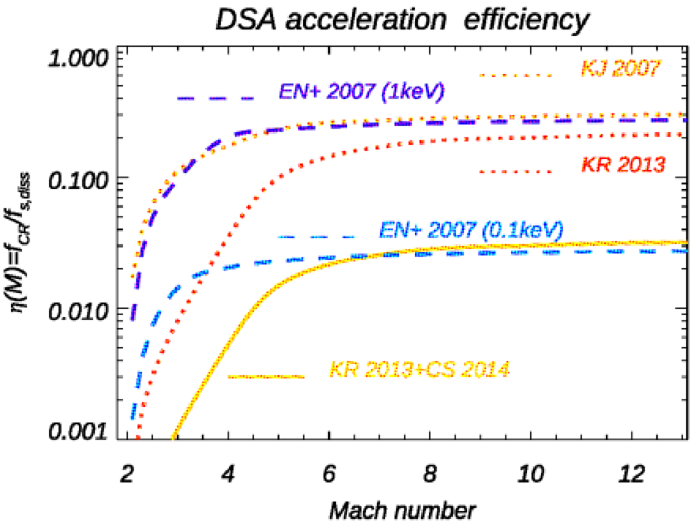

Figure 19: The figure shows different proposed acceleration efficiencies function $\eta(M)$ as a function of shock Mach number. The various models in different colors are: KJ2007 for Kang and Jones (2007), KR2013 for Kang and Ryu (2013), EN+2007 for Ensslin et al. (2007) (including two different gas temperatures) and KR 2013+CS 2014 for an "hybrid model" derived by combining the results of Kang and Ryu (2013) and Caprioli and Spitkovsky (2014), as in Vazza et al. (2016). From Bykov et al. (2019)

1.5 Active Galactic Nuclei

Active Galactic Nuclei have been suggested to be the sources of both high-energy neutrinos and Ultra High Energy Cosmic Rays. Their contribution to the γ-ray and neutrino background will be assessed by my study, I provide in the following a brief overview on their structure and classification.

Active Galactic Nuclei are galaxies with an accreting Supermassive Black Hole ($M_{BH} = 10^6 - 10^9 M_\odot$) at their centre. While all galaxies host a supermassive black hole at their centre, only 1-10% of them are active. AGN are able to produce very high luminosities ($L_{bol} \sim 10^{40} - 10^{48}$ erg/s) concentrated in small regions (of the order of a few milliparsecs, in most cases) surrounding the black hole. Their emission covers the whole electromagnetic spectrum as visible from Figure 20 (Padovani et al., 2017). The ultimate source of such luminosity is the gravitational potential energy of the black hole (Urry and Padovani, 1995).

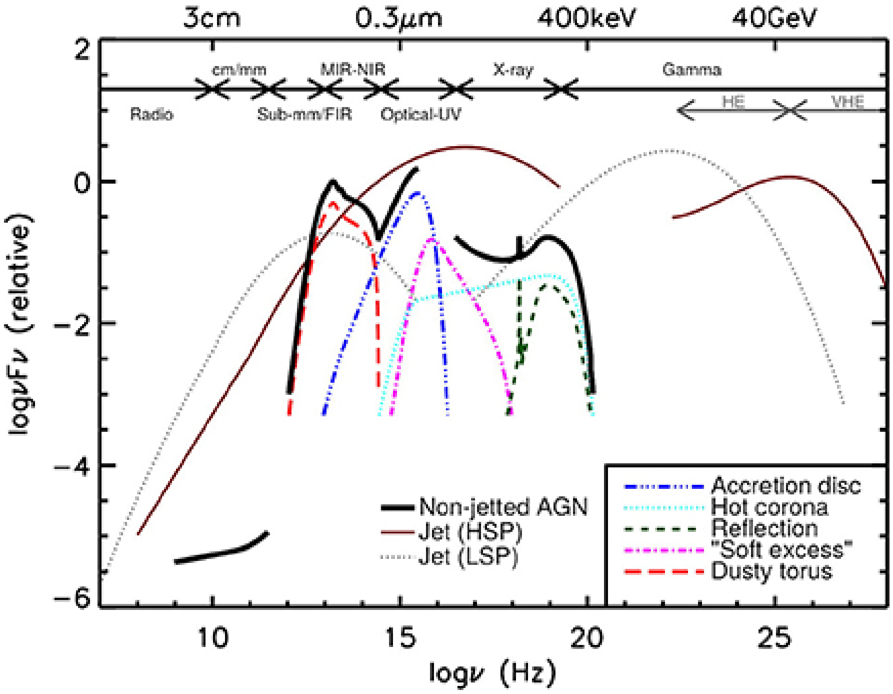

Figure 20: A template of the multi-wavelength emission of AGN: *in red* the emission from the dusty torus, *in blue* the optical emission form the accretion disk, *in pink* the soft X-ray emission probably due to the Comptonization of the disc, *in light blue* the power-law emission from the hot corona, *in green* the emission of photons produced in the corona and reflected by the disc, *in black* the total emission form a non-jetted AGN, while *in brown* and *in grey* the emission from two different models for jetted AGN. From Padovani (2017)

A schematic depiction of the AGN structure is shown in Figure 21: the matter falling onto the black hole settles in an accretion disc where it loses angular momentum through viscous or turbulent motion. The loss of angular momentum is associated with the heating ($T > 10^4 K$) of the accretion disc through friction resulting in the emission of light at wavelengths ranging between the soft X-rays and the optical. The gas located closer to the black hole emits higher energy radiation with respect to the gas located further out (Urry and Padovani, 1995).
In the vicinity of the black hole, the interaction between the photons produced in the disc and the high energy electrons present in the corona results in the emission of hard X-ray photons (Longair, 2011).
When the gravitational force exerted by the black hole is lower than the vertical pressure and the disc fragments into rapidly moving clouds. These clouds produce broad emission lines in the optical and ultraviolet and this is the reason why this region is called Broad Line Region. Moving away from the black hole, the temperature of the gas progressively lowers, at about 0.3-3 pc the gas temperature is low enough for dust to form. The main role played by dust is the reprocessing of light: dust absorbs preferentially ultraviolet and blue light and re-emits it at mid-infrared wavelengths. This region is known as the torus because of its toroidal shape. Beyond the torus (at about 90-900 pc), clouds moving more slowly produce narrow emission lines (Urry and Padovani, 1995).

Outflows of energetic particles can take place along the disk's poles forming radio-emitting jets where particles stream at extremely high velocity and where acceleration of relativistic particles can happen (Urry and Padovani, 1995).

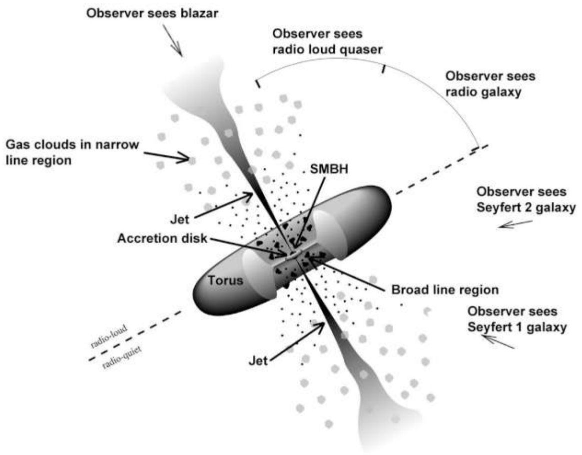

Figure 21: The figure describes the structure of an AGN. From Padovani et al. (2017)

Due to its complex structure, the orientation of an AGN with respect to the line of sight determines which of its components dominates the emission. This results in the fact that AGN have different spectral properties, mostly determined by their orientation. Other factors playing an important role in shaping the spectral properties of an AGN are the presence of strong jets and the host galaxy's environment (Padovani et al., 2017). The different spectral properties of AGN give rise to a complex taxonomy. Here I will give only an overview for the better understanding of my work, for a more exhaustive treatment refer to Longair (2011).

The first classification can be based on the presence of non-thermal radio emission: AGN whose multi-band emission is dominated by thermal processes are known as radio-quiet, while AGN whose emission is dominated by non-thermal processes related to the presence of a jet, are radio-loud. Radio quiet galaxies are further divided into quasars and Seyferts on the basis of their absolute magnitude in the B filter. Quasars are the most luminous of the two having $M_B < -23$, they appear to have very blue colours and they are typically hosted by elliptical galaxies while Seyferts are characterised by $M_B > -23$. Among the latter it is possible to distinguish between Type 1 and Type 2 Seyfert galaxies on the basis of their spectra. An example of spectra of Type 1 Seyfert galaxies is shown in Figure 22: it is characterised by the presence of broad (FWHM $\sim$ 1500-15000 km/s) permitted emission lines and by the presence of narrow (FWHM $\sim$ 500-1500 km/s) forbidden lines ranging between the UV and the optical wavelengths. The spectrum of a Type 2 Seyfert galaxy is shown in Figure 23, it is characterised by the presence of narrow permitted and forbidden lines. The difference in their spectra is explained by the orientation of the AGN with respect to the line of sight: observing and AGN in the equatorial plane means we are observing the torus hence it appears obscured showing a Seyfert 2 spectrum, while observing an AGN on the polar axis, it appears unobscured and shows a Seyfert 1 spectrum. The dust present in the torus absorbs the UV and blue light, causing the narrowing of permitted lines in the spectrum.

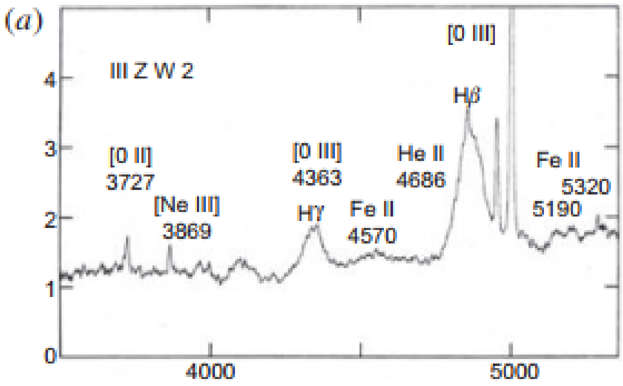

Figure 22: The figure shows the spectrum of the Seyfert 1 galaxy III Zw 2. It is possible to notice the broad emission lines of hydrogen Hγ and Hβ as well as the narrow forbidden lines of oxygen and neon. From Longair (2011)

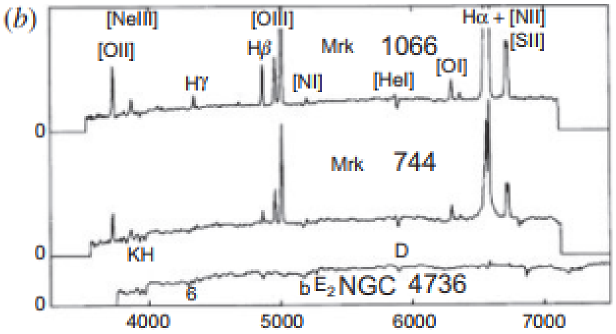

Figure 23: The figure shows the spectrum of the galaxis Mkn 1066 (Type 2) and Mkn 744 (Type 1.8) compared with that of the galaxy NGC 4736.The permitted emission lines (such as Hγ and Hβ) are much narrower than in the case of the Seyfert 1 galaxy and have the same linewidths as the forbidden lines. From Longair (2011)

Radio-loud AGN can be divided into radio-galaxies and blazars on the basis of the jet's orientation and optical spectrum. The emission from blazars is dominated by the non thermal component, since their jet is pointing directly towards the observer. On the basis of their radio spectra, blazars can be divided into Flat Spectrum Radio Quasar (FSRQ) and BL-Lacs. Both Flat Spectrum Radio Quasars and BL-Lacs are variable sources characterised by a flat radio spectra with constant intensity $I_\nu \propto \nu^0$, resulting from the emission of self-absorbed synchrotron radiation in compact sources. However, their optical spectra differ: the ones of FSRQ show broad emission lines while the ones of BL-Lacs are characterised by an almost featureless continuum. The differences in their spectra seem to be explained by a different efficiency in the accretion flow. FSRQ accrete efficiently via an accretion disc and are able to ionise the BLR clouds responsible for the broad line features visible in their spectra. BL-Lacs, on the other hand, are believed to accrete mostly through less efficient advection flows, they have less

ionising power hence the lack of emission lines.
The Spectral Energy Distribution of different classes of blazars is shown in Figure 4. It is characterised by a double peak, the first peak is located between the infrared and the X-ray and is due to synchrotron emission, the second peak ranges between the MeV and the TeV and is generally attributed to Inverse Compton and/or Synchrotron Self Compton. The sequence of SEDs displayed in Figure 4 and it is set by the properties of the accretion flow. FSRQ occupy the high power portion of the diagram, their secondary peak is located at MeV energies and has a power about 10 times higher with respect to the primary one. BL-Lacs, instead, occupy the low power portion of the diagram, their secondary peak is located in the TeV and the primary and secondary peak have the same luminosity. The fact that the secondary peak for FSRQ is at lower energy with respect to BL-Lacs depends on their higher cooling efficiency. The difference in the Compton dominance, instead, is determined by a different origin for the target photons. In FSRQ the secondary peak is due to the scattering of external photons originating in the disc with the high energy electrons present in the jet. For BL-Lacs, the secondary peak is due to Inverse Compton scattering on the photons produced via synchrotron radiation inside the jet. In summary, the complexity of processes involved in the physiscs of AGN, the multi-scale interaction with the environment and the variety of their high energy emission makes them very suitable candidates for the production of high energy neutrinos in the Universe.

2 Methods

2.1 Cosmological simulations: ENZO

Cosmological simulations are employed to study complex astrophysical problems that require solving and following highly non-linear dynamics such as structure formation where smaller objects first collapse and the merge into larger structures. The fundamental constituents of a cosmological simulation are: dark matter, dark energy and ordinary matter together with a set of well-defined initial conditions.

Various observational data such as measurement of the cosmic microwave background or the redshift-distance relation derived from type Ia supernovae constrain the cosmological framework within which cosmological simulations are performed. This framework is known as ΛCDM and according to it our Universe at z=0 is characterised by a flat geometry and dominated by dark matter and dark energy which make up for 95% of its energy density.Its name derives from the fact that Dark matter is believed to be cold and collisionless while the contribution from dark energy is parameterised by the cosmological constant Λ. In this model only 5% of the Universe's energy density can be ascribed to the contribution of ordinary matter.

The initial conditions for a cosmological simulation specify the shape and amplitude of the primordial power spectrum of density fluctuations. Its shape is usually in the form $P(k) = Ak^n|T(k)|^2$ where $T(k)$ is a transfer function, k is the amplitude of the modes, A is a normalisation factor and $n \sim 1$ is the exponent. This spectrum, once subjected to gravity, determines the number of dark matter halos with given mass collapsed within a given time and how quickly these grow through merging (Somerville and Davé, 2014). Once the form of the primordial power spectrum is specified, dark matter positions and velocities as well as baryon density, velocity and temperature field have to be specified. Their form is as follows:

$$\begin{cases} x = q + D(t)\Psi(q) \\ a(t)\dot{x} = a(t)\frac{dD(t)}{dt}\Psi(q) = a(t)H(t)\frac{d\ln D}{d\ln a}D(t)\Psi(q) \end{cases} \tag{12}$$

where x represents the initial positions, q is the unperturbed particle position, $D(t)$ is the linear growth factor, $a(t)$ is the scale factor while Ψ is the displacement field.

Dark matter is modelled by the coupling of the collisionless Boltzmann equation and the Poisson equation:

$$\begin{cases} \frac{df}{dt} = \frac{\partial f}{\partial t} + v\frac{\partial f}{\partial r} - \frac{\partial \Phi}{\partial r}\frac{\partial f}{\partial v} = 0 \\ \nabla^2\Phi = 4\pi G\int f dv \end{cases} \tag{13}$$

where f is the distribution function for dark matter, v represents the velocity and Φ represents the collective gravitational potential. The Boltzmann equation describes the conservation of the dark matter distribution function while the Poisson's equation describes the shape of the gravitational potential. These equations have to be solved in an expanding background Universe. The numerical technique employed by ENZO code to solve the equations is known as particle mesh. The solution for the Poisson's equation is obtained through a convolution between the density field $\rho(x)$ and a Green function $g(x)$ and takes the following form:

$$\Phi(x) = \int g(x - x')\rho(x)dx' \tag{14}$$

The process is typically divided into three steps. At first, a density field from the particle positions on a mesh. The second step involves the transformation of the density field to Fourier's space and the determination of the gravitational potential. The gravitational potential is usually computed in the

Fourier space because the convolution becomes simply:

$$\widehat{\Phi}(k) = \widehat{g}(k - k') \cdot \widehat{\rho}(k) \tag{15}$$

The third step involves the transformation of the gravitational potential back to real space.

Baryonic matter is a subdominant contributor to the Universe's energy density however, it is the Universe's only visible component. This means that simulating baryons is fundamental in order to make predictions. Baryons are mainly composed of hydrogen in the gaseous form. They are usually treated as a magnetized inviscid plasma and describe by the four Euler's equations. The ENZO code is based on the Eulerian formalism of these equations. In this framework the focus is put on specific locations in the fluid through which particles flow. The first equation states the conservation of mass while the last one states the conservation of the total energy per unit mass. The set of equations is expressed as:

$$\begin{cases} \frac{\partial \rho}{\partial t} + \nabla \cdot (\rho v) = 0 \\ \frac{\partial \rho v}{\partial t} + \nabla \cdot (\rho v \otimes v + P) = 0 \\ \frac{\partial \rho e}{\partial t} + \nabla \cdot (\rho e + P) v = 0 \end{cases} \tag{16}$$

where ρ is the density, t is time, v is the velocity, P is the fluid's pressure and e is the total energy per unit mass (Vogelsberger et al., 2019).

This structure constitutes the basis for a cosmological simulation. Usually it is complemented by the other astrophysical processes relevant in shaping galaxy populations such as: gas cooling, magnetic fields, stellar feedback, AGN feedback, radiative transport and cosmic rays. Among these processes the most peculiar ones are feedback processes and cosmic rays.

Feedback processes retard the star formation either by preventing the collapse of gas or by removing the gas, they are usually taken into account by subgrid recipes. Feedback can be driven by stars that deposit large amounts of energy in the interstellar medium. This type of feedback is believed to explain the inefficiency in the conversion of gas into stars in giant molecular clouds and the low fraction of stars with respect to the baryon content of galaxies.

The other drivers for feedback processes are Active Galactic Nuclei that can heat up, eject, ionize or photo-dissociate gas through photo-ionization, photo-electric heating and winds(Somerville and Davé, 2014).

2.2 ENZO MHD runs used for this Thesis

I used a set of newly produced cosmological magneto-hydrodynamical simulations using ENZO [1], designed to investigate the injection and evolution of cosmic rays by different mechanisms operating in the cosmic web.

In detail, the simulations covered a comoving volume of $(42.5 \text{ Mpc})^3$ with a static grid of 1024^3 cells, giving a constant spatial resolution of 41.5 kpc/cell and a constant mass resolution of 1.01×10^7 $\text{M}_\odot$ per dark matter particle. All runs include equilibrium gas cooling, a "sub-grid" dynamo amplification model at run-time, which allows the estimation of the maximum contribution of a dynamo in low density environments (see e.g. Vazza et al., 2017), while the treatment of primordial magnetic fields and feedback from galaxy formation processes varies.

---

[1] enzo-project.org

I analysed two models in which magnetic fields and cosmic rays were injected at run-time in the simulation, both by star forming particles and by simulated active galactic nuclei. The star formation recipe follows the method by Kravtsov (2003), designed to reproduce the observed Kennicutt's law (Kennicutt, 1998) and with free parameters calibrated to reasonably reproduce the integrated star formation history and the stellar mass function of galaxies at $z \leq 2$. The feedback from star forming particles assumes a fixed fraction of energy/momentum/mass ejected per each formed star particles, $E_{SN} = \epsilon_{SF} m_* c^2$, with efficiency calibrated to $\epsilon_{SF} = 10^{-8}$ as in previous work (Vazza et al., 2017). The simulation also considers that 90% of the feedback energy is released in the thermal form (i.e. hot supernovae-driven winds), distributed the 27 nearest cells around the star particle, and 10% in the form of magnetic energy, assigned to magnetic dipoles by each feedback burst.

The feedback from active galactic nuclei is treated by assuming that, at each timestep of the simulation, the highest density peaks in the simulation harbour a supermassive black hole, to which we assign a realistic mass based on observed scaling relation (e.g. Gaspari et al., 2019). We then compute the instantaneous mass growth rate onto each supermassive black hole by following the standard Bondi–Hoyle formalism, in which we include (as typically for simulations at this resolution) an ad-hoc "boost" parameter meant to compensate for the lack of resolution around the Bondi radius. Depending on the temperature of the accreted gas, we use either "cold gas accretion" feedback (in which most of the energy is distributed in the form of thermal energy in the neighbourhood of each simulated AGN) or "hot gas accretion" feedback (in which most of the energy is released in the form of bipolar kinetic jets). In both cases, 10% of the feedback energy is released in the form of magnetic energy, through pairs of magnetised loops wrapped around the direction of kinetic jets. This magnetic field is added to a negligible uniform initial seed field of $B_0 = 10^{-11}$ nG (comoving), leading to "magnetic bubbles" correlated with halos in the simulated volume. The two variations studied in this work concerns two different set of parameters for the efficiency of feedback from the hot and cold gas accretion and are calibrated to well reproduce the radio luminosity functions of real radio galaxies in the local Universe. A more detailed descriptions of all parameters used in this model will be given in a forthcoming paper (Vazza et al., in prep).

2.2.1 Simulated sources of cosmic rays

The simulation in use separately tracks three different populations of cosmic rays: the one arising from shocks, the one arising from galaxies and the one arising from AGNs.

Shocks: The run-time modelling of cosmic ray injection from shocks requires the identification of such shock waves. Their detection is based on the difference between the gas pressure in neighbouring cells. Candidate shocked cells are selected by requiring a converging gas flow in the cell, which translates to $\nabla \cdot \mathbf{v} < 0$. The cells neighbouring a candidate shock are analysed to check whether the gas temperature and entropy are producing irreversible heating by changing in the same direction $\nabla S \cdot \nabla T > 0$. The verse for the shock propagation is determined by the temperature gradient. Once the pre and post-shock cells are set, the Mach number of the shock can be computed by means of the pressure jump in the pre and post-shock regions: $\frac{P_2}{P_1} = \frac{2\gamma M^2 - \gamma + 1}{\gamma + 1}$, where P_2 is the pressure in the post-shock region, P_1 is the pressure in the post-shock region and γ is the adiabatic index. Only supercritical shocks with $M \geq 2$ inject cosmic rays in the simulation. In order for cosmic rays to participate in the DSA process and diffuse across the shock, their momentum has to be greater than the injection momentum $p_{inj} = Q_p p_{th}$ where $p_{th} = \sqrt{2 m_p k_B T_p}$ and $Q_p = 3.5 - 3.8$. If we assume a thermal leakage model, the distribution function of the accelerated CR protons is approximately:

$$f(p) = \frac{n_d}{\pi^{3/2}} p_{th}^{-3} \exp\left(-\xi_{inj}^2\right) \exp\left(-\frac{p^2}{p_{max}^2}\right) \tag{17}$$

Here p_{max} is the maximum momentum reached by DSA accelerated particles while ξ represents the fraction between the post shock thermal particle density (n_2) and the number density of accelerated cosmic ray protons (n_{CR}).

Under these hypothesis, the fraction between the post-shock thermal particle density (n_2) and the number density of accelerated CR protons ($n_{\rm CR}$) is given by Kang (2020) and Kang (2021):

$$\xi_{\rm shocks}(\mathcal{M}) = n_{\rm CR}/n_2 = \frac{4x_{\rm inj}^3}{\pi^{3/2}(\alpha_{\rm inj} - 3)} \exp\left(-x_{\rm inj}^2\right). \tag{18}$$

We set $x_{\rm inj} = 3.5$ and $\alpha_{\rm inj} = 4\mathcal{M}^2/(\mathcal{M}^2 - 1)$. The trend of the acceleration efficiency, in terms of the fraction of CRs accelerated with respect to the number of thermal protons in the upstream and as a function of the shock Mach number is given in Fig.24.

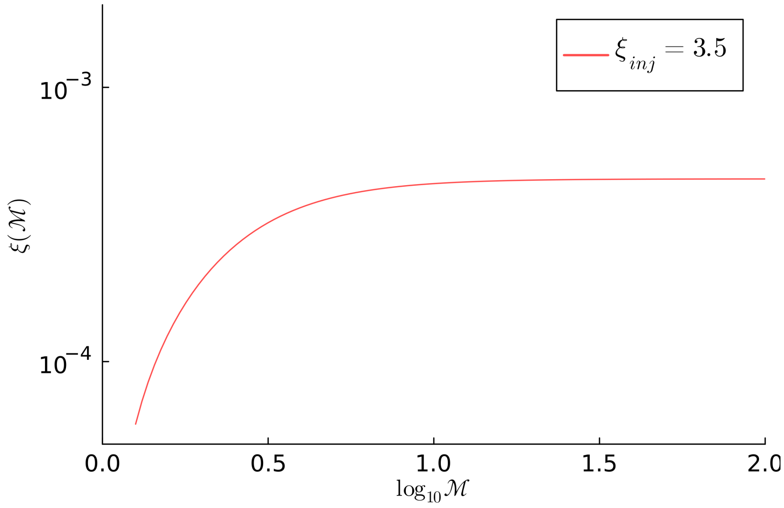

Figure 24: The Figure shows the shock acceleration efficency of CR protons as a function of Mach number, in the ENZO simulations analysed in this Thesis.

Star formation

New CRs are injected into the same cells, using a fixed fraction $\xi_{\rm SN,CR} = n_{\rm CR}/n_g$ of the local gas density, n_g. The value of this fixed fraction depends on several processes, all severely under-resolved given the temporal and spatial resolution of our fixed grid runs: a) the direct injection of CRs from DSA by shocks driven by supernova remnants and pulsar wind nebulae and b) the continuous injection of secondary CRs from the hadronic collisions between thermal protons and CR protons injected via DSA by the same aforementioned mechanisms, which in turn release a cascade of particles as in the hadronic cascade model; c) the thermalisation of CRs due to collisional and ionisation losses, which are particularly strong in the dense interstellar medium (e.g. Pfrommer et al., 2017). With a series of tests, we calibrated the total amount of CR electrons and CR protons injected by star formation requesting that the synchrotron radio emission from the actively star forming galaxies in our runs match the typical distribution of radio emission by real galaxies.

The reference value adopted in the simulations used in this Thesis is $\xi_{\rm SN,CR} = 10^{-5}$.

Active Galactic Nuclei

We injected new CRs within the jets, with density equal to a fixed fraction of the number density of the thermal gas in jets, $n_{\rm CR,jet} = \xi_{\rm Jet,CR} n_{\rm jet}$.

The amount of cosmic rays carried by jets is highly uncertain, and is possibly different across cosmic environments (i.e. in clusters or in the field), as suggested by the dynamical modelling of radio galaxies (e.g. Croston et al., 2018).

The starting reference value adopted in the simulations used in this Thesis is $\xi_{\rm Jet,CR} = 0.01$. However, as discussed in the conclusion of my Thesis, this value likely has to be renormalised (i.e. by a factor ~ 6 low) based on the findings I will discuss in the next section.

Figure 25 shows the relation between the hadronic γ-ray emission and the synchrotron radio emission produced, using our baseline efficiency parameters for AGN jets and star formation, for all galaxies in the simulation at four different redshifts. Within the significant scatter of data, the simulated emissions are in line with the best fit of real observations of local galaxies, obtained by Ajello et al. (2020) using FERMI and NVSS, which suggests that our baseline theoretical model is realistic.

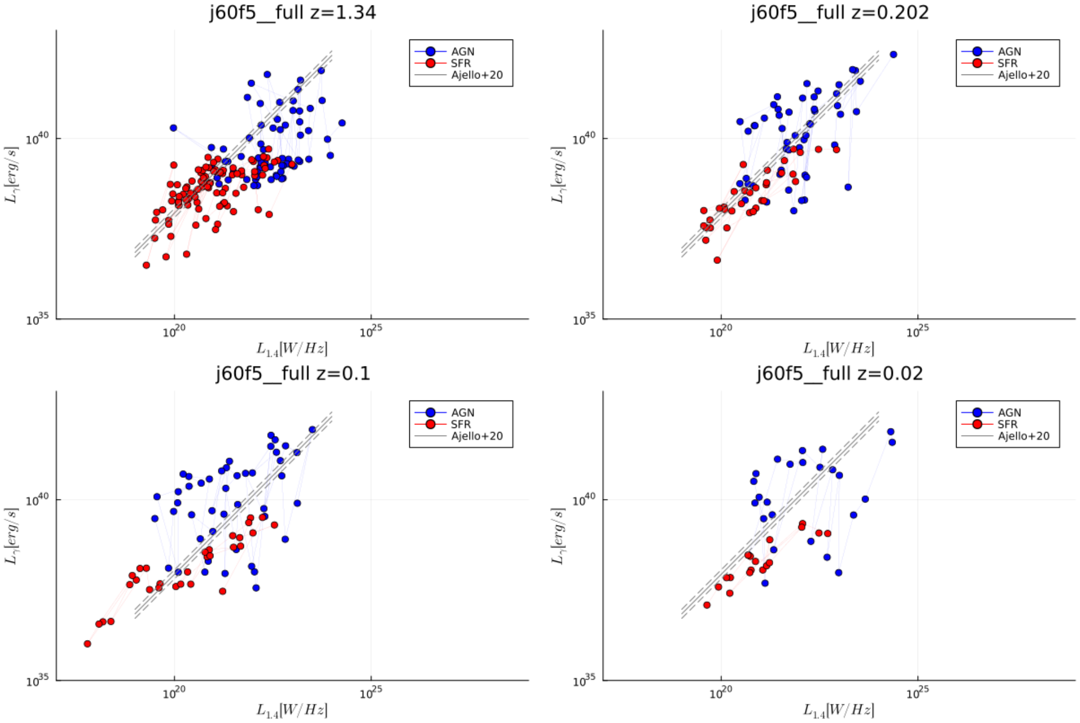

Figure 25: The Figure shows the relation between the hadronic γ-ray emission and the synchrotron radio emission from all galaxies in the simulation considered in this Thesis, at four different redshifts and compared to a collection of real observations, taken from Ajello et al. (2020).

Propagation of Cosmic Rays The simulation assumes that CR protons have a negligible dynamical impact on the gas dynamics, and this makes it possible to treat their propagation through the simulations assuming they are a passively advected fluid. This means that, after their injetion by multiple sources, CR are advection over time, neglecting any dynamical feedback on the thermal gas fluid, and using the same magneto-hydrodynamical routines in ENZO solvers, to advect all other fluid quantities in the simulated volume. CRs are tracked separately for each species, meaning that the code tracks the number density of CRs (i.e. not the energy density, as done in other approaches) because this allows us to use exactly the same advection routine and enforce the same mass conservation of all other fluid species tracked in ENZO.

This approach does not explicitly model the additional process of CR diffusion, but only CR transport assuming that CRs are frozen-in the gas.

This assumption is valid for the lowest energy CR protons responsible for production of γ-ray emission simulated in my Thesis, while diffusion cannot be entirely neglected for he highest energy CR protons which are responsible for the production of neutrinos observed by IceCube.

Predicting the diffusion of CRs in a tangled magnetic field is a non trivial problem in astrophysics (e.g. Bhattacharjee, 2000; Lazarian et al., 2023; Harari et al., 2014, for reviews),

In order to guess the diffusion coefficient of the high energy ($\geq 10^7 - 10^8$ GeV) CR protons responsible for the injection of neutrinos detected by IceCube, we can refer to the spatial diffusion coefficient derived by Harari et al. (2014) to fit the numerical propagation of high energy CRs in the $10^{15} - 10^{20}$ eV range.

Considering that $l_{\rm diff} \approx \sqrt{4D\tau}$, for a low $B = 0.01\mu G$ field, the diffusion coefficient is $D \sim 9 \cdot 10^{31}$erg/s, leading to a diffusion length of $l_{\rm diff} \sim 90$ kpc in a $\tau = 1$ Gyr timescale, which is of the same order of two cells in our simulations. For lower energies or higher magnetic field values (which are more realistic considering that most of our CRs are sourced by the highly magnetised regions of AGN or star forming regions), the diffusion length scale is smaller than this, indicating that the effect of CR diffusion can be reasonably neglected compared to the one of advection, for the sake of my analysis.

2.3 Age determination of the CR distributions

In order to assess the typical age of the CRe present in any given cell of the simulation at any time, recipe based on Beckmann et al. (2019) was implemented in the the ENZO simulation, which can also track the propagation of a second "decaying" CRe fluid for each of the primary CRe species, which gets injected and advected exactly as the primary CRe species. However, it is additionally subject to an exponential decay with a fixed, arbitrary timescale (τ, so that $n'_{CRe} \propto e^{-t/\tau}$): $n'_{CRe}(t + \Delta t) = n'_{CRe}(1 - \Delta t/\tau)$. This makes it possible, at any stage in the simulation, to infer the time elapsed since the last injection of dominating the budget of CRe in all cells:

$$t_{\rm age} = -\tau \log\big(\frac{n'_{\rm CRe}(t)}{n_{CRe}(t)}\big), \tag{19}$$

in which n_{CRe} is the number density for each of the primary CRs (i.e. not subjected to the artificial decay law). No other dynamical exchange between CRs and the thermal gas is assumed to take place (e.g. Coulomb losses).

2.4 Theoretical modelling for proton proton interactions

The modelling of gamma ray and neutrino spectra arising from proton proton interactions are calculated by a Julia program (https://julialang.org/) through the formalism outlined by Pfrommer and Ensslin

(2004). This allows us to describe the decay of secondary neutral pions into two high-energy gamma rays through the introduction of opportune source functions.
We define the the differential source function and the emissivity respectively as:

$$\begin{cases} q(r,E) = \frac{dN}{dtdVdE} \\ j(r,E) = Eq(r,E) \end{cases} \tag{20}$$

Where N is the integrated number of particles, t represents the time, V represents the volume and E represents the energy. Their volume integrated quantities are defined as:

$$\begin{cases} Q(E) = \int dV q(r,E) \\ J(E) = EQ(E) \end{cases} \tag{21}$$

Cosmic ray protons are assumed to have everywhere a power-law spectrum with the very flat slope of $\alpha_p = 2.05$, typical of the strong shocks which are predicted to form in cosmic structures (Bykov et al., 2019). This means that we assume no losses of energy for our cosmic ray protons entering the simulation. This is a fair enough approximation considering that the cooling timescales for ionisation and Coulomb losses even at the highest densities in our simulation are long. For example for $E = 1$ GeV protons in a $10^{-3}cm^{-3}$ medium the loss timescale is $\sim$ 30 Gyrs, and it is 3 Gyrs for $E = 100$ GeV. As shown in Section 3.1, the average time elapsed since the last injection of cosmic rays is $\leq$ 2 Gyrs at $z = 0$ in our simulations (or even less at high redshift) showing that neglecting cosmic ray losses is a fair enough assumption of the effects of cosmic rays considered in my Thesis.
Cosmic ray protons whose momentum is above the kinematic threshold $p_{tr} = 0.78 GeV c^{-1}$ can produce pions through hadronic mechanism when interacting with the thermal gas background. According to isospin symmetry if we assume the thermal equilibrium of the pion cloud in the centre of mass, the pions have relative multiplicities of $\xi_{\pi^0} = \frac{1}{2}\xi_{\pi^\pm}$. The charged pions decay into secondary muons, electrons and neutrinos, while neutral pions decay into two gamma rays as shown in Equation 1. In the high energy limit, cosmic ray protons possess energies $E_p \gg m_p c^2$ and the pion source function can be approximated to:

$$q_{\pi^0}(\mathbf{r}; E_{\pi^0}) dE_{\pi^0} dV \sim 2^3 \overline{\sigma}_{pp} c n_N(\mathbf{r}) \frac{\tilde{n}_{CRp}(\mathbf{r})}{GeV} \times \left(\frac{6E_{\pi^0}}{GeV}\right)^{-\alpha_\gamma} dE_{\pi^0} dV \tag{22}$$

Here $\overline{\sigma}_{pp} = 32$ mbarn is the inelastic cross-section for proton proton collisions, $\alpha_\gamma = 4/3(\alpha_p - 1/2)$ and $n_N = d_{tar} n_e(\mathbf{r}) = n_e(\mathbf{r})/(1 - 1/2X_{He})$ is the target nucleon density (which can be computed in the simulation based on the gas density).
The differential source function integrated over the solid angle for the gamma rays produced by the decay of neutral pions can be calculated in the same energy regime by assuming an isotropic distribution of the decay products in their rest frame. It can be expressed as:

$$q_\gamma(\mathbf{r}; E_\gamma) = 2 \int_{E_\gamma + \frac{m_\pi^2 c^4}{4E_\gamma}}^{\infty} dE_{\pi^0} \frac{q_\pi^0(\mathbf{r}; E_{\pi^0})}{\sqrt{E_{\pi^0}^2 - m_{\pi^0}^2 c^4}} = 2^3 \overline{\sigma}_{pp} c n_N(\mathbf{r}) \frac{\tilde{n}_{CRp}(\mathbf{r})}{GeV} \times \left(\frac{6 m_{\pi^0} c^2}{GeV}\right)^{-\alpha_\gamma} \mathcal{B}_x\left(\frac{\alpha_\gamma}{2}; \frac{1}{2}\right) \tag{23}$$

where $\mathcal{B}_x(a;b)$ represents the incomplete beta-function with $x = \left(\frac{4E_\gamma m_{\pi^0} c^2}{4E_\gamma^2 + m_{\pi^0}^2 c^4}\right)^2$. The formula shown in Eqn 23 is valid both in the $E_\gamma \ll m_{\pi^0} c^2/2$ regime and in the $E_\gamma \gg m_{\pi^0} c^2/2$ regime. However, it overestimates the number of gamma rays for energies $E_\gamma \sim m_{\pi^0} c^2/2$. Pfrommer and Ensslin (2004) derived an analytic formula meant to include more detailed physics at the pion production threshold through the use of the shape parameter $\delta_\gamma = 0.14\alpha_\gamma^{-1.6} + 0.44$ and the expansion of the beta function present in Eq.23. We will present here the revised expression present in Beckmann et al. (2022):

$$q_\gamma(\mathbf{r}; E_\gamma)dE_\gamma dV \simeq \overline{\sigma}_{pp} c n_N(\mathbf{r})\tilde{n}_{CRp}(\mathbf{r}) \times \left(\frac{2^{4-\alpha_\gamma}}{3\alpha_\gamma}\right)\left(\frac{m_{\pi^0}c^2}{GeV}\right)^{-\alpha_\gamma}\left[\left(\frac{2E_\gamma c^2}{m_{\pi^0}c^2}\right)^{\delta_\gamma} + \left(\frac{2E_\gamma c^2}{m_{\pi^0}c^2}\right)^{-\delta_\gamma}\right]^{-\alpha_\gamma/\delta_\gamma} \tag{24}$$

Here $\overline{\sigma}_{pp} = 10^{-27}\left[1 - \left(\frac{1.22}{E_p}\right)^4\right]^2 (34.3 + 1.88L + 0.25L^2)$ is the effective inelastic cross section as presented in Kelner et al. (2006) and $L = \ln(E_p/1TeV)$.
The expected gamma ray flux is then computed by integrating the source function over energy and volume: $F_\gamma = \int q_\gamma(\mathbf{r}; E_\gamma)dE_\gamma dV$. In particular, the source function is integrated over an energy range of $E_\gamma = [0.5, 200]$ GeV in order to compare it with the gamma ray diffuse background detected by Fermi.

The neutrino fluxes can be estimated in a similar fashion by using a neutrino source function q_ν (Ha et al., 2020). Such source function can be related to the γ-ray source function q_γ by assuming that the pion source function q_π has a power-law form $q_\pi(\mathbf{r}; E_\pi) \propto E_\pi^{-\alpha_\gamma}$. The neutrino source function at neutrino energies $E_\nu = E_\gamma$ has the following expression:

$$q_\nu(\mathbf{r}; E_\nu)dE_\nu dV = q_\gamma(\mathbf{r}, E_\gamma)[Z_{\nu_\mu}(\alpha_\gamma) + Z_{\nu_e}(\alpha_\gamma)] \tag{25}$$

The variables $Z_{\nu_\mu}(\alpha_\gamma)$ and $Z_{\nu_e}(\alpha_\gamma)$ are meant to take into account the contribution from muon and neutrino electrons respectively. Their expression is derived in Kelner et al. (2006) as follows:

$$Z_{\nu_\mu}(\alpha_\gamma) = \frac{4[3 - 2k - k^{\alpha_\gamma}(3 - 2k + \alpha_\gamma - k\alpha_\gamma)]}{\alpha_\gamma(1-k)^2(\alpha_\gamma + 2)(\alpha_\gamma + 3)} + (1-k)^{\alpha_\gamma - 1} \tag{26}$$

$$Z_{\nu_e}(\alpha_\gamma) = \frac{24[(1-k)\alpha_\gamma - k(1 - k^{\alpha_\gamma})]}{\alpha_\gamma(1-k)^2(\alpha_\gamma + 1)(\alpha_\gamma + 2)(\alpha_\gamma + 3)} \tag{27}$$

where $k = m_{\mu^\pm}^2/m_{\pi^\pm}^2 = 0.573$. In the Julia program (6), the neutrino fluxes are calculated by integrating the source function in the interval $[10^5; 10^6]$ GeV, which corresponds to the typical energy range for neutrinos detected by IceCube.
Considering the effect of oscillations across extragalactic distances, the neutrino flux computed with the above formalism is considered to be the all-flavour neutrino flux produced by our simulations, to be compared with the all-flavour neutrino fluxes measured by IceCube Collaboration upon extrapolating form their measurement.

The neutrino and gamma ray fluxes are computed by a Julia program which I used for this thesis (6), separately for shocks, AGNs and star formation for every cell in each of the simulations' snapshots. To study their evolution in redshift, the fluxes are summed over all of the cells in the snapshot's volume $\overline{F}_\gamma$ and $\overline{F}_\nu$.

2.5 Cumulative fluxes

The Julia code I developed for the computation of the cumulative fluxes (7) takes as input about 15 time snapshots of the γ-ray and neutrino emission from two different runs. At first it computes the integrated background emission from γ-rays and neutrinos by processing the snapshots from the simulations (the two runs have a slightly different number of saved snapshots), saved in the redshift range between $z \approx 3$ and $z = 0$, with a redshift spacing of about $\Delta z = 0.2$.

I plotted the fluxes arising from each type of sources (shocks, AGNs or star-forming galaxies) against the redshift's evolution, in order to first compute the trend of the emission in the comoving reference frame of each snapshot.

Next, I interpolated the resulting curves with a first order spline through the built-in Julia function `linear_interpolation()` with a step size of 0.05 in redshift. This procedure allowed a finer redshift binning.

The interpolated comoving fluxes were converted into real fluxes, observable by a $z = 0$ observer via:

$$F_{real} = (1+z)^{-\alpha_\gamma+1} \frac{F_{int} V_{com}}{4\pi} \frac{E^2}{4\pi d_L^2} \ [\mathrm{MeV\ cm^{-2} s^{-1} sr^{-1}}] \tag{28}$$

where d_L is the luminosity distance, F_{int} is the interpolated flux, V_{com} is the comoving volume and $(1+z)^{-\alpha_\gamma}$ is a correction factor taking into account the bandwidth compression. Bandwidth compression refers to the fact that the photons emitted over a frequency range $[(1+z)\Delta\nu]$ are squeezed into a frequency $\Delta\nu$ in the observer's frame (Condon and Matthews, 2018). I computed the comoving volume by considering each of the nodes at which the fluxes were computed as the centre of a redshift bin. In this way the comoving volume for the i-th node corresponds to the i-th bin volume and its expression is: $V_{com} = 4\pi d_c^2(i)[d_c(i+1) - d_c(i-1)]$, where d_c represents the comoving distance.

Finally the contribution to the neutrino diffuse flux at every redshift were summed over to obtain a cumulative flux to be compared with the measured background.

3 Results

In order to give a complete overview of the steps undertaken by my Thesis project to predict the level of extragalactic neutrino emission from the entire cosmic web, I will present my results first by introducing a number of sanity checks done on a small test run (Sec. 3.1), followed by the full analysis of two larger production runs with variations of galaxy formation physics (Sec.3.2), which I used to compute the integrated γ-ray and neutrino backgrounds and compare with real data (Sec.3.4).

3.1 Properties of Cosmic Rays across the simulated universe at redshift 0

Since the neutrino and γ-ray emission derive from processes involving cosmic rays, I initially performed an analysis of cosmic rays at a sample redshift of 0 extending over a cubic volume of about 10.5 Mpc per side with a resolution of 20.8 kpc (hence sampled by a 256^3 grid) in order to verify the pipeline.
The high energy protons are divided in the three populations described above: shocks, AGNs and star-formation. To preliminary disentangle the contribution from structure formation shocks and galaxy formation, the contributions from the AGN and star-formation are considered as a single.
The first analysis I performed was meant to understand the morphology of the variables characterising the simulation: gas density, Dark Matter density, gas temperature, magnetic field, cosmic ray density from both cosmic shock injection and feedback and also the distribution of time elapsed since the cosmic ray injection. The analysis has been performed on a 'slice' of area $(10.5)^2 Mpc^2$ and thickness 20.8 kpc.
Figure 26b shows the spatial distribution of Dark Matter which is a quantity tracked by our simulation, as explained in Section 2.1: its distribution is not uniform over the area, instead it shows a concentration in the upper right and in the lower left portions of the area. It is possible to notice the presence of elongated structures in the lower right portion.
Figure 26a shows the spatial distribution of gas density: it follows the distribution of Dark Matter as expected form structure formation theory.

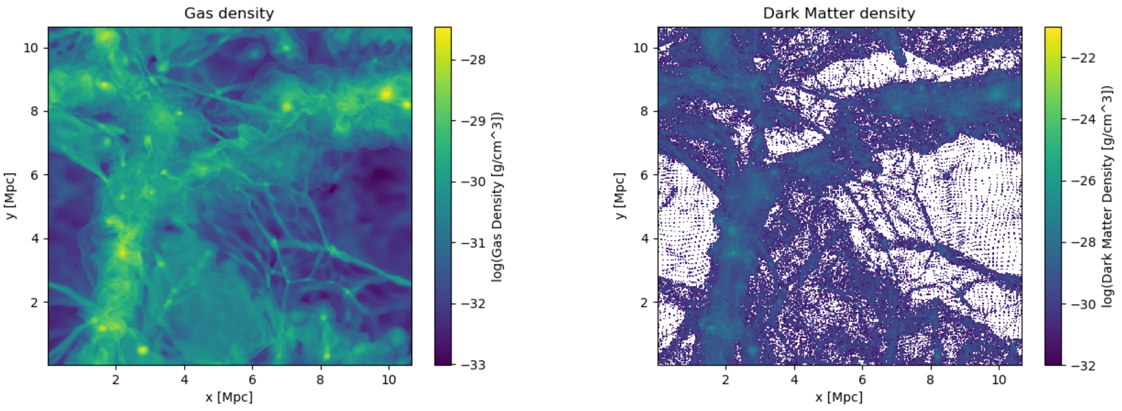

(a) Morphology of the gas density for a thin slice through a test cosmological simulation at $z = 0$.

(b) Morphology of the Dark Matter density for a thin slice through a test cosmological simulation at $z = 0$.

Figure 26

Figure 27a shows the spatial distribution of magnetic fields: they are mostly located in upper and in

the lower-left portion of the volume in correspondence with the highest density regions. This is explained by the fact that in the simulation magnetic fields are injected by AGN and galaxies as expected from structure formation theories.
The spatial distribution of the highest temperature component (T $\sim 10^6$ K, shown in yellow in Figure 27b) is similar to the one of magnetic fields, which is consistent with the fact that gas accreting onto bound structures is heated in the virialisation process. The Figure shows also the presence of a lower energy gas (T $\sim 10^4$ K) forming extended and filamentary structures.

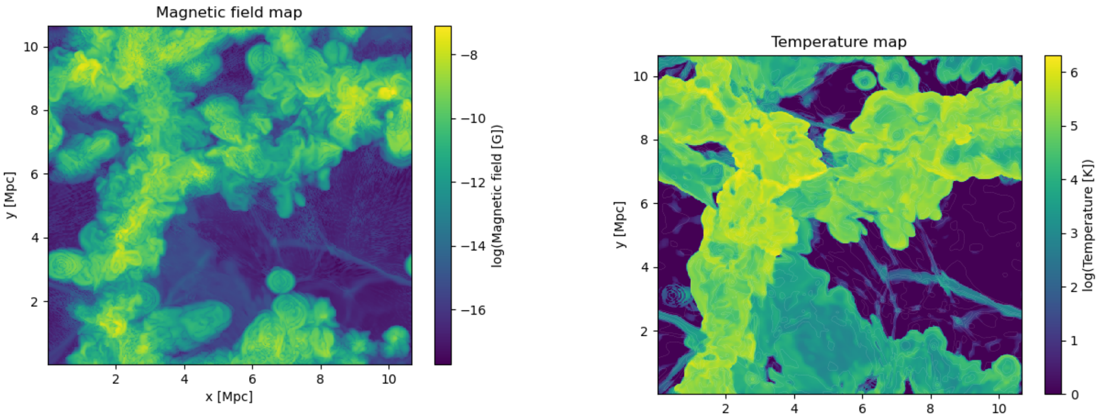

(a) Morphology of the magnetic field amplitude for a thin slice through a test cosmological simulation at $z = 0$.

(b) Morphology of the temperaturefor a thin slice through a test cosmological simulation at $z = 0$.

Figure 27

Figure 28 shows the morphology of the cosmic ray density: it is possible to notice that the spatial distribution of cosmic rays injected by cosmic shocks (subfigure 28a) closely follows the one of the gas temperature, while the spatial distribution of cosmic rays injected by AGN and star formation follows the spatial distribution of magnetic fields.

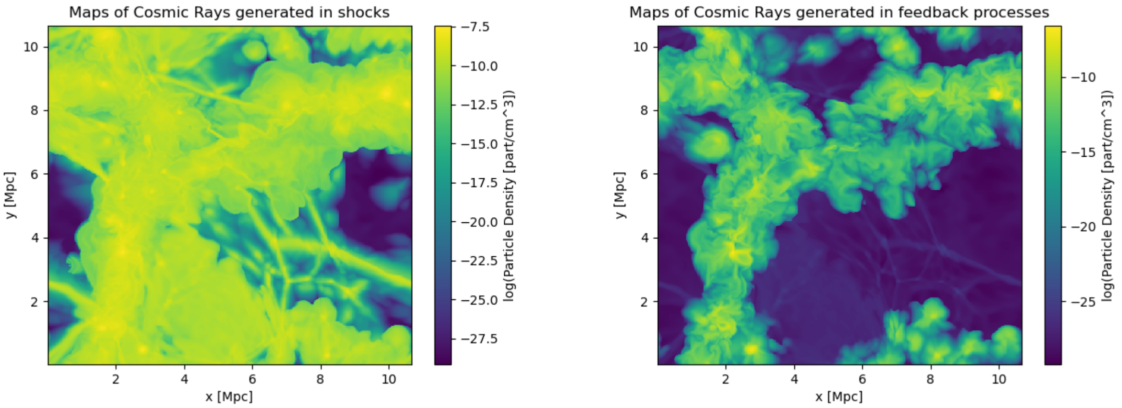
Maps of Cosmic Rays generated in shocks

Maps of Cosmic Rays generated in feedback processes

(a) Morphology of the density of cosmic rays injected by shocks for a thin slice through a test cosmological simulation at $z = 0$.

(b) Morphology of the cosmic rays injected by AGN and star-formation for a thin slice through a test cosmological simulation at $z = 0$.

Figure 28

Figure 29 shows the spatial distribution of time elapsed since the injection of cosmic ray particles, which is an easy measurable quantity tracked by this new suite of simulations, as explained in Sec.2.3. It is possible to notice that cosmic rays injected by shocks have typically been injected less than 3.5 Gyrs ago. On the other hand, cosmic rays inject by AGN and star-formation have typically been injected between 3 and 3.5 Gyrs ago implying that, while AGN and star-formation had a peak activity at high redshift, cosmic shocks are produced at any time in the cosmic web, following the ongoing process of matter accretion driven by gravity at any epoch.

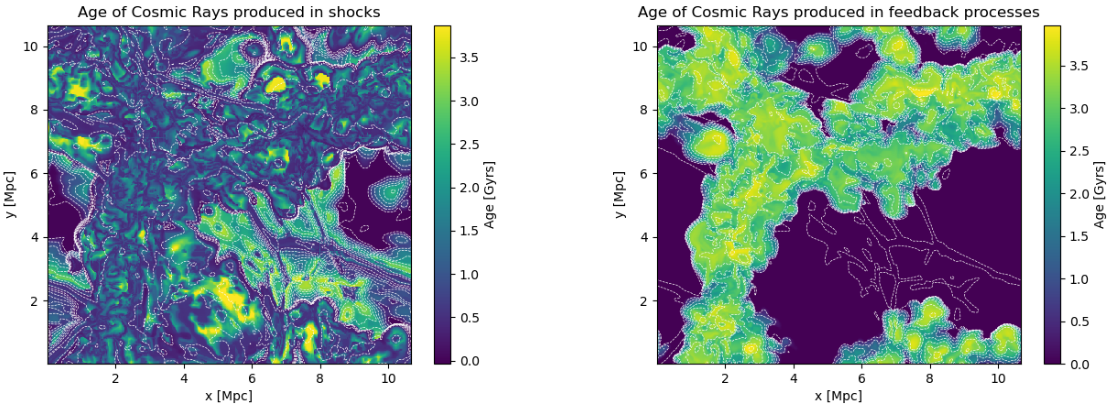

(a) Age distribution for cosmic rays injected by shocks for a thin slice through a test cosmological simulation at $z = 0$.

(b) Age distribution the cosmic rays injected by AGN and star-formation for a thin slice through a test cosmological simulation at $z = 0$.

Figure 29

Next, I analysed the main properties of the two cosmic ray populations, they are summarised in Table 1. Finally, I tried to relate the properties of cosmic rays to the properties of the gas.

	CR shock	CR AGN+SF
Average age per cell [Gyrs]	1.50	2.3
Average energy per cell [erg]	10^{55}	10^{54}
Average density per cell [cm^{-3}]	10^{-16}	10^{-17}

Table 1: Table showing the main properties for the two populations of cosmic rays present in the model at redshift $z = 0$. The quantities are averaged over cubic cells of 20.8 kpc per side. The 'age' of cosmic rays actually refers to the time elapsed since their injection

From the table it is possible to see that, in the model analysed, cosmic rays from AGNs and star-formation are typically older, less dense and less energetic than the ones from shocks. The difference in age is explained by the fact that AGN inject cosmic rays mostly during the peak of their activity which is at $z \sim 2$. Cosmic shocks instead can develop at any time following the conditions of matter accretion onto halos and therefore the cosmic rays are injected even at more recent times.
This paradigm is confirmed by observing the correlations between the age of cosmic rays and their energy. For both categories of cosmic rays it is possible to notice that the oldest cosmic rays are the highest energy ones. These particles are now diffusing through empty cosmic volumes thus preventing them from loosing energy, while those among them diffusing in dense areas of the volume interacted with particles becoming thermalised very quickly.

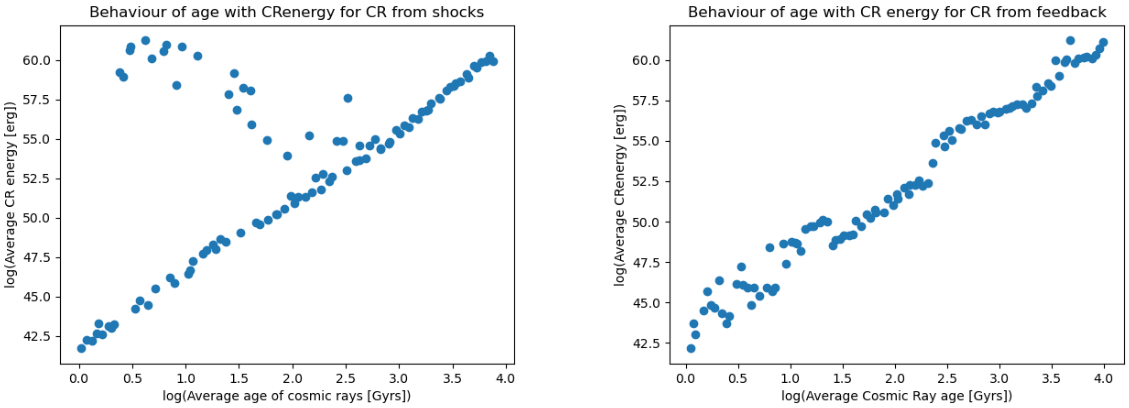

(a) Cosmic rays injected by shocks

(b) Cosmic rays injected by AGNs and star-formation

Figure 30: In the figure the logarithm of the average CR energy is plotted against the average cosmic ray age.

The study of the behaviour of the cosmic ray density versus the ambient gas density highlighted another trend: the normalised density of cosmic rays injected by shocks is found to be constant at the value of 10−3 for ambient gas densities comprised between 10^{-31} and 10^{-27} g cm^{-3} as can be visualised in Figure 31a. Such a feature shows that shocks are present both in cosmic filaments and in bound structures, and that the mechanisms responsible for the injection of cosmic rays from shocks do not vary significantly in the two environments.

For the high energy particles injected by AGN and star-formation, instead, the relation between their normalised density and the ambient gas' density is showed in Figure 31b. It is characterised by two distinct concentrations of values. At gas densities between 10^{-34} and 10^{-28} g cm^{-3} the cosmic rays show a wide range of normalised densities ranging from $10^{-7.5}$ to 10^{-20}. On the other hand for gas densities above 10^{-28} g cm^{-3}, the normalised values seem to be clustered in a narrower region with higher values ranging between 10^{-5} and $10^{-2.5}$. The two groups of values are representative of the two distinct environments in the simulation where we can find particles injected by AGN and star formation: galaxies (for the particles with energies above 10^{-28} g cm^{-3}) and cosmic filaments. The galactic cosmic ray population shows a higher value of the normalised density because such particles are produced in the innermost regions of galaxies and might be the result of recent galactic activity.

In essence, this shows that while at the low densities typical of the outer atmosphere of halos or of cosmic filaments, the amount of cosmic rays injected by shocks or galaxy formation can have large variations depending on the local dynamics and cosmic variance. At the high density of halos, instead, we always expect a significant amount of cosmic rays resulting from the combination of shocks, AGN feedback and star-formation. Assessing the dependence of this amount and the underlying physical models of galaxy formation and using this to predict the plausible emission of γ-rays and neutrinos from the cosmic web is the subject of the following Section of my Thesis.

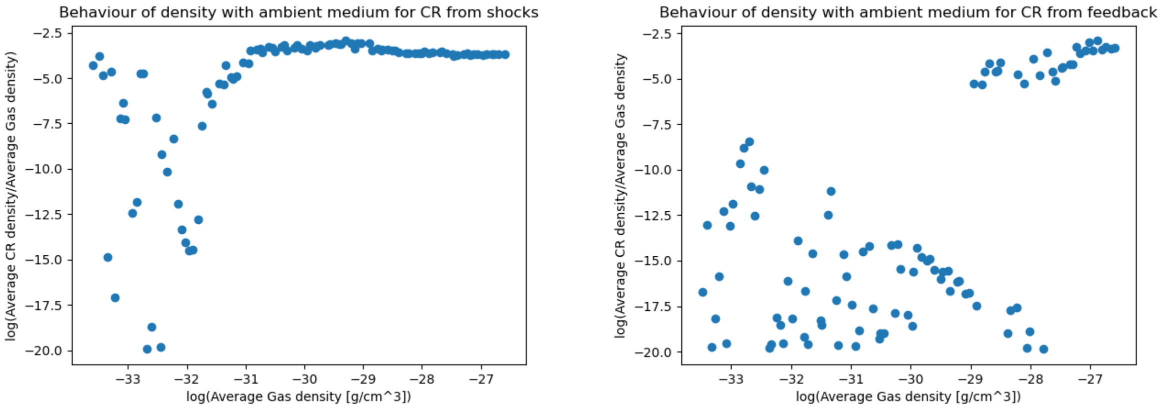

(a) Cosmic rays injected by shocks

(b) Cosmic rays injected by AGNs and star-formation

Figure 31: The figure shows the logarithm of the average normalised CR density plotted against the logarithm of the ambient gas density.

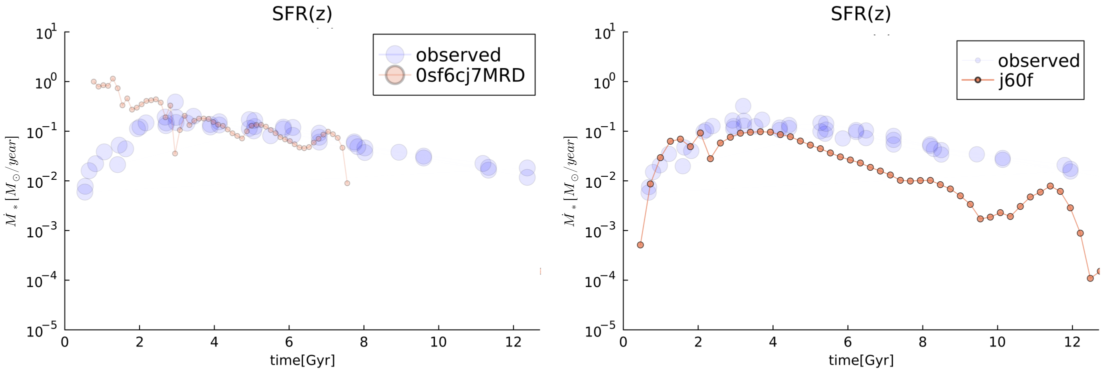

Figure 32: Simulated cosmic star formation history in model A (left) and in model B (right). The big purple points give the observed cosmic star formation derived in Madau and Dickinson (2014).

3.2 Model variations for galaxy formation physics and their impact on Cosmic Rays, gamma-ray and neutrino production

In the remainder of the Thesis, I will focus on the analysis of two large, 1024^3 cells simulations of a $42.5^3\mathrm{Mpc}^3$ comoing volume, in which two different sets of parameters have been adopted to model the processes of star formation, feedback and AGN growth over time. They are compared here to give a sense of the impact of numerical galaxy formation in the final amount of hadronic γ-ray and neutrino emission for the entire cosmic web.

"Model A" adopted a rather aggressive implementation of star formation, by adopting a relatively low gas density to allow for the start of the star formation process in the Kravtsov (2003) model ($n \geq 10^{-4}$part/cm^3), as well as assuming a small minimum mass to form star particles ($m_{*,min} = 10^6 M_\odot$). This results in a quite "bursty" star formation already in the first ~ 2 Gyr of evolution of the simulated universe, and in a basic halt of the star formation process after ~ 7 Gyr, as an effect of an efficient conversion of gas into stars, as well as of the (too) powerful feedback from AGN and star formation implemented in this model, which depleted cold gas from the centre of most simulated halos.

"Model B" adopted instead - after recalibrations of the adopted numerical parameters through trials and errors, in a suite of simulation described in a forthcoming paper (Vazza et al. in prep.) - a more gentled and balanced star formation recipe, in which star particles are only formed at $n \geq 10^{-3}$part/cm^3 densities and with a higher minimum mass ($m_{*,min} = 10^7 M_\odot$). At this resolution, this choice of parameters shifts the peak of the cosmic star formation history at later times, and it overall correctly follows the observed cosmic star formation history in the first ~ 6 Gyr, i.e. after the peak of the cosmic star formation rate, then drops significantly below the cosmic average star formation, but keep producing episodes of intense star formation until the end of the run. In the second part of the simulated evolution, the role of cosmic variance for the limited volume analysed here becomes important, considering that over time the number of massive galaxies is limited in this volume, and subject to random fluctuations which can only be averaged out by resimulating several independent boxes.

3.2.1 Model A

Active Galactic Nuclei and Star-Formation The gamma ray emission from AGNs and star formation at redshift 1.84 is due to a collection of many small sources distributed over the whole volume, as

visible in Figure 33. As time passes, such sources cluster together and increase in size as expected from the hierarchical models of galaxy evolution. The fact that even at low redshift there are many sources of γ-ray emission partly due to the fact that the effect of two different kinds of sources are considered in a single cosmic ray variable and partly to the fact that this specific model has an unrealistic star-formation history.
It is possible to notice a decrease in the average γ-ray flux of about 2 orders of magnitude between redshift 2.981 and redshift 0.02 which also follows the predicted star formation history for model A

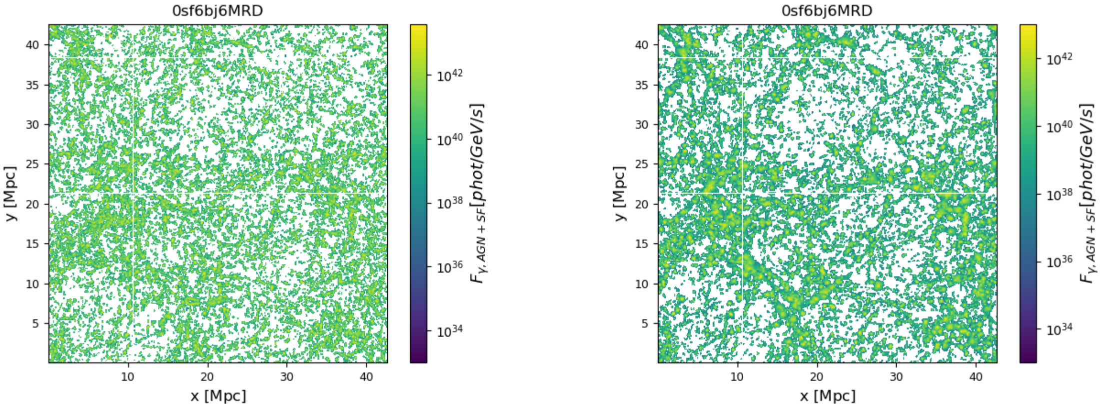

(a) Gamma ray emission from AGNs and star-formation at $z = 1.84$

(b) Gamma ray emission from AGNs and star-formation at $z = 1.065$

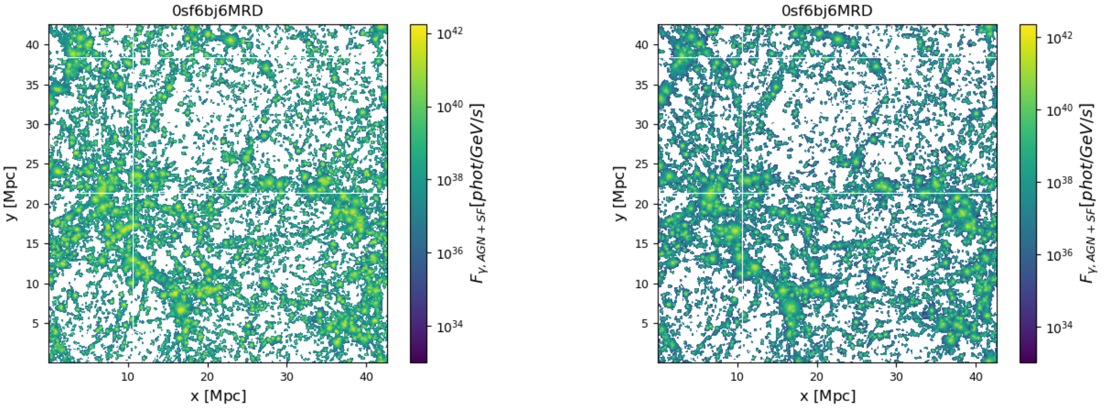

(c) Gamma ray emission from AGNs and star-formation at $z = 0.312$

(d) Gamma ray emission from AGNs and star-formation at $z = 0.02$

Figure 33: Evolution of the γ-ray emission with redshift

Cosmic Shocks The γ-ray emission from cosmic shocks at high redshifts is characterised by small separated sources distributed all over the volume, as shown in Figure 34.This is mostly an artifact of our choice of restricting the computation of γ-ray emission and neutrinos (which is computationally

expensive) only to the peak of the distribution of cosmic rays injected by shocks, which is otherwise very volume filling, although in general contributing to little hadronic emission, owing to the low density of external shocks. As the volume evolves the emission is still localised in small patches, which is consistent with the expectation that the most energetic shocks are localised inside bound structures and not in filaments.
It is also possible to notice an increase by 1 order of magnitude in the average neutrino flux up to redshift 1.455 and a subsequent decrease by 2 orders of magnitude hinting at a peak activity inside galaxies at redshift 1.455.

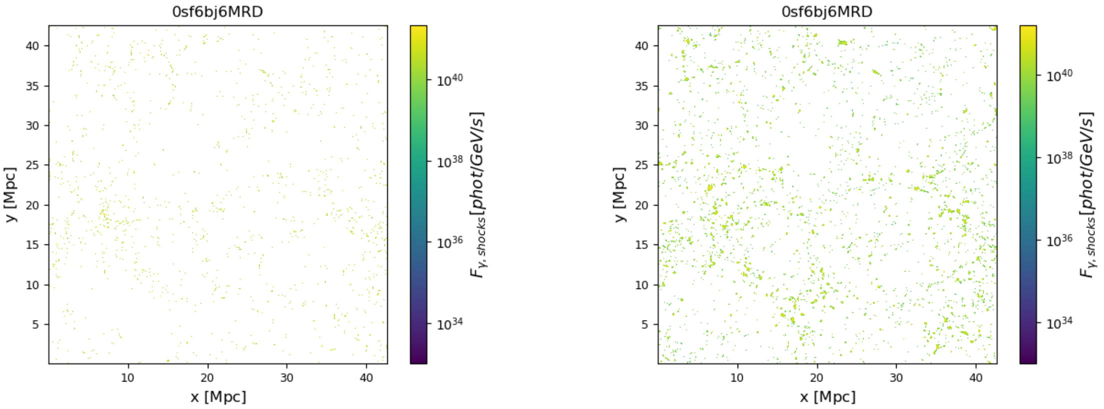

(a) Gamma ray emission from shocks at $z = 1.84$ (b) Gamma ray emission from shocks at $z = 1.065$

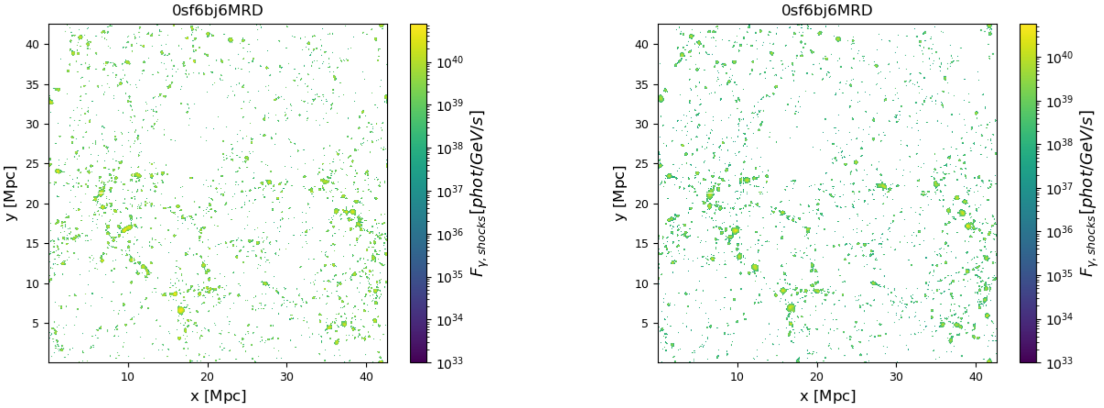

(c) Gamma ray emission from shocks at $z = 0.312$ (d) Gamma ray emission from shocks at $z = 0.02$

Figure 34: Evolution of the γ-ray emission with redshift

3.2.2 Model B

Active Galactic Nuclei In the simulation Active Galactic Nuclei begin their activity at redshift of almost $z \sim 2$. Their gamma ray emission at such epoch appears patchy and localised in the vicinity of the many AGN seeds as visible from Figure 35. The patches are small and distributed all over the volume.

Figure 35 shows the gamma ray emission at different redshifts, it is evident that as time passes the emission diffuses over the volume and the number of sources reduces. At redshift 0.01 for example, most of the volume is filled with low γ-ray emission and only a few tens of clustered hot-spots. The gamma ray flux reduces by one order of magnitude between redshift 1.84 and redshift 0.02.

The evolution of the γ-ray emission mirrors the evolution of AGNs with cosmic time: they are more common and more active at high redshifts.

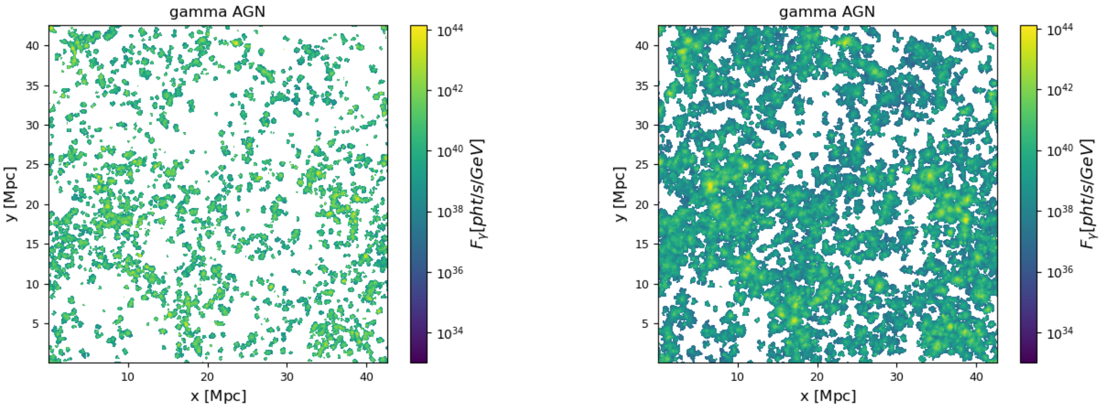

(a) Gamma ray emission from AGNs at $z = 1.84$

(b) Gamma ray emission from AGNs at $z = 1.22$

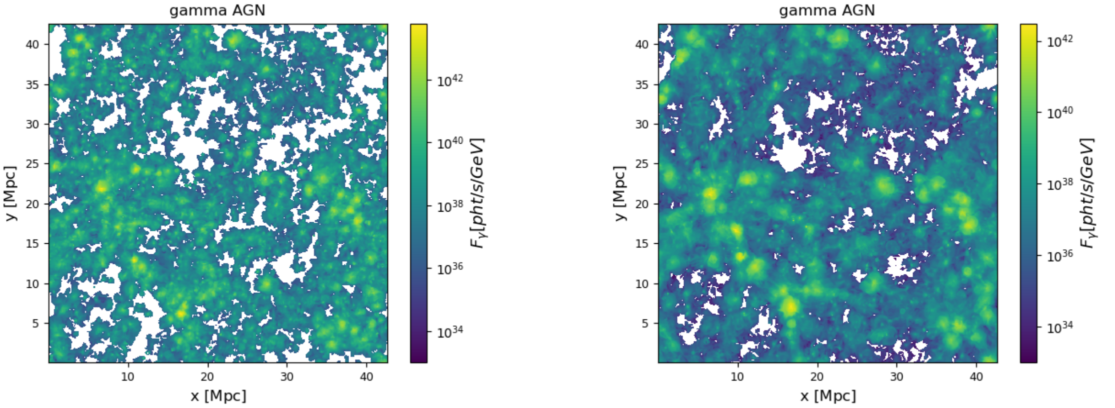

(c) Gamma ray emission from AGNs at $z = 0.968$

(d) Gamma ray emission from AGNs at $z = 0.02$

Figure 35: Evolution of the γ-ray emission with redshift

Cosmic Shocks For run B I computed the γ-ray and neutrino emission for a large population of cells with cosmic rays injected by shocks, down to emission levels which are virtually impossible to observe. The γ-ray emission from cosmic shocks at high redshift is shown in Figure 36, it appears as filamentary and widely distributed over the cosmic volume. As the simulation evolves, the flux decreases,

the filaments look more spaced and it is possible to appreciate the formation of clumps. The flux of γ-rays injected by cosmic shocks overall decreases by three orders of magnitude between redshift 3 and redshift 0.02.
The evolution in the gamma ray emission mirrors the evolution of the Large Scale Structure, combined with the effect that while high-redshift shocks develop in un-virialised and dense environments, the ones at lower redshift on average are at the boundaries of virialised structures and contribute to lower γ-ray emission because of their low density.

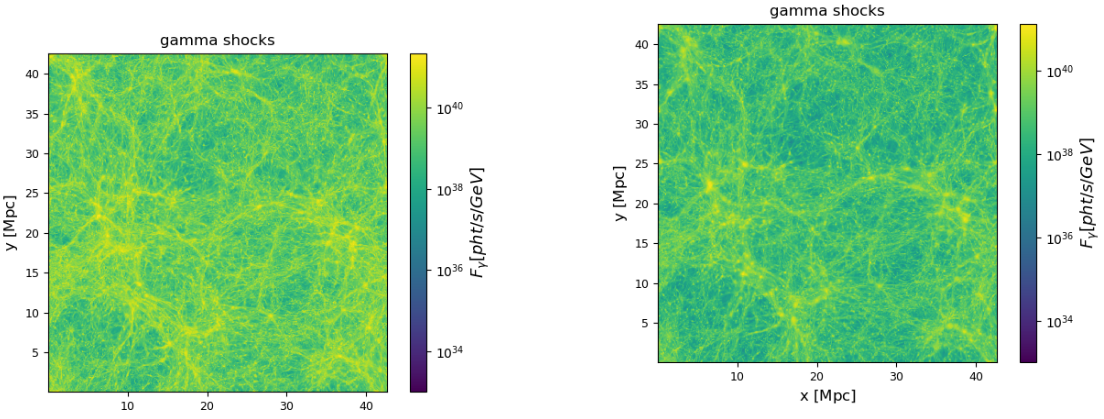

(a) Gamma ray emission from cosmic shocks at $z = 1.84$

(b) Gamma ray emission from cosmic shocks at $z = 1.22$

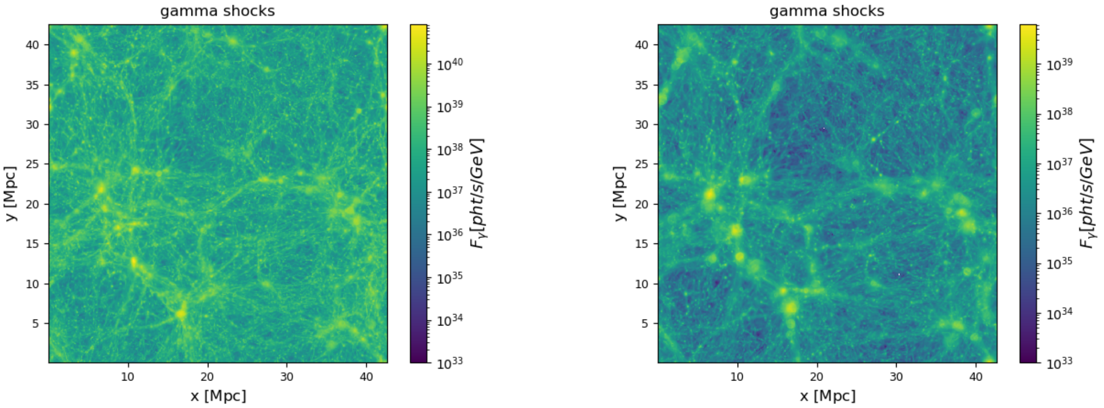

(c) Gamma ray emission from cosmic shocks at $z = 0.968$

(d) Gamma ray emission from cosmic shocks at $z = 0.02$

Figure 36: Evolution of the γ-ray emission with redshift

Star Formation The gamma ray emission from star formation is represented in Figure 37. At high redshift it appears as a mixture of many thin filaments and small clumps distributed over the whole volume. As time passes the emission looks clumpier and located in a few large hotspots. The γ-ray

flux reduces by about three orders of magnitude between redshift 3 and reshift 0.02, with a trend again driven by the drop of simulated cosmic star-formation.
The evolution of this component of the γ-ray emission mirrors the evolution of galaxies: at high redshift they are smaller but they have higher star formation rates, while at low redshift there are bigger but less star forming galaxies.

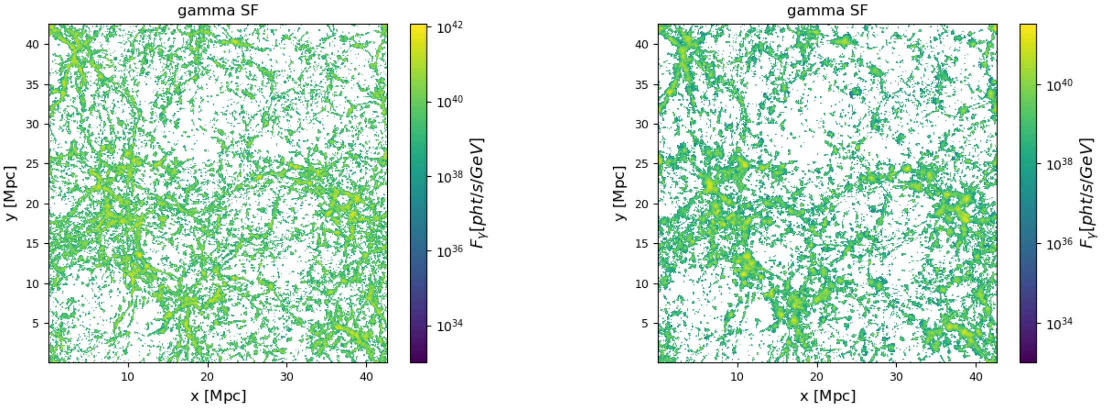

(a) Gamma ray emission from star formation at $z = 1.84$

(b) Gamma ray emission from star formation at $z = 1.22$

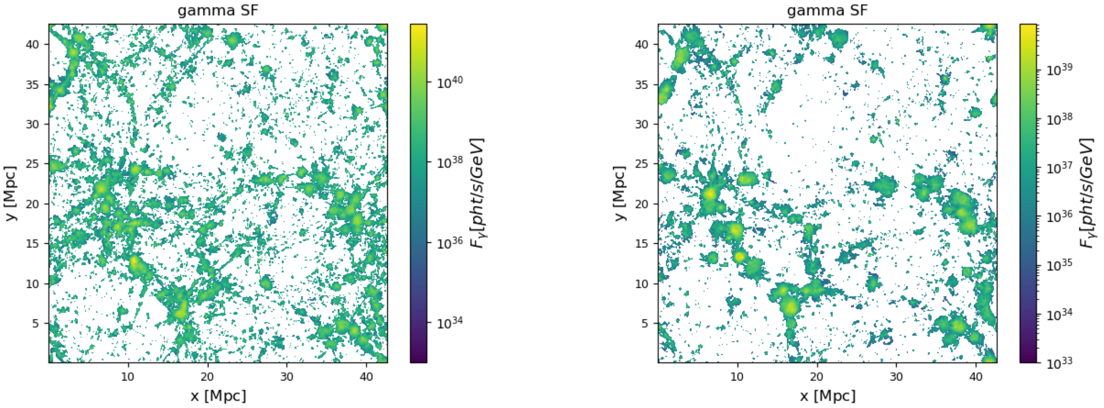

(c) Gamma ray emission from star formmation at $z = 0.968$

(d) Gamma ray emission from star formation at $z = 0.02$

Figure 37: Evolution of the γ-ray emission with redshift

3.3 Neutrinos

3.3.1 Model A

Active Galactic Nuclei and Star-Formation The evolution of the neutrino emission from AGNs and star-forming galaxies is shown in Figure 38 and it closely follows the trends already reported for the γ-ray emission.

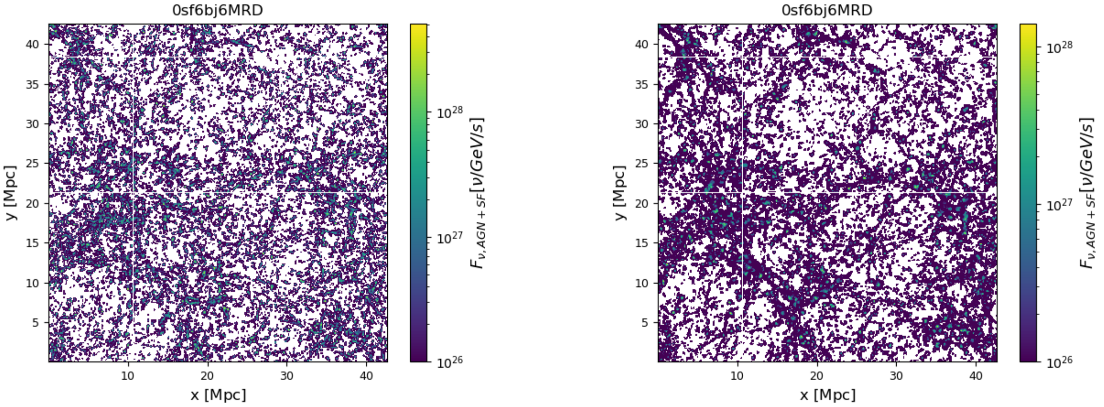

(a) Neutrino emission from AGNs and star formation at $z = 1.84$

(b) Neutrino emission from AGNs and star forming galaxies at $z = 1.065$

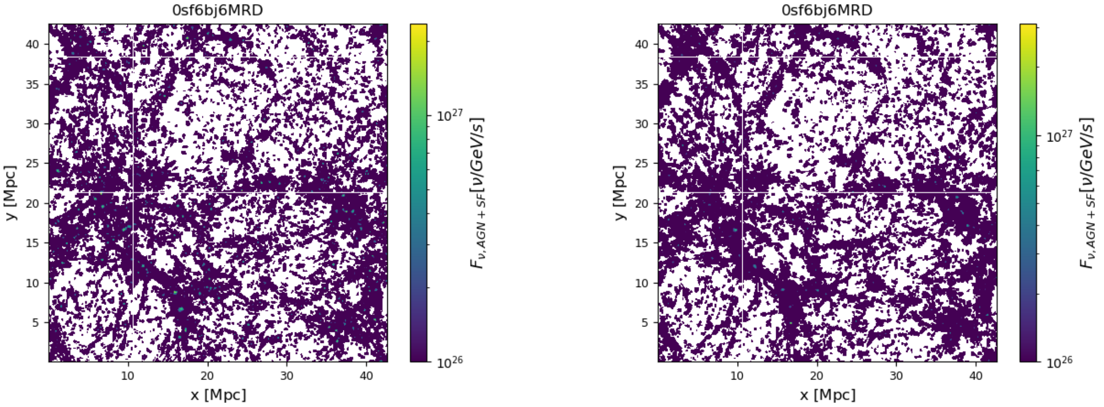

(c) Neutrino emission from AGNs and star forming galaxies at $z = 0.312$

(d) Neutrino emission from AGN and star forming galaxies at $z = 0.02$

Figure 38: Evolution of the neutrino emission with redshift

Cosmic Shocks The neutrino emission from cosmic shocks at different redshifts is shown in Figure 39 and it closely follows the trends already reported for the γ-ray emission.

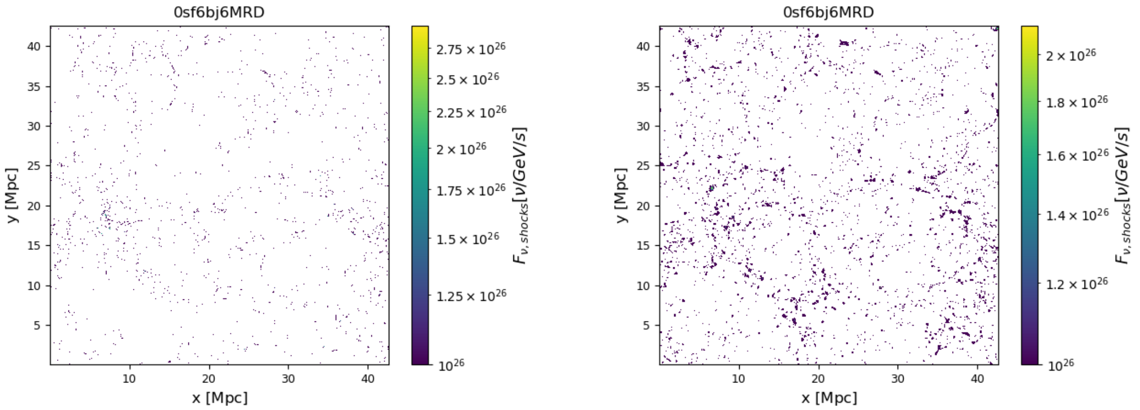

(a) Neutrino emission from shocks at $z = 1.84$

(b) Neutrino emission from shocks at $z = 1.065$

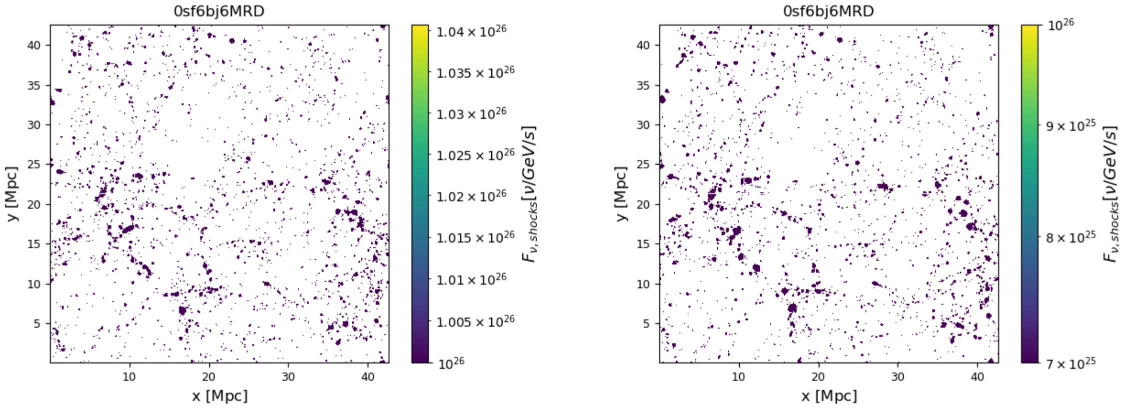

(c) Neutrino emission from shocks at $z = 0.312$

(d) Neutrino emission from shocks at $z = 0.02$

Figure 39: Evolution of the neutrino emission with redshift

3.3.2 Model B

Active Galactic Nuclei The emission of neutrinos from AGN, shown in Figure 40, evolves with redshift in a similar way as the corresponding γ-ray emission.

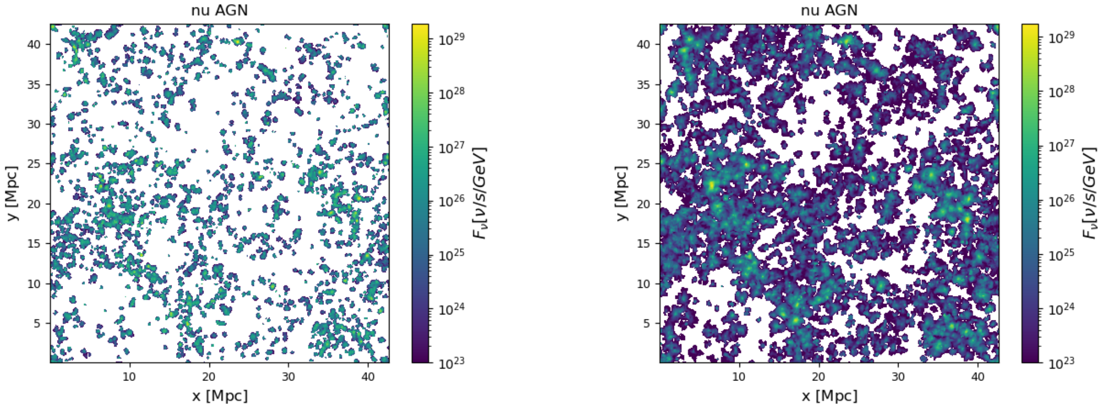

(a) Neutrino emission from AGNs at $z = 1.84$ (b) Neutrino emission from AGNs at $z = 1.22$

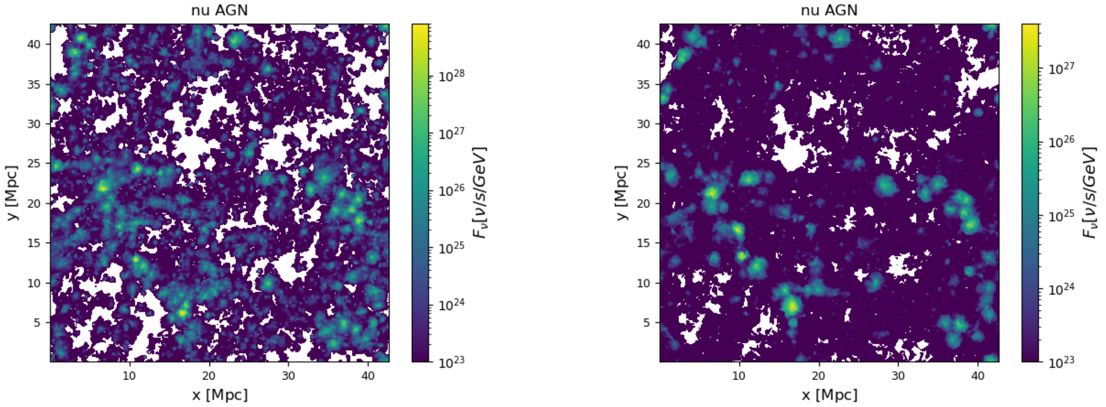

(c) Neutrino emission from AGNs at $z = 0.968$ (d) Neutrino emission from AGNs at $z = 0.02$

Figure 40: Evolution of the neutrino emission with redshift

Cosmic Shocks Figure 41 shows the evolution of neutrinos injected by cosmic shocks and it closely follows the corresponding γ-ray evolution.

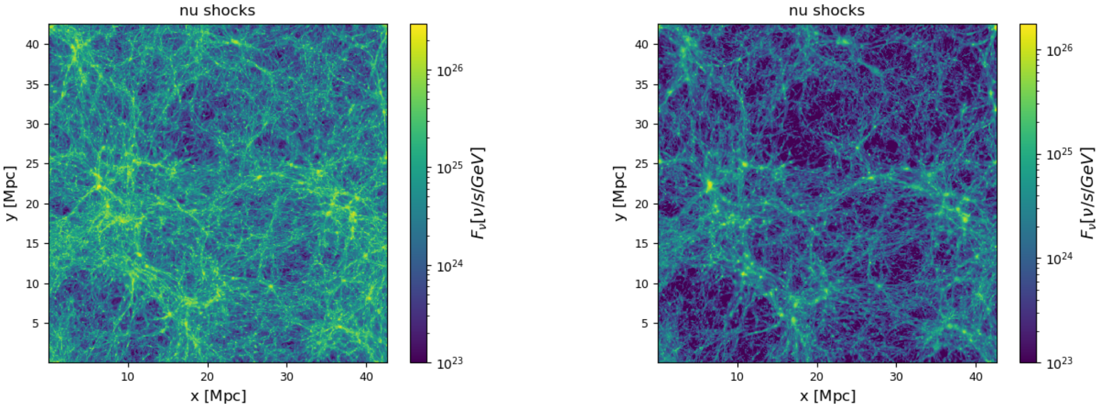

(a) Neutrino emission from cosmic shocks at $z = 1.84$ (b) Neutrino emission from cosmic shocks at $z = 1.22$

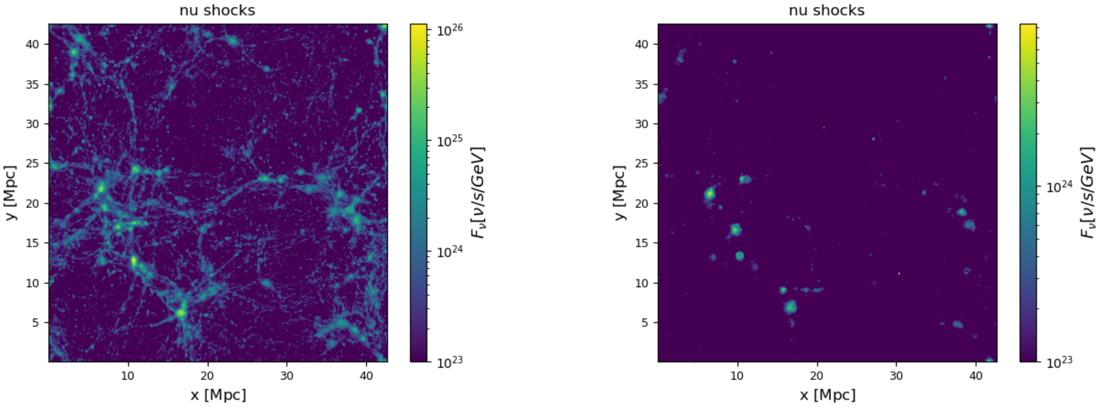

(c) Neutrino emission from cosmic shocks at $z = 0.968$ (d) Neutrino emission from comsic shocks at $z = 0.02$

Figure 41: Evolution of the neutrino emission with redshift

Star Formation

The neutrino emission from star formation is shown in Figure 42 and it closely follows the corresponding γ-ray emission.

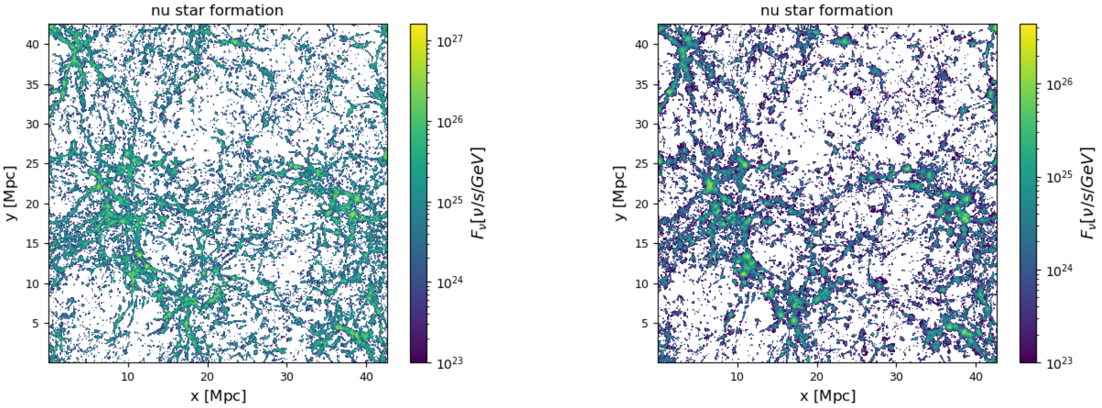

(a) Neutrino emission from star formation at $z = 1.84$ (b) Neutrino emission from star formation at $z = 1.22$

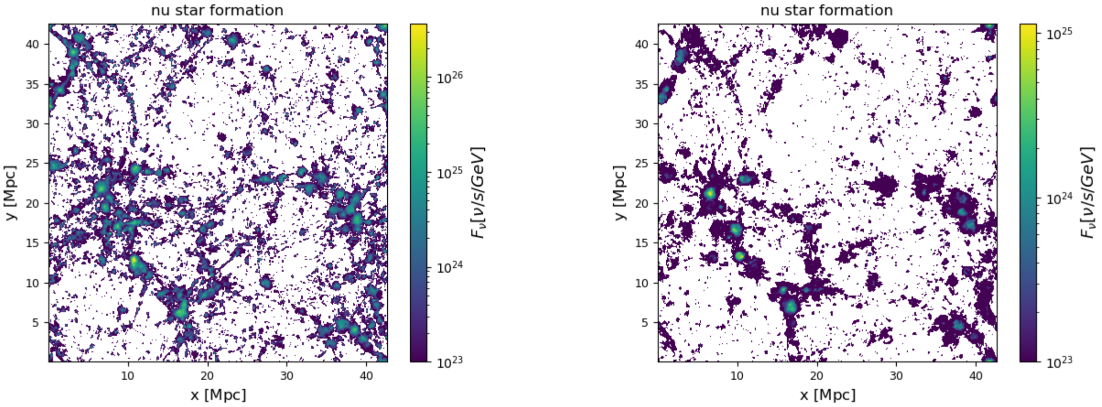

(c) Neutrino emission from star formation at $z = 0.968$ (d) Neutrino emission from star formation at $z = 0.02$

Figure 42: Evolution of the neutrino emission with redshift

3.4 The simulated gamma-ray and neutrino backgrounds

A key result of my work is to use the simulated emissions discussed in the previous section to produce a model for the γ-ray and neutrino background extrapolated for the entire sky and integrated up to high redshift ($z = 3$ here). The gamma-ray flux integrated over the simulation's volume at different redshifts is shown in Figure 43. In the Figure, the left panel describes the evolution for model A while the right one describes the evolution for model B. It is possible to notice that in both models γ-rays produced by AGNs are the dominant component, at least up to redshift $z = 2$. For both models the γ-ray flux from AGN decreases by an order of magnitude between redshift $z = 2$ and redshift $z = 0$. However, model B presents a sudden decrease in the emission at $z > 2$ that is not visible in model A. The reason might be ascribed to an unrealistic modelling of star-formation for model A, resulting in higher star-formation rates already at $z \sim 3$. The sudden decrease in flux above redhsift $z = 2$ present in model B marks the epoch during which AGNs are not yet active in our model and therefore cosmic shocks and star forming galaxies are the only γ-ray sources.

In model A the emission from shocks shows a peak at redshift $z = 1.5$ where the emission is about one order of magnitude greater than at redshift 0 and at redshift $z = 3$.

In model B the shape of the emission form cosmic shocks differs from the one in model A. In fact, at redshift $z = 0$ its value is almost one order of magnitude below the one of model B at the same redshift and the emission increases steadily by almost 3 orders of magnitude until redshift $z = 3$. The emission from shocks and star-formation seems to be of the same order of magnitude and to have a similar shape. As commented above, for run A I only included the peaks of cosmic rays from shocks, which have reduced the integrated contribution from the volume filling population of shocks.

The figure also shows the errorbars associated with each time snapshot and they represent my estimate of the cosmic variance, determined via bootstrapping within the two-dimensional map obtained by marginalising over the z axis. The code used to this end is presented in Section 7, it samples the area of two snapshots (one located at high redshift and the other located at low redshift) in 10 randomly sized and randomly located areas and for each of them it calculates the γ-ray and neutrino emission. The ratio between the semi difference between the highest and the lowest emission and the total emission provides an estimate of the snapshot's relative error. Since the relative errors of the high-redshift and low-redshift snapshots were similar, it was possible to use them as the relative errors of all snapshots. The fact that the errorbars are relatively small means that the emission is dominated by many small sources diffuse throughout the volume as confirmed also by the morphological studies. The large errorbars present for the shock component in model A at high redshifts result from the fact that only very few sources are detected.

Figure 44 shows the neutrino flux integrated over the simulated volume. The characteristics for both models are the same as the ones already discussed for the γ-ray emission.

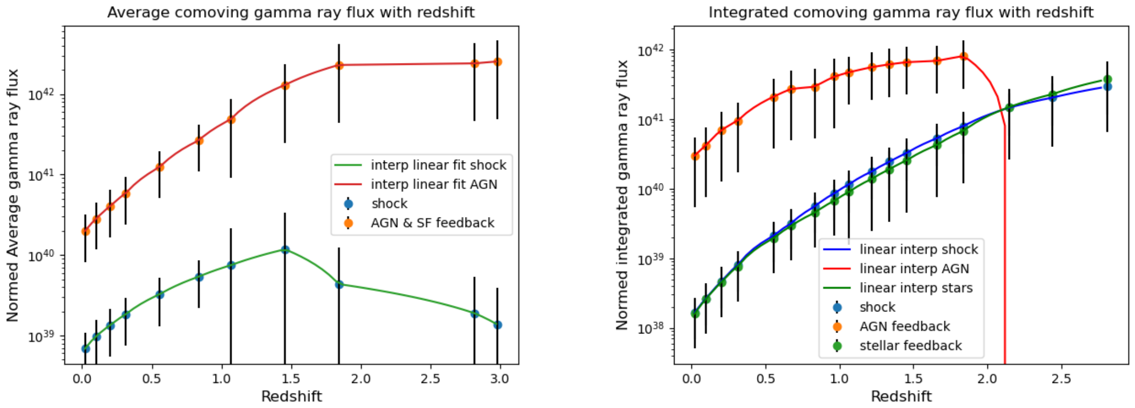

(a) (b)

Figure 43: The redshift evolution of the background *gamma*-ray flux for model A (on the left) and for model B (on the right). The figure also shows the time snapshots used for the interpolation. The errorbars at each epoch show our estimate of the cosmic variance, calculated by bootstrapping within the two-dimensional map obtained by marginalising over the z axis. Notice the two different range of scales used for the two integrated fluxes

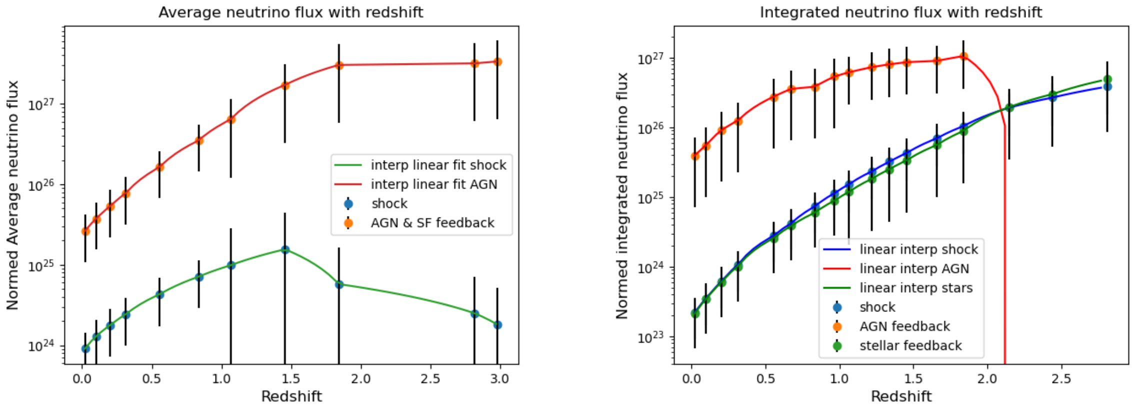

(a) (b)

Figure 44: The redshift evolution of the background neutrino flux for model A (on the left) and for model B (on the right). The figure also shows the time snapshots used for the interpolation. The errorbars at each epoch show our estimate of the cosmic variance, calculated by bootstrapping within the two-dimensional map obtained by marginalising over the z axis.

3.5 Cumulative flux

Based on the previous results, we can say that model B is the more realistic of the two analysed in this work, hence in the following it will be the one to be compared to the real observational data. Figure 45 shows the contribution from each redshift bin to the γ-ray background. As already explained in Section 3.4, I interpolated the total simulated fluxes from each snapshots in order to obtain a finer redshift binning. Next, I corrected the emission from each redshift bin for cosmological effects, such as the bandwidth compression, through equation 28. Finally, the cumulative emission results form the sum of the emission from that reshift bin and all of its preceding ones.

From Figure 45, it is possible to notice that the main contribution to the background comes form AGNs. However the cumulative γ-ray flux up to redshift 3 is inconsistent with the $Fermi$-LAT observation for the 0.5-200 GeV energy band. In particular the cumulative flux is a factor 5 above the observed limit. Such a discrepancy could be attributed to an overestimation for the efficiency in the production of cosmic rays or to attenuation of gamma rays inside the sources. Of the two hypothesis the first one is the most probable one because the injection efficiency is highly uncertain and may vary according to the type of AGN or the type of environment, furthermore, attenuation would require the further assumption of the presence of a high density photon field.

The cumulative flux for neutrinos, instead, in shown in Figure 46. It is about 2 orders of magnitude below the observed IceCube limit for the $10^5 - 10^6$ energy band. The dominant component for the flux is the one originating form AGNs as predicted by Buson et al. (2023) and Padovani et al. (2024). The star-formation and cosmic shocks components provide a similar contribution which is about 1 order of magnitude lower than the AGN's one at redshift 3.

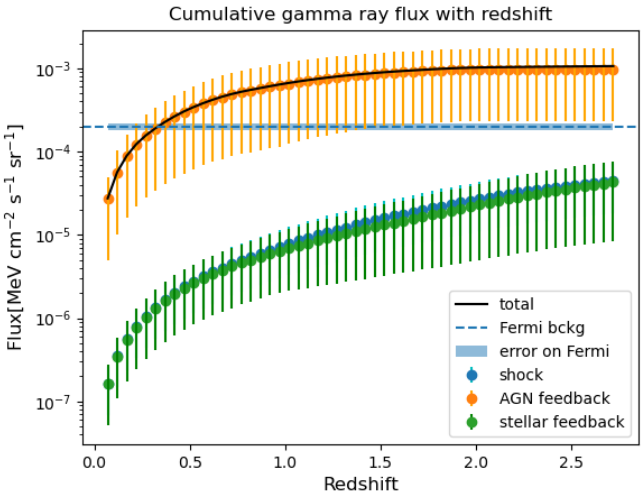

Figure 45: The figure displays the contribution to the γ-ray cumulative flux coming from different redshifts; *in orange* the contribution from AGNs, *in blue* the contribution from cosmic shocks, *in green* the contribution from star-formation, *in black* the overall contribution from all populations, *in blue dotted* the $Fermi$-LAT limit for the γ-ray background in the energy band.

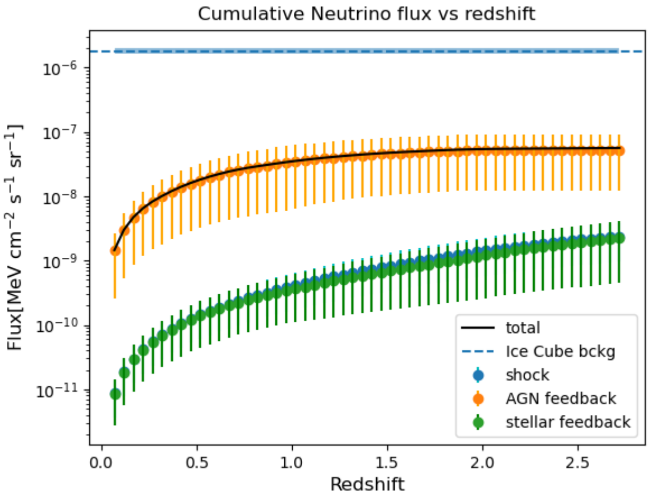

Figure 46: The figure displays the contribution to the neutrino cumulative flux coming from different redshifts; *in orange* the contribution from AGNs, *in blue* the contribution from cosmic shocks, *in green* the contribution from star-formation, *in black* the overall contribution from all populations, *in blue dotted* the IceCube limit for the neutrino background in the $10^5 - 10^6$ GeV energy band.

The reference model used for the acceleration of CRs by AGN in this simulation assumed a fixed ratio between the number density of cosmic rays injected by jets, and the thermal gas density: $\xi_{AGN} = 0.01$ (Sec 2.2). This number is highly uncertain, and it can also possibly vary with the typology of AGN feedback event, and the environment where the AGN is located, as the CR content of jets on $\sim 10 - 100$ kpc can also be affected by the interaction with the environment (e.g. Croston et al., 2018).

For the acceleration efficiency of CRs by cosmic shocks, the adopted simulation used the Mach number-dependent formula by Kang (2020) (see also Fig.24). As discussed already, the CR injection efficiency by cosmic shocks is still uncertain, and even more so in the case of CR protons, whose diffuse hadronic γ-ray emission is not detected in clusters of galaxies. Moreover, effects dependent on the obliquity of shocks (i.e. the angle between the shock velocity and the upstream magnetic field vector) are expected to quench the acceleration efficiency of protons, for quasi-perpendicular geometries. Since the latter are statistically way more dominant in large-scale structures (e.g. Wittor et al., 2020), it is therefore plausible that the baseline assumption given by the $\xi_{\text{shocks}}(\mathcal{M})$ in Eq.18 overestimates the total number of injected CR protons in the simulation.

Therefore, if we interpret the mismatch between the *Fermi*-LAT background limits as a joint constrain on ξ_{AGN} and $\xi_{\text{shocks}}(\mathcal{M})$, we can renormalise a posteriori these parameters to be $\xi'_{AGN} = \frac{0.01}{X}$ and $\xi'_{\text{shocks}}(\mathcal{M}) = \frac{\xi_{\text{shocks}}(\mathcal{M})}{X}$, where X is the ratio between the simulated background as if produced only by AGN and cosmic shocks and the observed γ-ray background ($X \approx 6.6$).

This is what is shown in the recalibrated cumulative γ-ray flux shown in Figure 47, which considers the γ-ray emission by AGN and cosic shocks rescaled by a factor $X = 6.6$ in order to match the *Fermi*-LAT limit. As previously observed the dominant emission comes form AGN which contribute to 74.1 % of the background while the star-formation is responsible for about 22.4% of the background and shocks contribute to about 3.5% of the observed background.

The neutrino cumulative flux, instead, is still 2 orders of magnitude below the IceCube limit. In this case as well the dominant contributors to the diffuse flux are AGN, however they make up only for 0.4% of the observed neutrino diffuse flux.

In summary, my work suggests that the possible following simple relation can be used to highlight the range of possible values allowed for the acceleration efficiencies of CRs by the three investigated mechanisms (combined together), based on the comparison with the real γ-ray background in the 0.5-200 GeV energy range probed by *Fermi*-LAT.

$$F_{\gamma,0.5-200GeV} \approx 2 \cdot 10^{-4} \frac{\mathrm{MeV}}{\mathrm{cm}^2\ \mathrm{s}\ \mathrm{sr}} \cdot \left[0.741 \frac{\xi_{\mathrm{AGN}}}{1.5 \cdot 10^{-3}} + 0.224 \frac{\xi_{\mathrm{SF}}}{10^{-5}} + 0.035 \frac{\xi_{\mathrm{shocks}}(\mathcal{M}=3)}{4.5 \cdot 10^{-5}}\right] \tag{29}$$

where in the case of shocks, we referred for simplicity the efficiency constrained by my Thesis to the reference value for $\mathcal{M} = 3$ shocks, which are responsible for most of the dissipation of shock kinetic energy in the cosmic web (e.g. Bykov et al., 2019).

Likewise, for the neutrino flux we can derive:

$$F_{\nu,10^5-10^6GeV} \approx 1.8 \cdot 10^{-6} \frac{\mathrm{MeV}}{\mathrm{cm}^2\ \mathrm{s}\ \mathrm{sr}} \cdot \left[0.004 \frac{\xi_{\mathrm{AGN}}}{1.5 \cdot 10^{-3}} + 0.001 \frac{\xi_{\mathrm{SF}}}{10^{-5}} + 0.0002 \frac{\xi_{\mathrm{shocks}}(\mathcal{M}=3)}{4.5 \cdot 10^{-5}} + 0.9948\right] \tag{30}$$

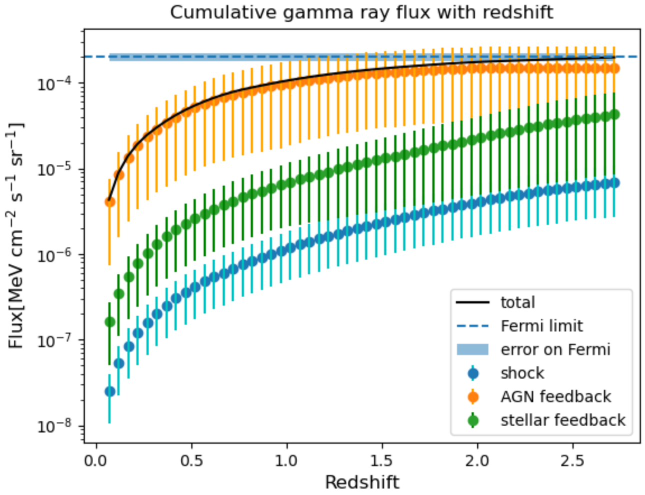

Figure 47: The figure displays the contribution to the γ-ray cumulative flux coming from different redshifts once rescaled to match observations; *in orange* the contribution from AGNs, *in blue* the contribution from cosmic shocks, *in green* the contribution from star-formation, *in black* the overall contribution from all populations, *in blue dotted* the *Fermi*-LAT limit for the γ-ray background in the energy band.

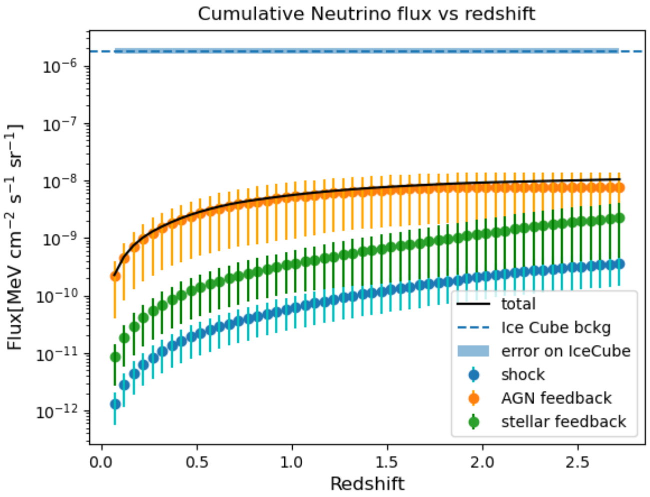

Figure 48: The figure displays the contribution to the contribution to the neutrino cumulative flux coming from different redshifts once rescaled to match observations; *in orange* the contribution from AGNs, *in blue* the contribution from cosmic shocks, *in green* the contribution from star-formation, *in black* the overall contribution from all populations, *in blue dotted* the IceCube limit for the neutrino background in the $10^5 - 10^6$ GeV energy band.

4 Discussion & Future Work

I have presented the results of the application of a status-of-art cosmological simulation of the evolution of large-scale structures to perform. For the first time in the literature, a joint modelling of the γ-ray and neutrino emission from several key mechanisms believed to be responsible for acceleration of cosmic rays on extragalactic scales: the injection of cosmic rays at structure formation shocks through diffuse shocks acceleration, the injection of cosmic rays by star formation, and the injection of cosmic rays by AGN feedback events.

The fact that the three main physical "ingredients" included in the simulations to inject cosmic rays and produce γ-ray and neutrino emission can account for the whole observed γ-ray emission, but only for 1% of the neutrino emission, hints towards the fact that the (rather advanced) model used here is, still, probably incomplete. Considering that, to a first order, the simulated trends of the star formation and AGN feedback in the simulation have been calibrated to reasonably reproduce observed global trends of galaxies (like the cosmic star formation history, the stellar mass function and the correlation between the black hole mass and the host galaxy mass), as well as the local radio and γ-ray emission properties of galaxies, to understand the reasons for the discrepancy I can focus on (at least) two main aspects.

Missing physics: photo-pion production and attenuation of γ-rays

The first aspect could be related to missing physical mechanisms inside the sources, such as a) photo-pion production of neutrinos or b) attenuation of γ-ray photons. The simulation presented here assumes that neutrinos are produced through proton-proton collisions only. However, another important mechanism believed to be at work in astrophysical sources is photo-pion production of neutrinos. This mechanism is particularly important for sources with large densities of photons, like the surroundings of AGN indeed. In this case, the interaction between high-energy cosmic rays and a radiation field produce neutral and charged pions whose decay, in turn, generates neutrinos and γ-rays (Spurio, 2018). If photo-pion production is at work in real sources, together with proton-proton collisions, then our estimate for the neutrino and γ-ray emission would increase by a factor ~ 3 (e.g. Murase, 2022). This would result yet again in the overproduction of our simulated γ-ray background, compared to the and observed γ-ray background measured by *Fermi*-LAT.

Another potentially important physical mechanism that is linked to photo-pion production, and which is not included in this analysis, is the attenuation of γ-ray emission. Indeed the existence of neutrino sources opaque to GeV-TeV γ-rays has been suggested as a solution for the fact that otherwise the γ-ray emission accompanying the neutrino flux, at energies $E_\nu = 1 - 10$ TeV, would exceed the observed isotropic gamma ray background (Murase et al., 2024). The origin of the attenuation could be attributed to the fact that, if the source is compact enough, its emitted γ-rays can interact with intense photon fields generating electron and positron pairs through Breit-Wheeler process ($\gamma + \gamma \rightarrow e^- + e^+$). Attenuation of γ-rays needs to be taken into account in particular in photo-pion production scenarios, because the same population of target photons responsible for the neutrino production should also interact with the pionic γ-rays causing the attenuation. The opacity for the Breit-Wheeler process ($\tau_{\gamma\gamma}$) and the energy-loss length of protons involved in photo-pion production ($\tau_{p\gamma}$) are approximately related through their cross-section: $\tau_{\gamma\gamma} \sim 10^3 \tau_{p\gamma}$. Then a target photon field capable of generating neutrinos and characterised by $\tau_{p\gamma} \sim 0.1$, will not be transparent to pionic γ-rays, because of the high opacity caused by 2 photon interactions $\tau_{\gamma\gamma} \sim 100$ (Kun et al., 2024). Hence the high density photon fields required for the acceleration of $\sim$ PeV neutrinos might increase the optical thickness for photons at 1 GeV (e.g. Reimer et al., 2019). The electron and positron pairs can produce electromagnetic cascades down to MeV γ-rays or hard X-rays (IceCube Collaboration, 2024), i.e. outside of the energy band considered in this study. Observational clues for the presence of attenuation inside AGN come from the fact that in many AGN the γ-ray and neutrino emission do not seem to be related (Buson et al., 2022, 2023; Aartsen and et al, 2017).

Missing sources: Seyfert galaxies

The second aspect could be related to astrophysical sources of neutrinos which have not been modelled in the suite of simulations I analysed in my work. In this respect, Padovani et al. (2024) predicts that the sources of neutrinos with energies below 1 PeV might be non-jetted AGN. Since neutrino signals have been associated with Seyfert galaxies (Neronov et al., 2023; IceCube Collaboration, 2024) and since Seyfert galaxies are believed to be non-jetted AGN, their addition to the model might improve the current constraints. The high density and high photon fields present in the proximity of the black hole might indeed offer suitable conditions for neutrino production (IceCube Collaboration, 2024) and the multi-messenger modelling of a Seyfert galaxy associated with neutrino emission (NGC 1068), predicts that the neutrino emission lies within 100 Schwarzschild radii from the black hole (Murase, 2022). In particular, the neutrino production in Seyfert galaxies is believed to be related to the X-ray emitting coronae (Murase, 2022; Neronov et al., 2023). The most favourable scenarios include cosmic rays accelerated either in the coronae or in shocks interacting with X-rays from the coronae (photo-pion scenario) or with inflows (proton-proton scenario) (Murase, 2022). The same model suggests the presence of strong attenuation of the GeV-TeV γ-ray emission (Murase, 2022) due to the optical thickness of the AGN core, therefore the addition of Seyfert galaxies to my model should not affect the simulated γ-ray background (which is computed in the energy band $0.5 - 200$ GeV). On the other hand, it could be possible to place limits on the production of neutrinos from the simulated Seyfert galaxies by comparing the simulated fluxes not only with the neutrino diffuse background but also with the signals detected from nearby Seyfert galaxies.

A proper inclusion of the physics likely to be at work in Seyfert galaxies is non trivial at the spatial resolution of the simulation analysed in my Thesis. In order to incorporate this emission modality of neutrinos, either a challenging sub-parsec spatial resolution must be achieved (either with very aggressive adaptive mesh refinement, or with other numerical approaches) in order to resolve the acceleration process of cosmic rays by the hot X-ray corona, or sub-grid models for the same process must be designed and tested, using the resolved information of the host galaxies (e.g. their mass, accretion rate and black hole properties) for a proper calibration of the hot corona properties.

5 Conclusion

The main goal of this work was the analysis of a cosmological simulation in order to assess, for the first time in the literature, the contribution of three different kind of sources (AGN, cosmic shocks and star-formation) to the extragalactic neutrino diffuse background. The reason behind this lies in the fact that despite many efforts in understanding the origin of the extragalactic neutrino diffuse background, its sources remain unknown. The choice of AGN, cosmic shocks and star-formation as the possible sources of neutrino emission can be traced back to the fact that all of them are capable of accelerating cosmic rays to high energies, and the interactions of high energy cosmic rays with thermal gas (proton-proton collisions) or with photon fields (photo-pion production) are bound to generate neutrinos and gamma-rays.

The simulation covered a comoving volume of $(42.5)^3\mathrm{Mpc}^3$ with 1024^3 cells with a resolution of 41.5 kpc per cell. AGN, star-formation and shocks were simulated realistically and considered as acceleration sources of cosmic rays, with a few tuneable parameters related to the injection efficiency of each mechanism.

I modelled the neutrino emission in the energy band $10^5 - 10^6$ GeV and the γ-ray emission in the energy band $0.5 - 200$ GeV. The joint modelling of these two backgrounds is crucial for my study, since from the comparison between the simulated γ-ray background and the real one observed by *Fermi*-LAT, I can limit the maximum cosmic ray proton acceleration efficiency of various processes also related to the production of high-energy neutrinos.

The procedure I followed in computing the emission is the following:

- I assumed proton-proton collision to be the main neutrino production mechanism, and I computed the emission of neutrinos and γ-rays for all cells of the simulation, for several redshifts and for CRs injected by the three different mechanisms.

- I computed the comoving flux of the neutrino and γ-ray emission between redshift 0 and redshift 3 for two slightly different runs of the same simulation. The fluxes were calculated on the basis of the cosmic ray energy density obtained from the simulation and making use of the formalism developed by Pfrommer and Ensslin (2004).
- One of the two runs (here called "Model A") was found to be too "bursty" and to overpredict the flux at $z > 2$. Model B instead was found to be accurate and this is why the subsequent analysis focused on this run.
- Once the flux was corrected for cosmological effects (such as bandwidth compression and cosmological dimming), I computed the cumulative background neutrino and γ-ray fluxes from the entire Universe, in the $0 \leq z \leq 3$ redshift range.

Then I compared the simulated neutrino and γ-ray backgrounds with the observed IceCube diffuse flux and to the *Fermi*-LAT background respectively. It was clear that the γ-ray emission exceeded the measured *Fermi*-LAT background by a factor ~ 5. A plausible explanation of this seemed to lie in the uncertainty of the injection efficiency of AGN and of the cosmic ray acceleration from shocks. The injection efficiency of star-formation, despite being uncertain as well, was thought to be correct since a rescaling would have meant a larger scatter in the relation plotted in Fig.25 hence an unphysical model of star-fromation. Since the cumulative fluxes of AGN and cosmic shocks had to be rescaled keeping

the star-formation flux as it was, their values had to be reduced by a factor ~ 6.
The simulated γ-ray background, once properly rescaled to be consistent with *Fermi*-LAT observations, allows to derive the following simple expression, relating the (poorly constrined) acceleration efficiency of CRs of the various acceleration channels considered in my Thesis, and the integrated γ-ray background emission:

$$F_{\gamma,0.5-200GeV} \approx 2 \cdot 10^{-4} \frac{\mathrm{MeV}}{\mathrm{cm}^2\ \mathrm{s}\ \mathrm{sr}} \cdot \left[0.741 \frac{\xi_{\mathrm{AGN}}}{1.5 \cdot 10^{-3}} + 0.224 \frac{\xi_{\mathrm{SF}}}{10^{-5}} + 0.035 \frac{\xi_{\mathrm{shocks}}(\mathcal{M}=3)}{4.5 \cdot 10^{-5}}\right] \tag{31}$$

The neutrino background, instead was found to have the following expression:

$$F_{\nu,10^5-10^6GeV} \approx 1.8 \cdot 10^{-6} \frac{\mathrm{MeV}}{\mathrm{cm}^2\ \mathrm{s}\ \mathrm{sr}} \cdot \left[0.004 \frac{\xi_{\mathrm{AGN}}}{1.5 \cdot 10^{-3}} + 0.001 \frac{\xi_{\mathrm{SF}}}{10^{-5}} + 0.0002 \frac{\xi_{\mathrm{shocks}}(\mathcal{M}=3)}{4.5 \cdot 10^{-5}} + 0.9948\right] \tag{32}$$

It is worth highlighting that the three sources of cosmic rays considered in the model (cosmic shocks, AGN and star-formation) can plausible account for the entire observed γ-ray background, and yet their overall contribution to the neutrino background is less than 1%.

This suggests the possibility that the model might be incomplete. Two possible directions to take into account to improve the model are:

- including other physical phenomena: photo-pion production and attenuation of γ-rays are believed to be at work in astrophysical sources. Photo-pion production should result in neutrino and γ-ray emission through the interaction of high energy cosmic rays and photons. Attenuation, instead, results in a decrease of the γ-ray flux due to photon-photon interaction producing electron and positron pairs.

- including new sources: the addition of Seyfert galaxies might be of fundamental importance since theoretical models by Padovani et al. (2024) suggest that non-jetted AGN such as Seyferts might dominate the neutrino emission at energies below 1 PeV and there is growing evidence towards the fact that this class of AGN is capable of emitting neutrinos (Neronov et al., 2023; IceCube Collaboration, 2024).

In conclusion, my Thesis aims at shedding a light on the mysterious origin of extragalactic neutrinos as well as unveiling the most powerful accelerators in the Universe. Such a challenge requires a meticulous investigation through the joint modelling of many astrophysical processes, part of which was made through the Thesis.

6 Appendix A: Code to compute the gamma-ray and neutrino emission

The code computes the γ-ray and neutrino emission cell by cell for the entire $(42.5)^3 Mpc^3$ following the formalism by Pfrommer and Ensslin (2004) described in Section 2.4.

```
global E2=1e8  #GeV    #...maximum assumed kinetic energy of CR protons- debatable
global E1=0.1 #GeV    #...minimum assumed kinetic energy of CR protons

#....energy ranges needed for gamma and neutrino emissions
global const  Eg_range=[0.5,200] #GeV  typical range of γ-rays in FERMI observations
global const  Eν_range=[1e5,1e6] #GeV  typical range of neutrinos detected by IceCUBE

d_l = 2.2772e26 # 73.8Mpc to cm


function cosmic_ray_energy(cr::Float64,α::Float64,dx::Float64,E1::Float64,E2::Float64)
GeVerg=1.6e-10
 ecr= cr*(-α.+1)/(-α.+2)*(E2^(-α.+2)-E1^(-α.+2))/(E2^(-α.+1)-E1^(-α.+1))*GeVerg
return ecr
end


function cosmic_ray_energyV(cr::Array{Float64},α::Float64,dx::Float64,E1::Float64,E2::Float64)
GeVerg=1.6e-10
#ecr.=
return cr.*(-α.+1)/(-α.+2)*(E2^(-α.+2)-E1^(-α.+2))/(E2^(-α.+1)-E1^(-α.+1))*GeVerg
end

function number_cosmic_ray_rangeV(cr::Array{Float64},α::Float64,dx::Float64,E1::Float64,E2::Float64,Ea:
 return cr.*(Eb^(-α.+1)-Ea^(-α.+1))/(E2^(-α.+1)-E1^(-α.+1))
end



function alpha_g(alpha_p::Array{Float64}) #questo è alpha gamma nella trattazione, alpha p  e' l'indice
    alpha_g = similar(alpha_p)
@inbounds for j in 1:size(alpha_p, 2)
@inbounds      @simd   for i in 1:size(alpha_p, 1)
            alpha_g[i,j] = (4.0 * (alpha_p[i,j]- 0.5)/ 3.0)
        end
    end
    return alpha_g
end

function Zν_mu_f(kk::Float64,alpha_gamma::Float64)
```

```
 return 4.0*(3.0-2.0*kk-kk^alpha_gamma*(3.0-2.0*kk+alpha_gamma-kk*alpha_gamma))/(alpha_gamma*(1.0-kk)^2
end
function Zν_e_f(kk::Float64,alpha_gamma::Float64)
 return 24.0*((1.0-kk)*alpha_gamma-kk*(1.0-kk^alpha_gamma))/(alpha_gamma*(1.0-kk)^2.0*(alpha_gamma+1.0)
end
function fterm1(alpha_gamma::Float64,x::Float64)
    return (2.0^(4-alpha_gamma))/(3.0*alpha_gamma)*x^(-alpha_gamma) #primo termine moltiplicativo in q
end
function fterm2(E_g::Float64,x::Float64,delta_gamma::Float64,alpha_gamma::Float64)  #secondo termine mol
    return ((2.0*E_g/x)^delta_gamma+(2.0*E_g/x)^(-delta_gamma))^(-alpha_gamma/delta_gamma)
end

function sigma_pp(alpha_g_val::Array{Float64},pval::Array{Float64}) #...routine for the cross-section
    sigma_pp = similar(alpha_g_val)
@inbounds for j in 1:size(alpha_g_val, 2)
@inbounds   @simd for i in 1:size(alpha_g_val, 1)
     #  sigma_pp[i,j] = ((32 * (0.96 + exp(4.4 - (2.4 * alpha_g_val[i,j])))) * 1e-27) # from mbarn to c
       Eproton=prest*10^pval[i]  #...enery of this proton in GeV
       L=log(Eproton*0.001)      #...
       sigma_pp[i,j] = (1.0-(1.22/Eproton)^4)^2*(34.3 +1.88*L + 0.25*L^2.)*1e-27  #...Kelner+2006 eq.79
    end
    end
    return sigma_pp
end

#tutto questo serve perche' il flusso di neutrini Fv=qgamma*(Zvm+Zve)

# list of available snapshots and corresponding redshifts
snap = [11,   12,   13,   14,  15,  16,   17,  18,19,20,21,22,23, 24,25,26,27]
zeds=[2.815,2.441,2.151,1.84,1.66,1.455,1.34,1.22,1.065,0.968,0.835,0.675,0.555]#,0.312,0.202,0.1,0.02]
#...simulation parameters
const ng=1024   #..1D number of cells
const dx=41.6    #..kpc/cell
const Lbox=42.5 #...Mpc

    @inbounds for k in 10:10  # Loop over timesteps in the snap list above
        global Eg_range, Eν_range, ng

        ss = string(snap[k])

        # Hardcoded values
        z = zeds[k]
        cd = 2.82287e-30*(1 + z)^3 # From code density to g/cm^3, physical units; divide for 1/(1+z)^3
        cv = 1.2584558e+09    # From code velocity to cm/s, physical units; multiply this for 1+z for c
        cb = sqrt(cd * 4 * pi) * cv  # From code B-field to G, physical units; divide for 1/(1+z)^2 for
```

```
      # Range of x, y, z values for the extraction from HDF5 files

      nslice = 32  # The z-direction is going to be analyzed sequentially by extracting nslice planes
      dz = convert(Int64, trunc(ng / nslice))   # Thickness of each slice

      map = Array{Float64}(undef, ng, ng, 12)   # Maps of all quantities
      map .= 0.0
      map2 = Array{Float64}(undef, ng, ng, 6)   # Maps of neutrino and gamma emission for a small sli
      map2 .= 0.0

       @inbounds for lz in 1:nslice   # Looping over the slices in the z-direction
          i1 = 1 #ran_coord[n] - ran_side + 1  #1
          i2 = ng #ran_coord[n] + ran_side    #ng
          j1 = 1 #ran_coord[n] -ran_side + 1 #1
          j2 = ng #ran_coord[n] + ran_side   #ng
          l1 = 1 + dz * (lz - 1)
          l2 = l1 + dz - 1
          ng = i2 - i1 + 1
          nz = l2 - l1 + 1

          dens = h5read(file, string("Density"), (i1:i2, j1:j2, l1:l2))
          temp = h5read(file, string("Temperature"), (i1:i2, j1:j2, l1:l2))

          temp = convert(Array{Float64,3}, temp)
          dens = convert(Array{Float64,3}, dens)

          # B-fields do not enter hadronic emissions, so we just read one for displaying some maps
          bz = h5read(file, string("Bz"), (i1:i2, j1:j2, l1:l2))
          bz = convert(Array{Float64,3}, bz)
          bz .*= cb


cr1=h5read(file2,string("CRe_Density"),(i1:i2,j1:j2,l1:l2))  #...shocks
cr1=convert(Array{Float64,3},cr1)

tcr1=h5read(file2,string("CRe_Time"),(i1:i2,j1:j2,l1:l2))
tcr1=convert(Array{Float64,3},tcr1)

cr2=h5read(file2,string("CRe_Density2"),(i1:i2,j1:j2,l1:l2))  #..Cosmic rays from AGN
cr2=convert(Array{Float64,3},cr2)

tcr2=h5read(file2,string("CRe_Time2"),(i1:i2,j1:j2,l1:l2))
tcr2=convert(Array{Float64,3},tcr2)

cr3=h5read(file2,string("CRe_Density3"),(i1:i2,j1:j2,l1:l2))  #..Cosmic rays from star formation
cr3=convert(Array{Float64,3},cr3)
```

```
tcr3=h5read(file2,string("CRe_Time3"),(i1:i2,j1:j2,l1:l2))
tcr3=convert(Array{Float64,3},tcr3)


          ratio1 = similar(dens)
          ratio1 .= cr1 ./ dens
          imax = findall(x -> isnan(x), ratio1)
          ratio1[imax] .= 0.0

          println(maximum(ratio1))
          println(maximum(cr3))
          # ...

          #....the following is needed to recalibrate a wrongly set injection efficiency for shock in
          ratio1 = similar(dens)
          ratio1 .= cr1 ./ dens
          imax = findall(x -> isnan(x), ratio1)
          ratio1[imax] .= 0.0

          # Needed renormalization step for CR protons from shocks (DSA)
          mad = maximum(ratio1)
          imax = findall(x -> (x == mad), ratio1)
          Kep = 100  # Assumed CR protons to electrons ratio
          norm = 2e-7 / mad * Kep
          cr1 .*= norm
          ratio1 = nothing

          # ...

          dens .*= cd / (m_p * 1.15) / (1.0 - (0.5 * X_He))   # Proton density in part/cm^3
          eth = similar(dens)  # Thermal gas energy
          eth .= kb * 1.5 * dens .* temp * (kpctocm * dx)^3  # Erg

          ecr2 = similar(eth)
          ecr2 .= 0.0
          ecr3 = similar(eth)
          ecr3 .= 0.0
          ecr1 = similar(ecr2)
          ecr1 .= 0.0


          α = 2.05 #2.05 #2.1 #2.2 # CR proton spectrum - it can also be tuned to the age of CRs
          αγ = (4.0 * (α - 0.5) / 3.0)  # Gamma-ray photon spectrum (p-p collisions)
          δγ = (real(0.14 * (αγ + 0im)^-1.6) + 0.44)  # "Shape parameter"
```

```
# ...

minecr1 = 1e-4   # Some reasonable range of values to do emission computations only on the
minecr2 = 1e-5   #era 1e-19 fino a snap 19#...in principle the two thresholds for CR1 and C
minecr3=1e-12

iw2 = findall(x -> (x >= minecr2), cr2)
ncr2 = size(iw2)
println("AGN CRs cells above threshold=", ncr2[1])
cr2 .*= (kpctocm * dx)^3 * cd / (m_p * 1.15) / (1.0 - (0.5 * X_He))

iw3 = findall(x -> (x >= minecr3), cr3)
ncr3 = size(iw3)
println("stellar CRs cells above threshold=", ncr3[1])
cr3 .*= (kpctocm * dx)^3 * cd / (m_p * 1.15) / (1.0 - (0.5 * X_He))

iw1 = findall(x -> (x >= minecr1), cr1)
ncr1 = size(iw1)
println("shocks CRs cells above threshold=", ncr1[1])
cr1 .*= (kpctocm * dx)^3 * cd / (m_p * 1.15) / (1.0 - (0.5 * X_He))

# ...

cr_numγ1 = similar(dens)
cr_numν1 = similar(dens)
cr_numγ2 = similar(dens)
cr_numν2 = similar(dens)
cr_numγ3 = similar(dens)
cr_numν3 = similar(dens)

# ...

# AGN
GeVerg = 1.6e-10
Efactor = (-α + 1) / (-α + 2) * (E2^(-α + 2) - E1^(-α + 2)) / (E2^(-α + 1) - E1^(-α + 1)) *
Nfactor_γ = (Eg_range[2]^(-α + 1) - Eg_range[1]^(-α + 1)) / (E2^(-α + 1) - E1^(-α + 1))
Nfactor_ν = (Eν_range[2]^(-α + 1) - Eν_range[1]^(-α + 1)) / (E2^(-α + 1) - E1^(-α + 1))

ecr2[iw2[:]] .= cr2[iw2[:]] * Efactor
cr_numγ2[iw2[:]] .= cr2[iw2[:]] * Nfactor_γ
cr_numν2[iw2[:]] .= cr2[iw2[:]] * Nfactor_ν

ecr3[iw3[:]] .= cr3[iw3[:]] * Efactor
cr_numγ3[iw3[:]] .= cr3[iw3[:]] * Nfactor_γ
cr_numν3[iw3[:]] .= cr3[iw3[:]] * Nfactor_ν
```

```
# Shocks
ecr1[iw1[:]] .= cr1[iw1[:]] * Efactor
cr_numγ1[iw1[:]] .= cr1[iw1[:]] * Nfactor_γ
cr_numν1[iw1[:]] .= cr1[iw1[:]] * Nfactor_ν

@inbounds for i in 1:dz
    @views map[:, :, 1] += dens[:, :, i] / ng
    @views map[:, :, 2] += temp[:, :, i] / ng
    @views map[:, :, 3] += abs.(bz[:, :, i]) / ng
    @views map[:, :, 4] += ecr1[:, :, i] / ng
    @views map[:, :, 5] += ecr2[:, :, i] / ng
    @views map[:, :, 6] += ecr3[:, :, i] / ng
end

# Gamma-ray and neutrino emission
nΓ = 10        # Number of bins to reconstruct the spectra of gamma and neutrino emission
δΓ = (Eg_range[2] - Eg_range[1]) / nΓ
δΓν = (Eν_range[2] - Eν_range[1]) / nΓ

# Arrays for gamma-ray and neutrino emissions for shocks
F = Array{Float64}(undef, nΓ, ncr1[1])
F .= 0.0
Fν = Array{Float64}(undef, nΓ, ncr1[1])
Fν .= 0.0
# Arrays for gamma-ray and neutrino emissions for AGN
F2 = Array{Float64}(undef, nΓ, ncr2[1])
F2 .= 0.0

Fν2 = Array{Float64}(undef, nΓ, ncr2[1])
Fν2 .= 0.0

# Arrays for gamma-ray and neutrino emissions for SF
F3 = Array{Float64}(undef, nΓ, ncr3[1])
F3 .= 0.0

Fν3 = Array{Float64}(undef, nΓ, ncr3[1])
Fν3 .= 0.0


# Emission from shocks
gamma_emission1 = similar(cr1)
gamma_emission1 .= 0.0
neutrino_emission1 = similar(cr1)
neutrino_emission1 .= 0.0
```

```
# Emission from AGN
gamma_emission2 = similar(cr2)
gamma_emission2 .= 0.0
neutrino_emission2 = similar(cr2)
neutrino_emission2 .= 0.0

 # Emission from SF
gamma_emission3 = similar(cr3)
gamma_emission3 .= 0.0
neutrino_emission3 = similar(cr3)
neutrino_emission3 .= 0.0

# Arrays to store the spectra of gamma-ray and neutrino emissions
gamma_spec = Array{Float64}(undef, nΓ, 2)
gamma_spec .= 0.0
gamma_spec2 = similar(gamma_spec)
gamma_spec3 = similar(gamma_spec)

gamma_specν = Array{Float64}(undef, nΓ, 2)
gamma_specν .= 0.0
gamma_specν2 = similar(gamma_specν)
gamma_specν3 = similar(gamma_specν)

# Initial Lorentz factors for gamma and neutrino emissions
Γ = Eg_range[1] / επp / prest + δΓ * 0.5
Γν = Eν_range[1] / ενp / prest + δΓν * 0.5

# Single loop to produce both gamma-ray and neutrino emissions

@inbounds for i in 1:nΓ
    println("doing energy bin ", i)

    # Gamma emission calculations
    Γ += δΓ
    Eproton = prest * Γ
    E_g0 = Eproton * επp
    delta_gamma = δγ
    alpha_gamma = αγ
    L = log(Eproton * 0.001)

    # Neutrino emission calculations
    Γν += δΓν
    Eproton = prest * Γν
    E_g = Eproton * επp
    Eν = Eproton * ενp
    L = log(Eproton * 0.001)
```

```
    # Functions for calculations
    sigma_pp_val = (1.0 - (1.22 / Eproton)^4)^2 * (34.3 + 1.88 * L + 0.25 * L^2.0) * 1e-27
    term1 = fterm1(alpha_gamma, mass_pion)
    term2 = fterm2(E_g0, mass_pion, delta_gamma, alpha_gamma)

    sigma_pp_valν = (1.0 - (1.22 / Eproton)^4)^2 * (34.3 + 1.88 * L + 0.25 * L^2.0) * 1e-27
    term1ν = fterm1(alpha_gamma, mass_pion)
    term2ν = fterm2(E_g, mass_pion, delta_gamma, alpha_gamma)

    kk = 0.573
    Zν_mu = Zν_mu_f(kk, alpha_gamma)
    Zν_e = Zν_e_f(kk, alpha_gamma)


    # Calculate gamma-ray emission for shocks
    F[i, :] = sigma_pp_val * c * dens[iw1[:]] .* cr_numγ1[iw1[:]] * term1 * term2

    # Calculate neutrino emission for shocks
    Fν[i, :] = (Zν_mu + Zν_e) * (sigma_pp_valν * c * dens[iw1[:]] .* cr_numν1[iw1[:]] * ter

    neutrino_emission1[iw1[:]] .+= Fν[i, :]
    gamma_emission1[iw1[:]] .+= F[i, :]


    # Calculate gamma-ray emission for AGN
    F2[i, :] = sigma_pp_val * c * dens[iw2[:]] .* cr_numγ2[iw2[:]] * term1 * term2

    # Calculate neutrino emission for AGN
    Fν2[i, :] = (Zν_mu + Zν_e) * (sigma_pp_valν * c * dens[iw2[:]] .* cr_numν2[iw2[:]] * te

    # Calculate gamma-ray emission for SF
    F3[i, :] = sigma_pp_val * c * dens[iw3[:]] .* cr_numγ3[iw3[:]] * term1 * term2

    # Calculate neutrino emission for SF
    Fν3[i, :] = (Zν_mu + Zν_e) * (sigma_pp_valν * c * dens[iw3[:]] .* cr_numν3[iw3[:]] * te



    neutrino_emission2[iw2[:]] .+= Fν2[i, :]
    gamma_emission2[iw2[:]] .+= F2[i, :]
    neutrino_emission3[iw3[:]] .+= Fν3[i, :]
    gamma_emission3[iw3[:]] .+= F3[i, :]

end
```

7 Appendix B: Code for the cumulative fluxes

The code presented here has been employed for the computation of the total comoving fluxes and the cumulative fluxes. It takes 17 snapshots as inputs and for each of them computes the total comoving γ-ray and neutrino fluxes (`tot_flux_`) injected by shocks (identified with number 1), AGN (identified with number 2) and star formation (identified with number 3). Next, the data are interpolated with a first order spline function through the built-in Julia function `linear_interpolation()` with a step size of 0.05 in redshift. Then the code proceeds to compute the cumulative fluxes.

```
α =2.05
αγ = (4.0 * (α - 0.5) / 3.0)


tot_flux_neutrino1=zeros(17)
tot_flux_neutrino2=zeros(17)
tot_flux_neutrino3=zeros(17)
tot_flux_gamma1=zeros(17)
tot_flux_gamma2=zeros(17)
tot_flux_gamma3=zeros(17)
sum_flux_gamma2=zeros(17)

snap = [11,   12,   13,   14,  15,  16,   17,  18,19,20,21,22,23,24,25,26,27]
zeds=[2.815,2.441,2.151,1.84,1.66,1.455,1.34,1.22,1.065,0.968,0.835,0.675,0.555,0.312,0.202,0.1,0.02]
com_rad_dist=zeros(17)
lum_dist=zeros(17)

for k in 1:17
    ss = string(snap[k])

    #  Range of x, y, z values for the extraction from HDF5 files

    i1 = 1
    i2 = ng
    j1 = 1
    j2 = ng

    neutrino_emission1 = h5read(file, string("neutrino_map1"), (i1:i2, j1:j2
    gamma_emission1 = h5read(file, string("gamma_map1"), (i1:i2, j1:j2))
    neutrino_emission2 = h5read(file, string("neutrino_map2"), (i1:i2, j1:j2))
    gamma_emission2 = h5read(file, string("gamma_map2"), (i1:i2, j1:j2))
    neutrino_emission3 = h5read(file, string("neutrino_map3"), (i1:i2, j1:j2))
    gamma_emission3 = h5read(file, string("gamma_map3"), (i1:i2, j1:j2))

    neutrino_emission1 = convert(Array{Float64,2}, neutrino_emission1)
    gamma_emission1 = convert(Array{Float64,2}, gamma_emission1)
    neutrino_emission2 = convert(Array{Float64,2}, neutrino_emission2)
    gamma_emission2 = convert(Array{Float64,2}, gamma_emission2)
```

```
    neutrino_emission3 = convert(Array{Float64,2}, neutrino_emission3)
    gamma_emission3 = convert(Array{Float64,2}, gamma_emission3)

    neutrino_emission3.=1e7*neutrino_emission3 # renormalisation
    gamma_emission3.=1e7*gamma_emission3

    tot_flux_neutrino1[k] = sum(neutrino_emission1)
    tot_flux_neutrino2[k] = sum(neutrino_emission2)
    tot_flux_neutrino3[k] = sum(neutrino_emission3)
    tot_flux_gamma1[k] = sum(gamma_emission1)
    tot_flux_gamma2[k] = sum(gamma_emission2)
    tot_flux_gamma3[k] = sum(gamma_emission3)
    rad_dist=comoving_radial_dist(cosmo,zeds[k])
    com_rad_dist[k]=ustrip(comoving_radial_dist(cosmo,zeds[k])::Number)
    lum_dist[k]=ustrip(luminosity_dist(cosmo, zeds[k])::Number)

end

# normalized flux over the volume
norm_flux_neutrino1=reverse(tot_flux_neutrino1)./Lbox^3
norm_flux_neutrino2=reverse(tot_flux_neutrino2)./Lbox^3
norm_flux_neutrino3=reverse(tot_flux_neutrino3)./Lbox^3
norm_flux_gamma1=reverse(tot_flux_gamma1)./Lbox^3
norm_flux_gamma2=reverse(tot_flux_gamma2)./Lbox^3
norm_flux_gamma3=reverse(tot_flux_gamma3)./Lbox^3

# 1D interpolation

xs=range(0.02, step=0.05, stop=2.816)
interp_linear_neutrino1 = linear_interpolation(reverse(zeds), norm_flux_neutrino1)
interp_linear_neutrino2 = linear_interpolation(reverse(zeds),norm_flux_neutrino2)
interp_linear_neutrino3 = linear_interpolation(reverse(zeds),norm_flux_neutrino3)
interp_linear_gamma1 = linear_interpolation(reverse(zeds), norm_flux_gamma1)
interp_linear_gamma2 = linear_interpolation(reverse(zeds), norm_flux_gamma2)
interp_linear_gamma3 = linear_interpolation(reverse(zeds), norm_flux_gamma3)
ys_neutr1=interp_linear_neutrino1(xs) # n/GeV/s/Mpc^3
ys_neutr2=interp_linear_neutrino2(xs)
ys_neutr3=interp_linear_neutrino3(xs)
ys_gamma1=interp_linear_gamma1(xs)
ys_gamma2=interp_linear_gamma2(xs)
ys_gamma3=interp_linear_gamma3(xs)


e_flux_neutrino1=zeros(2)
e_flux_neutrino2=zeros(2)
e_flux_neutrino3=zeros(2)
```

```
e_flux_gamma1=zeros(2)
e_flux_gamma2=zeros(2)
e_flux_gamma3=zeros(2)


# sampling to get error
Random.seed!(115)
ran_coord=rand(1:512, 10)
sp=[16, 27]
for k in 1:2
    flux_neutrino1=zeros(10)
    flux_neutrino2=zeros(10)
    flux_neutrino3=zeros(10)
    flux_gamma1=zeros(10)
    flux_gamma2=zeros(10)
    flux_gamma3=zeros(10)

    for n in 1:10
        ran_side=rand(1:(ran_coord[n]))

        ng=2*ran_side
        lb=string(ng)

        i1= ran_coord[n] - ran_side + 1
        i2 = ran_coord[n] + ran_side
        j1 = ran_coord[n] -ran_side + 1
        j2 = ran_coord[n] + ran_side

        neutrino_emission1 = h5read(file, string("neutrino_map1"), (i1:i2, j1:j2))
        gamma_emission1 = h5read(file, string("gamma_map1"), (i1:i2, j1:j2))
        neutrino_emission2 = h5read(file, string("neutrino_map2"), (i1:i2, j1:j2))
        gamma_emission2 = h5read(file, string("gamma_map2"), (i1:i2, j1:j2))
        neutrino_emission3 = h5read(file, string("neutrino_map3"), (i1:i2, j1:j2))
        gamma_emission3 = h5read(file, string("gamma_map3"), (i1:i2, j1:j2))

        neutrino_emission1 = convert(Array{Float64,2}, neutrino_emission1)
        gamma_emission1 = convert(Array{Float64,2}, gamma_emission1)
        neutrino_emission2 = convert(Array{Float64,2}, neutrino_emission2)
        gamma_emission2 = convert(Array{Float64,2}, gamma_emission2)
        neutrino_emission3 = convert(Array{Float64,2}, neutrino_emission3)
        gamma_emission3 = convert(Array{Float64,2}, gamma_emission3)

        neutrino_emission3.=1e7*neutrino_emission3
        gamma_emission3.=1e7*gamma_emission3
        flux_neutrino1[n] = mean(neutrino_emission1)
        flux_neutrino2[n] = mean(neutrino_emission2)
```

```
        flux_neutrino3[n] = mean(neutrino_emission3)
        flux_gamma1[n] = mean(gamma_emission1)
        flux_gamma2[n] = mean(gamma_emission2)
        flux_gamma3[n] = mean(gamma_emission3)
    end
    e_flux_neutrino1[k]=(maximum(flux_neutrino1)-minimum(flux_neutrino1))/2.0/Lbox^3*ng^2
    e_flux_neutrino2[k]=(maximum(flux_neutrino2)-minimum(flux_neutrino2))/2.0/Lbox^3*ng^2
    e_flux_neutrino3[k]=(maximum(flux_neutrino3)-minimum(flux_neutrino3))/2.0/Lbox^3*ng^2
    e_flux_gamma1[k]=(maximum(flux_gamma1)-minimum(flux_gamma1))/2.0/Lbox^3*ng^2
    e_flux_gamma2[k]=(maximum(flux_gamma2)-minimum(flux_gamma2))/2.0/Lbox^3*ng^2
    e_flux_gamma3[k]=(maximum(flux_gamma3)-minimum(flux_gamma3))/2.0/Lbox^3*ng^2
end
# error

err_flux_neutrino1=zeros(17)
err_flux_neutrino2=zeros(17)
err_flux_neutrino3=zeros(17)
err_flux_gamma1=zeros(17)
err_flux_gamma2=zeros(17)
err_flux_gamma3=zeros(17)

for k in 1:17
  if zeds[k]>=1.0
    err_flux_neutrino1[k]=e_flux_neutrino1[1]/norm_flux_neutrino1[12]*norm_flux_neutrino1[18-k]
    # relative error multiplied by the point value
    err_flux_neutrino2[k]=e_flux_neutrino2[1]/norm_flux_neutrino2[12]*norm_flux_neutrino2[18-k]
    err_flux_neutrino3[k]=e_flux_neutrino3[1]/norm_flux_neutrino3[12]*norm_flux_neutrino3[18-k]
    err_flux_gamma1[k]=e_flux_gamma1[1]/norm_flux_gamma1[12]*norm_flux_gamma1[18-k]
    err_flux_gamma2[k]=e_flux_gamma2[1]/norm_flux_gamma2[12]*norm_flux_gamma2[18-k]
    err_flux_gamma3[k]=e_flux_gamma3[1]/norm_flux_gamma3[12]*norm_flux_gamma3[18-k]
  else
    err_flux_neutrino1[k]=e_flux_neutrino1[2]/norm_flux_neutrino1[1]*norm_flux_neutrino1[18-k]
    err_flux_neutrino2[k]=e_flux_neutrino2[2]/norm_flux_neutrino2[1]*norm_flux_neutrino2[18-k]
    err_flux_neutrino3[k]=e_flux_neutrino3[2]/norm_flux_neutrino3[1]*norm_flux_neutrino3[18-k]
    err_flux_gamma1[k]=e_flux_gamma1[2]/norm_flux_gamma1[1]*norm_flux_gamma1[18-k]
    err_flux_gamma2[k]=e_flux_gamma2[2]/norm_flux_gamma2[1]*norm_flux_gamma2[18-k]
    err_flux_gamma3[k]=e_flux_gamma3[2]/norm_flux_gamma3[1]*norm_flux_gamma3[18-k]
  end
end

# integrated emission

tot_n_flux1=zeros(length(xs)-2)
tot_n_flux2=zeros(length(xs)-2)
tot_n_flux3=zeros(length(xs)-2)
tot_g_flux1=zeros(length(xs)-2)
```

```
tot_g_flux2=zeros(length(xs)-2)
tot_g_flux3=zeros(length(xs)-2)
sum_n=zeros(length(xs)-2)
sum_g=zeros(length(xs)-2)
com_volume=zeros(length(xs)-2)
com_d=zeros(length(xs))
lum_d=zeros(length(xs)-2)
zs=zeros(length(xs)-2)
err_n_flux1=zeros(length(xs)-2)
err_n_flux2=zeros(length(xs)-2)
err_n_flux3=zeros(length(xs)-2)
err_g_flux1=zeros(length(xs)-2)
err_g_flux2=zeros(length(xs)-2)
err_g_flux3=zeros(length(xs)-2)

for k in 1:(length(xs))
  com_d[k]=ustrip(comoving_radial_dist(cosmo,xs[k])::Number)
end

for i in 2:(length(xs)-1)
  com_volume[i-1]=4*pi*com_d[i]^2*abs(com_d[i+1]-com_d[i-1]) # Mpc^3
  zs[i-1]=xs[i] # redshift for plots
  lum_d[i-1]=ustrip(luminosity_dist(cosmo, xs[i]))
  tot_n_flux1[i-1]=(1+xs[i])^(-αγ+1)*ys_neutr1[i]*com_volume[i-1]*1e3*(Eν_range[1])^2/(4*pi*(lum_d[i-1]
  tot_n_flux2[i-1]=(1+xs[i])^(-αγ+1)*ys_neutr2[i]*com_volume[i-1]*1e3*(Eν_range[1])^2/(4*pi*(lum_d[i-1]
  tot_n_flux3[i-1]=(1+xs[i])^(-αγ+1)*ys_neutr3[i]*com_volume[i-1]*1e3*(Eν_range[1])^2/(4*pi*(lum_d[i-1]
  tot_g_flux1[i-1]=(1+xs[i])^(-αγ+1)*ys_gamma1[i]*com_volume[i-1]*1e3*(Eg_range[1])^2/(4*pi*(lum_d[i-1]
  tot_g_flux2[i-1]=(1+xs[i])^(-αγ+1)*ys_gamma2[i]*com_volume[i-1]*1e3*(Eg_range[1])^2/(4*pi*(lum_d[i-1]
  tot_g_flux3[i-1]=(1+xs[i])^(-αγ+1)*ys_gamma3[i]*com_volume[i-1]*1e3*(Eg_range[1])^2/(4*pi*(lum_d[i-1]
  sum_n[i-1]=tot_n_flux1[i-1]+tot_n_flux2[i-1]+tot_n_flux3[i-1]
  sum_g[i-1]=tot_g_flux1[i-1]+tot_g_flux2[i-1]+tot_g_flux3[i-1]

  if zs[i-1]>=1.0
    err_n_flux1[i-1]=(1+xs[i])^(-αγ+1)*ys_neutr1[i]*com_volume[i-1]*1e3*(Eν_range[1])^2/(4*pi*(lum_d[i-
    err_n_flux2[i-1]=(1+xs[i])^(-αγ+1)*ys_neutr2[i]*com_volume[i-1]*1e3*(Eν_range[1])^2/(4*pi*(lum_d[i-
    err_n_flux3[i-1]=(1+xs[i])^(-αγ+1)*ys_neutr3[i]*com_volume[i-1]*1e3*(Eν_range[1])^2/(4*pi*(lum_d[i-
    err_g_flux1[i-1]=(1+xs[i])^(-αγ+1)*ys_gamma1[i]*com_volume[i-1]*1e3*(Eg_range[1])^2/(4*pi*(lum_d[i-
    err_g_flux2[i-1]=(1+xs[i])^(-αγ+1)*ys_gamma2[i]*com_volume[i-1]*1e3*(Eg_range[1])^2/(4*pi*(lum_d[i-
    err_g_flux3[i-1]=(1+xs[i])^(-αγ+1)*ys_gamma3[i]*com_volume[i-1]*1e3*(Eg_range[1])^2/(4*pi*(lum_d[i-

  else
    err_n_flux1[i-1]=(1+xs[i])^(-αγ+1)*ys_neutr1[i]*com_volume[i-1]*1e3*(Eν_range[1])^2/(4*pi*(lum_d[i-
    err_n_flux2[i-1]=(1+xs[i])^(-αγ+1)*ys_neutr2[i]*com_volume[i-1]*1e3*(Eν_range[1])^2/(4*pi*(lum_d[i-
    err_n_flux3[i-1]=(1+xs[i])^(-αγ+1)*ys_neutr3[i]*com_volume[i-1]*1e3*(Eν_range[1])^2/(4*pi*(lum_d[i-
    err_g_flux1[i-1]=(1+xs[i])^(-αγ+1)*ys_gamma1[i]*com_volume[i-1]*1e3*(Eg_range[1])^2/(4*pi*(lum_d[i-
    err_g_flux2[i-1]=(1+xs[i])^(-αγ+1)*ys_gamma2[i]*com_volume[i-1]*1e3*(Eg_range[1])^2/(4*pi*(lum_d[i-
```

```
    err_g_flux3[i-1]=(1+xs[i])^(-αγ+1)*ys_gamma3[i]*com_volume[i-1]*1e3*(Eg_range[1])^2/(4*pi*(lum_d[i-
  end
end

# cumulutive flux
cum_n_flux1=zeros(length(tot_n_flux1))
cum_n_flux2=zeros(length(tot_n_flux2))
cum_n_flux3=zeros(length(tot_n_flux3))
cum_sum_n_flux=zeros(length(tot_g_flux1))
cum_g_flux1=zeros(length(tot_g_flux1))
cum_g_flux2=zeros(length(tot_g_flux2))
cum_g_flux3=zeros(length(tot_g_flux3))
cum_sum_g_flux=zeros(length(tot_g_flux1))
err_cum_n_flux1=zeros(length(tot_g_flux1))
err_cum_n_flux2=zeros(length(tot_g_flux1))
err_cum_n_flux3=zeros(length(tot_g_flux1))
err_cum_g_flux1=zeros(length(tot_g_flux1))
err_cum_g_flux2=zeros(length(tot_g_flux1))
err_cum_g_flux3=zeros(length(tot_g_flux1))

cum_n_flux1[1]=tot_n_flux1[1]
cum_n_flux2[1]=tot_n_flux2[1]
cum_n_flux3[1]=tot_n_flux3[1]
cum_sum_n_flux[1]=(tot_n_flux1[1]+tot_n_flux2[1]+tot_n_flux3[1])
cum_g_flux1[1]=tot_g_flux1[1]
cum_g_flux2[1]=tot_g_flux2[1]
cum_g_flux3[1]=tot_g_flux3[1]
cum_sum_g_flux[1]=(tot_g_flux1[1]+tot_g_flux2[1]+tot_g_flux3[1])

err_cum_n_flux1[1]=err_n_flux1[1]
err_cum_n_flux2[1]=err_n_flux2[1]
err_cum_n_flux3[1]=err_n_flux3[1]
err_cum_g_flux1[1]=err_g_flux1[1]
err_cum_g_flux2[1]=err_g_flux2[1]
err_cum_g_flux3[1]=err_g_flux3[1]

for i in 2:(length(tot_n_flux1))
  cum_n_flux1[i]=cum_n_flux1[i-1]+tot_n_flux1[i]
  cum_n_flux2[i]=cum_n_flux2[i-1]+tot_n_flux2[i]
  cum_n_flux3[i]=cum_n_flux3[i-1]+tot_n_flux3[i]
  cum_sum_n_flux[i]=cum_n_flux1[i]+cum_n_flux2[i]+cum_n_flux3[i]
  cum_g_flux1[i]=cum_g_flux1[i-1]+tot_g_flux1[i]
  cum_g_flux2[i]=cum_g_flux2[i-1]+tot_g_flux2[i]
  cum_g_flux3[i]=cum_g_flux3[i-1]+tot_g_flux3[i]
  cum_sum_g_flux[i]=cum_g_flux1[i]+cum_g_flux2[i]+cum_g_flux3[i]
  # error Cumulative
```

```
  err_cum_n_flux1[i]=err_cum_n_flux1[i-1]+err_n_flux1[i]
  err_cum_n_flux2[i]=err_cum_n_flux2[i-1]+err_n_flux2[i]
  err_cum_n_flux3[i]=err_cum_n_flux3[i-1]+err_n_flux3[i]
  err_cum_g_flux1[i]=err_cum_g_flux1[i-1]+err_g_flux1[i]
  err_cum_g_flux2[i]=err_cum_g_flux2[i-1]+err_g_flux2[i]
  err_cum_g_flux3[i]=err_cum_g_flux3[i-1]+err_g_flux3[i]
end

# scaling to match the gamma ray flux
scaling=2e-4/cum_sum_g_flux[length(cum_sum_g_flux)]

s_cum_n_flux1=cum_n_flux1.*scaling
s_cum_n_flux2=cum_n_flux2.*scaling
s_cum_n_flux3=cum_n_flux3.*scaling
s_cum_sum_n_flux=cum_sum_n_flux.*scaling
s_cum_g_flux1=cum_g_flux1.*scaling
s_cum_g_flux2=cum_g_flux2.*scaling
s_cum_g_flux3=cum_g_flux3.*scaling
s_cum_sum_g_flux=cum_sum_g_flux.*scaling

err_s_cum_n_flux1=err_cum_n_flux1.*scaling
err_s_cum_n_flux2=err_cum_n_flux2.*scaling
err_s_cum_n_flux3=err_cum_n_flux3.*scaling
err_s_cum_g_flux1=err_cum_g_flux1.*scaling
err_s_cum_g_flux2=err_cum_g_flux2.*scaling
err_s_cum_g_flux3=err_cum_g_flux3.*scaling

# spectrum
spec=[11.22*cum_sum_n_flux[length(cum_sum_n_flux)], cum_sum_n_flux[length(cum_sum_n_flux)]]
E_nu=[5e4, 5e5]
e_spec=[11.22*(err_cum_n_flux1[length(err_cum_n_flux1)]+err_cum_n_flux2[length(err_cum_n_flux2)]+err_cu
```

References

M. Aartsen and et al. "search for time-independent neutrino emission from astrophysical sources with 3 yr of ice cube data". *The Astrophysical Journal*, 2013.

M. Aartsen and et al. "a combined maximum-likelihood analysis of the high-energy astrophysical neutrino flux measured with ice cube". *The Astrophysical Journal*, 2015.

M. Aartsen and et al. "the contribution of fermi-2lac blazars to diffuse tev-pev neutrino flux". *The Astrophysical Journal*, 2017.

M. Ajello, M. Di Mauro, V. S. Paliva, and S. Garrappa. "the γ-ray emission of star-forming galaxies". 2020.

M. Ajello, M. Di Mauro, V. S. Paliya, and S. Garrappa. The γ-Ray Emission of Star-forming Galaxies. *apj*, 894(2):88, May 2020. doi: 10.3847/1538-4357/ab86a6.

R. Beckmann, Y. Dubois, A. Pellissier, V. Olivares, V. Polles, O. Hahn, P. Guillard, and M. Lehnrt. "cosmic rays and thermal instability in self-regulating cooling flows of massive galaxy clusters". *Astronomy & Astrophysics*, 2022.

R. S. Beckmann, Y. Dubois, P. Guillard, P. Salome, V. Olivares, F. Polles, C. Cadiou, F. Combes, S. Hamer, M. D. Lehnert, and G. Pineau des Forets. Dense gas formation and destruction in a simulated Perseus-like galaxy cluster with spin-driven black hole feedback. *aap*, 631:A60, Nov. 2019. doi: 10.1051/0004-6361/201936188.

A. R. Bell and J. H. Matthews. "echoes of the past: ultra-high-energy cosmic rays accelerated by radiogalaxies, scattered by starburst galaxies". *Monthly Notices of the Royal Astronomical Society*, 2022.

P. Bhattacharjee. Origin and propagation of extremely high energy cosmic rays. *physrep*, 327:109–247, Mar. 2000. doi: 10.1016/S0370-1573(99)00101-5.

S. Buson, A. Tramacere, L. Pfeiffer, L. Oswald, R. de Menezes, A. Azzollini, and M. Ajello. "beginning a journey across the universe: the discovery of extragalactic neutrino factories". 2022.

S. Buson, A. Tramacere, L. Pfeiffer, L. Oswald, E. Barbano, G. Fichet de Clairefontaine, V. Baghmanyan, R. de Menezes, A. Azzollini, and M. Ajello. "extragalactic neutrino factories". 2023.

A. M. Bykov, F. Vazza, J. A. Kropotina, K. P. Levenfish, and F. B. S. Paerels. "shocks and non-thermal particle sin clusters of galaxies". 2019.

D. Caprioli and A. Spitkovsky. "simulation of ion acceleration at non-relativist shocks. i acceleration efficiency". 2014.

M. Cardillo, M. Tavani, A. Giuliani, S. Yoshiike, H. Sano, T. Fukuda, Y. Fukui, G. Castelletti, and G. Dubner. "the supernove remnant w44: confirmations and challenges for cosmic-ray acceleration". *Astronomy & Astrophysics*, 2014.

I. Collaboration. "characterization of the astrophysical diffuse neutrino flux using starting track events in icecube". 2024.

P. A. O. Collaboration. ”indication of anisotropy in arrival directions of ultra-high-energy cosmic rays through comparison to the flux pattern of extragalactic gamma-ray sources”. *The Astrophysical Journal*, 2018.

T. P. A. Collaboration. ”searches for anisotropies in the arrival directions of the highest energy cosmic rays detected by the pierre auger observatory”. *The Astrophysical Journal*, 2015.

J. Condon and A. M. Matthews. ”λ cdm cosmology for astronomers”. 2018.

J. H. Croston, J. Ineson, and M. J. Hardcastle. Particle content, radio-galaxy morphology, and jet power: all radio-loud AGN are not equal. *mnras*, 476(2):1614–1623, May 2018. doi: 10.1093/mnras/sty274.

M. di Mauro. ”the origin of the fermi-lat γ-ray background”. *WSPC Proceedings*, 2016.

T. A. Ensslin, C. Pfrommer, V. Springel, and M. Jubelgas. ”cosmic ray physics in calculations of cosmological structure formation”. 2007.

FermiLAT-Collaboration. ”the spectrum of isotropic diffuse gamma-ray emission between 100 mev and 820 gev”. 2014.

J. A. Formaggio and G. P. Zeller. ”from ev to eev: Neutrino cross-sections across energy scales”. 2013.

M. Gaspari, D. Eckert, S. Ettori, P. Tozzi, L. Bassini, E. Rasia, F. Brighenti, M. Sun, S. Borgani, S. D. Johnson, G. R. Tremblay, J. M. Stone, P. Temi, H. Y. K. Yang, F. Tombesi, and M. Cappi. The X-Ray Halo Scaling Relations of Supermassive Black Holes. *apj*, 884(2):169, Oct. 2019. doi: 10.3847/1538-4357/ab3c5d.

N. Gehrels, E. Ramirez-Ruiz, and D. B. Fox. ”gamma ray bursts in the swift era”. *Annual Review of Astronomy and Astrophysics*, 2009.

G. Ghisellini. ”the blazar sequence 2.0”. 2016.

P. D. Group. ”review of particle physics”. 2012.

J.-H. Ha, D. Ryu, and H. Kang. ”gamma-ray and neutrino emissions due to cosmic-ray protons accelerated at intracluster shocks in galaxy clusters”. *The Astrophysical Journal*, 2020.

D. Harari, S. Mollerach, and E. Roulet. Anisotropies of ultrahigh energy cosmic rays diffusing from extragalactic sources. *Phys. Rev. D*, 89:123001, Jun 2014. doi: 10.1103/PhysRevD.89.123001. URL https://link.aps.org/doi/10.1103/PhysRevD.89.123001.

IceCube, Fermi-LAT, MAGIC, AGILE, ASAS-SN, HAWC, H.E.S.S, INTEGRAL, Kanata, Kiso, Kapteyn, L. telescope, Subaru, Swift/NuSTAR, VERITAS, and V.-. teams. ”multi-messenger observations of a flaring blazar coincident with high-energy neutrino icecube-170922a”. 2018.

IceCube-Collaboration. ”an absence of neutrinos associated with cosmic ray acceleration in gamma-ray bursts”. 2013.

IceCube Collaboration. ”search for neutrino emission from hard x-ray agn with icecube”. 2024.

IceCube-Collaboration. ”evidence for neutrino emission from the nearby active galaxy ngc 1068”. 2024.

IceCube Collaboration. ”icecube search for neutrino emission from x-ray bright seyfert galaxies”. 2024.

H. Kang. Semi-Analytic Models for Electron Acceleration in Weak ICM Shocks. *Journal of Korean Astronomical Society*, 53:59–67, June 2020. doi: 10.5303/JKAS.2020.53.3.59.

H. Kang. Diffusive Shock Acceleration by Multiple Weak Shocks. *Journal of Korean Astronomical Society*, 54:103–112, June 2021.

H. Kang and T. W. Jones. ”self-similar evolution of cosmic-ray-modified quasi-parallel plane shocks”. 2007.

H. Kang and D. Ryu. ”diffusive shock acceleration at cosmological shock waves”. 2013.

S. R. Kelner, F. A. Aharonian, and V. V. Bugayov. ”energy spectra of gamma-rays, electrons and neutrinos produced at proton-proton interactions in the very hihg energy regime”. 2006.

R. C. Kennicutt, Jr. The Global Schmidt Law in Star-forming Galaxies. *apj*, 498:541–552, May 1998. doi: 10.1086/305588.

A. V. Kravtsov. On the Origin of the Global Schmidt Law of Star Formation. *apjl*, 590:L1–L4, June 2003. doi: 10.1086/376674.

E. Kun, I. Bartos, J. Becker Tjus, P. L. Biermann, A. Franckowiak, F. Halzen, S. Del Palacio, and J. Woo. ”a correlation between hard x-rays and neutrinos in radio-loud and radio-quiet agn”. 2024.

A. Lazarian, S. Xu, and Y. Hu. Cosmic ray propagation in turbulent magnetic fields. *Frontiers in Astronomy and Space Sciences*, 10, 2023. ISSN 2296-987X. doi: 10.3389/fspas.2023.1154760. URL `https://www.frontiersin.org/articles/10.3389/fspas.2023.1154760`.

M. S. Longair. *”High Energy Astrophysics”*, volume Third Edition. Cambridge University Press, 2011.

P. Madau and M. Dickinson. Cosmic Star-Formation History. *araa*, 52:415–486, Aug. 2014. doi: 10.1146/annurev-astro-081811-125615.

J. H. Matthews, A. R. Bell, and K. M. Blundell. ”particle acceleration in astrophysical jets”. 2020.

K. Murase. ”hidden hearts of neutrino active galaxies”. 2022.

K. Murase, C. M. Karwin, S. S. Kimura, M. Ajello, and S. Buson. ”sub-gev gamma rays from nearby seyfert galaxies and implications for coronal neutrino emission”. 2024.

A. Neronov, D. Savchenko, and D. V. Semikoz. ”neutrino signal from seyfert galaxies”. 2023.

P. Padovani. ”active galactic nuclei at all wavelengths and from all angles”. 2017.

P. Padovani, D. M. Alexander, R. J. Assef, B. De Marco, P. Giommi, R. C. Hickox, G. T. Richards, V. Smolcic, E. Hatziminaoglou, V. Mainieri, and M. Salvato. ”active galactic nuclei: what's in a name?”. 2017.

P. Padovani, R. Gilli, E. Resconi, C. Bellenghi, and F. Henningsen. ”the neutrino background from non-jetted active galactic nuclei”. *Astronomy & Astrophysics*, 2024.

C. Pfrommer and T. A. Ensslin. ”constraining the population of cosmic ray protons in cooling-flow clusters with γ-ray and radio observations: Are radio mini-halos of hadronic origin?”. *Astronomy & Astrophysics*, 2004.

C. Pfrommer, R. Pakmor, C. M. Simpson, and V. Springel. "simulating gamma-ray emission in star-forming galaxies". *apjl*, 847(2):L13, Oct. 2017. doi: 10.3847/2041-8213/aa8bb1.

S. Pozzi. "high intensity focused ultrasound (hifu): computing tools for medical applications". Master's thesis, Universita' La Sapienza, 2014.

A. Reimer, M. Boettcher, and S. Buson. "cascading constraints from neutrino-emitting blazars: The case of txs 0506+056". *The Astrophysical Journal*, 2019.

V. Shaw, A. van Vliet, and A. Taylor. "magnetic fields in the galactic halo bubbles and deflections of uhecrs". *Proceedings of Science*, 2023.

R. S. Somerville and R. Davé. "physical models of galaxy formation in a cosmological framework". 2014.

C. Spiering. *"Particle Physics Reference Library"*, volume 2 Detectors for particles and Radiation. Astronomy and Astrophysics Library Springer Nature, 2020.

M. Spurio. *"Probes of multimessenger Astrophysics (Charged Cosmic Rays, Neutrinos, Gamma-Rays and Gravitational waves)"*, volume Second Edition. Astronomy and Astrophysics Library Springer Nature, 2018.

R. Stein, S. van Velzen, M. Kowalski, A. Franckowiak, and S. Gezari. "a tidal disruption event coincident with a high-energy neutrino". 2021.

M. C. Urry and P. Padovani. "unified schemes for radio-loud active galactic nuclei". 1995.

F. Vazza, M. Brueggen, D. Wittor, C. Gheller, D. Eckert, and M. Stubbe. "constraining the efficiency of cosmic ray acceleration by cluster shocks". 2016.

F. Vazza, M. Brueggen, C. Gheller, S. Hackstein, D. Wittor, and P. M. Hinz. Simulations of extragalactic magnetic fields and of their observables. *Classical and Quantum Gravity*, 2017. URL http://iopscience.iop.org/10.1088/1361-6382/aa8e60.

M. Vogelsberger, F. Marinacci, P. Torrey, and E. Puchwein. "cosmological simulations of galaxy formation". 2019.

C. Volpe. "neutrino astrophysics : recent advances and open issues". *Journal of Physics: Conference Series*, 2015.

W. Winter. "sources of high-energy astrophysical neutrinos". 2024.

D. Wittor, F. Vazza, D. Ryu, and H. Kang. Limiting the shock acceleration of cosmic ray protons in the ICM. *mnras*, 495(1):L112–L117, Apr. 2020. doi: 10.1093/mnrasl/slaa066.

This work was supported by the European Research Council, ERC Starting Grant *MessMapp*, S. B. Principal Investigator, under contract no. 949555 and by Fondazione Cariplo and Fondazione CDP, through grant no Rif:2022-2088 CUP J33C22004310003 for "BREAKTHRU" project (F. V. Principal Investigator).